Title
Materials Science Tools for Regenerative Medicine

Author
Richardson, Wade N

Publication Date
2013

Peer reviewed|Thesis/dissertation

UNIVERSITY OF CALIFORNIA

Los Angeles

Materials Science Tools for Regenerative Medicine

A dissertation submitted in partial satisfaction of the
requirements for the degree Doctor of Philosophy
in Materials Science and Engineering

by

Wade Nichols Richardson

2014

ABSTRACT OF THE DISSERTATION

Materials Science Tools for Regenerative Medicine

by

Wade Nichols Richardson
Doctor of Philosophy in Materials Science and Engineering
University of California, Los Angeles, 2014
Professor Bruce Dunn, Chair

Regenerative therapies originating from recent technological advances in biology could revolutionize medicine in the coming years. In particular, the advent of human pluripotent stem cells (hPSCs), with their ability to become any cell in the adult body, has opened the door to an entirely new way of treating disease. However, currently these medical breakthroughs remain only a promise. To make them a reality, new tools must be developed to surmount the new technical hurdles that have arisen from dramatic departure from convention that this field represents.

The collected work presented in this dissertation covers several projects that seek to apply the skills and knowledge of materials science to this tool synthesizing effort. The work is divided into three chapters. The first deals with our work to apply Raman spectroscopy, a tool widely used for materials characterization, to

degeneration in cartilage. We have shown that Raman can effectively distinguish the matrix material of healthy and diseased tissue. The second area of work covered is the development of a new confocal image analysis for studying hPSC colonies that are chemical confined to uniform growth regions. This tool has important application in understanding the heterogeneity that may slow the development of hPSC –based treatment, as well as the use of such confinement in the eventually large-scale manufacture of hPSCs for therapeutic use. Third, the use of structural templating in tissue engineering scaffolds is detailed. We have utilized templating to tailor scaffold structures for engineering of constructs mimicking two tissues: cartilage and lung.

The work described here represents several important early steps towards large goals in regenerative medicine. These tools show a great deal of potential for accelerating progress in this field that seems on the cusp of helping a great many people with otherwise incurable disease.

The dissertation of Wade Nichols Richardson is approved.

_____

Ioanna Kakoulli

_____

Denis Evseenko

_____

Bruce Dunn, Committee Chair

University of California, Los Angeles

2014

TABLE OF CONTENTS

LIST OF FIGURES

LIST OF TABLES

ACKNOWLEDGMENTS

The work presented in this dissertation could not have been possible if not for the help a large number of people. The work itself has all been very collaborative and I hope a can capture here how grateful I am to all of the people whom I have worked side by side with in the lab, day after day to reach this point. Of course, I would not have been able remain diligent and persistent, and accomplish what I have without the love and support of many people outside of the lab. For them especially I must take this opportunity to say thank you.

Before I gush about all of the wonderful people in my life I need to take care of a short bit of business. Chapter 2 is a modified version of a manuscript submitted for publication to the Journal of Biophotonics. Chapter 3 is being prepared for submission for publication. During my tenure at UCLA I have worked thanks to the funding of several agencies. I would like to thank the National Institutes of Health for funding my work through grant PO1 GM081621. I would also like to thank the California Institute for Regenerative Medicine for supporting me through the CIRM Training Grant (T1-00005), as well as the UCLA Eli and Edith Broad Stem Cell Research Center for also supporting me with a training grant. Finally, I am grateful to the Nippon Sheet Glass Company for providing funding for the NSG fellowship, which I was awarded.

First, I must thank those worked on the same projects as me and made this research possible. Steve Jonas is first on this list since he was the one preceded me

in the lab and acted as a day-to-day mentor who guided me through my early time in graduate school. I can't thank him enough for the insights he gave me on how to navigate our lab's unique position as a tool maker for our collaborators. In addition I need to thank Julien Polleux for his help at the beginning of my time at UCLA and Dan Wilkinson for his tremendous help at the end. Dan has been instrumental in the design and execution of much of the work presented in this dissertation. I thank him and wish him the best of luck in continuing the work and anything else he does. I would also like to thank all the other members of the Dunn lab who have helped me over the years, in particular Danielle Casillas for help with electron microscopy, and Peter Malati for fixing things too numerous to describe.

The other half of all of the research presented here belongs to the collaborators that I have worked with. There would have been no work to do without them. Our collaboration with April Pyle has been a central part of our lab's effort in regenerative medicine. She has provided a huge amount of guidance through the problems in stem cell science that need addressing, and she has been willing to try the new ideas we have brought to her to solve these problems. My sincere thanks to her. In Prof. Pyle's lab I would like to thank Sean Sherman, Kaushali Thakore-Shah, Richard Swan, Majib Jan, Cory Peterson, and especially Jackie Alva. Jackie is in the unique position of having earned my thanks independently in two different labs. She is now a member of Brigitte Gomperts lab. In that lab, of course Brigitte needs the most thanks. She put enormous trust in me to help lead a very ambitious project to recreate lung tissue. I would also like to

thank Preethi Vijayaraj and Daniel Sivalingam for all of their hard work on this project. I would also like to thank Hong Wu, Owen Witte, Gay Crooks, Chih-Ming Ho, Heather Maynard, and Amander Clark for their collaborations.

The Dunn lab's collaboration with Denis Evseenko goes back to my first year at UCLA and worked together on many projects leading up to our very fruitful effort presented in Chapter 2. Not only do I need to thank Denis for all of these years of stimulating and enthusiastic collaboration, but also for serving as a member of my doctoral committee as well as for being constant source of honest and useful advice. Thank you, Denis. I would also like to thank the other members of my committee. Both Yu Huang and Ioanna Kakoulli have been very kind, understanding and helpful since I formed my committee.

Of course the most important member of my committee is my advisor, Bruce Dunn. I owe Professor Dunn my thanks as well as great deal more. From the first day of my visitation to UCLA he has always been able to keep me excited and driven about science. I've known that if I were having a hard time with something, that I would come out of a meeting with him feeling better about it. I've benefitted from his wisdom and from his kindness; from his intelligence and from his hard work. I could not have asked for a more supportive advisor during my PhD and hope very much that I have been a satisfactory student during my time here.

Now I need to switch from the professionally help I have received to my friends and family. Many of those I want to thank are ones with whom I shared in the trials of graduate school. It has been a great comfort to have friends who could

appreciate what I was going through. In particular I could not have made it without the friendship of Veronica Augustyn and Alex Bataller, they have been most excellent friends. I also want to acknowledge the kind friendship of Eric Gschweng, Sean Sherman, Gabe Ferguson, John Vincent, Peter Malati, Danielle Casillas, Paul Brochu, Jon Tesch, Stephanie Reed, Jackie Alva, and the many others I sadly don't have space to list.

There have also been several other people in my life that have provided tremendous support for me during my PhD. First, I want to thank my parent for not only they're wonderful support during this time, but for everything they have done for me leading up to now, to which I owe any success I have. I love you. I also want to thank Ana Muniz, with whom I can to UCLA from Tucson. Often the first part of graduate school is the hardest part to get through, and I know Ana's support during that time got me through. Of course, the other difficult part of graduate school is often the end. During this time I have depended on Sachi Kobayashi for help and she has been there. Thank you Sachi. I also need to thank my brother Jacob. He was the one who lead me to choose Materials Science for my career by choosing it for himself. From him I have learned a lot about being a scientist, a graduate student, and soon I think, a PhD researcher. Thanks Jake.

VITA

2005	B.S., Materials Science and Engineering University of Arizona Tucson, Arizona
2007	M.S., Materials Science and Engineering University of Arizona Tucson, Arizona
2007 - Present	PhD student, Materials Science and Engineering University of California, Los Angeles Los Angeles California

PUBLICATIONS AND PRESENTATIONS

Z.P. Tolstyka, **Wade Richardson**, E. Bat, C. J. Stevens, D. P. Parra, J. K. Dozier, M.D. Distefano, B. Dunn, and H. D. Maynard. "Chemoselective immobilization of proteins by microcontact printing and bioorthogonal click reactions." ChemBiochem. 14, 2464-71 (2013)

D. Evseenko, B. Latour, **Wade Richardson**, M. Corselli, A. Sahaghian, Y. Zhu, R. Chan, B. Dunn and G. M. Crooks. "Lysophosphatidic acid mediates myeloid differentiation within the human bone marrow microenvironment." *PLOS One.* 8, e63718 (2013)

Steven J. Jonas, Jackelyn A. Alva, **Wade Richardson**, Sean P. Sherman, Zoran Galic, April D. Pyle, Bruce Dunn. **"**A spatially and chemically defined platform for the uniform growth of human pluripotent stem cells." *Materials Science and Engineering: C*, 33, 234-41 (2013).

Douglas A. Loy, **Wade Richardson**. "Preparation and characterization of fluorescent silica and silsesquioxane nanoparticles." *PMSE Preprints.* 98, 9 (2008)

B. McMorrow, R. Chartoff, P. Lucas, **Wade Richardson**, and P. Anderson. "Particle surface treatment for nanocomposites containing ceramic particles." *Composite Interfaces*. 13, 801–817 (2006)

Wade Richardson, D. Evseenko, B. Dunn. "Raman spectroscopy: an enabling tool for cartilage regeneration." Poster session at the 7th annual UCLA Stem Cell Symposium, February 10, 2012

Wade Richardson, S. Jonas, J. Alva, A. Pyle, B. Dunn. "Micropatterning self-assembled monolayers as culture platforms for human embryonic stem cells." Poster session at 8th annual meeting of the International Society for Stem Cell Research, San Francisco, CA, June 17, 2010.

Wade Richardson, S. Jonas, V. Bahram, E. Gschweng, C. Peterson, A. Pyle, H. Wu, O. Witte, B. Dunn. "Micropatterned self-assembled monolayers as culture platforms for human and mouse embryonic stem cells." Poster session at 8th annual meeting of the International Society for Stem Cell Research, Barcelona, Spain, July 10, 2009.

Wade Richardson, S. Jonas, V. Bahram, J. Polleux, S. Guo, E. Gschweng, K. Kam, C. Peterson, A. Pyle, H. Wu, O. Witte, B. Dunn. "Hydrophobic substrates for improved embryoid body mediated embryonic stem cell differentiation." Poster session at the California Institute for Regenerative Medicine grantee meeting, September 17, 2008.

Introduction and Background

Chapter 1.1. Overview

Regenerative medicine holds tremendous promise to treat a wide range of human diseases by restoring damaged tissues or organs. This has drawn an enormous and rapidly growing research effort, much of which has been directed towards the study of human pluripotent stem cells (hPSCs), which possess the unique potential to differentiate to produce any cell type from the three embryonic germ lineages [1–4]. Despite this incredible potential, the successful clinically implementation of cellular or tissue regeneration derived from hPSCs remains elusive. While residual stem cell plasticity in final transplants is the most often cited technical impediment[5,6], many aspects of producing a successful regenerative therapy remain far from perfected. Indeed, such fundamental facets of this process as the choice of the PSCs source (embryonic or reprogrammed somatic)[7,8] and the ideal hPSC culture methods are still open areas of investigation[9–11]. Furthermore, for a given regenerative therapy the definitive phenotypic characteristics of the cell type best suited for transplant, and detailed differentiation, purification, and implantation methods must be worked out for that specific therapy. The opportunity now exists to overcome these difficulties and advance this burgeoning field to the ultimate goal of clinical therapy through the introduction of new tools and technologies.

The objective of the research presented here has been to produce enabling technologies by applying engineering principles, materials and characterization methods to pressing challenges in regenerative medicine. One critical application of regenerative medicine is the restoration of damaged articular cartilage. In this arena we have employed Raman spectroscopy to develop a method to distinguish healthy and diseased cartilage tissue. Beyond improving clinical diagnosis in patients this work has potential to accelerate progress in cartilage tissue engineering by providing routine feedback in the lab. In another area, we have sought to address the lack of uniform and consistent culture methods for hPSCs. We have made use of soft-lithographic techniques to direct the patterning of hPSC colony growth into defined areas to produce more uniform culture conditions. We have previously shown that these patterns have the potential to bring improved consistency to hPSC culture. Here we demonstrate that they can be used in concert with automated confocal image analysis to create a new tool for the study of spatial aspects of hPSC heterogeneity. The third research focus presented is the structural templating in scaffolds for the 3-dimensional (3-D) culture of hPSC-derived progenitor cells to direct differentiation or reproduce tissue architecture.

Chapter 1.2 Raman Spectroscopy and Cartilage Disease

Chapter 1.2.1. Raman Spectroscopy Basics

Raman scattering of light is a natural phenomenon first discovered by Sir Chandrasekhara Venkata Raman, earning him the 1930 Nobel Prize in physics[12].

Most light scattered by molecules undergoes elastic Rayleigh scattering, by which process the scattered light retains the same energy (wavelength) as the incident light. A small fraction of light (~1 in $3x10^7$ photons), Raman found, is scattered inelastically. In Raman scattering the incident photon interacts with the vibrational excitation of a molecule or solid lattice, and the energy to the vibrational excitation is added or subtracted to the energy of the photon as it is scattered (Figure 1.1). In a Stokes transition the photon energy is reduced and in an anti-Stokes transition the energy increases. Whether, and to what degree a vibrational excitation mode will exhibit Raman scattering is determined by the change in the molecule's polarizability with respect to the vibrational (normal) coordinate. Detecting the Raman scattered light requires a monochromatic light source and a means to filter the much more intense Rayleigh scattered light. C. V. Raman accomplished this using sunlight and photographic filters.

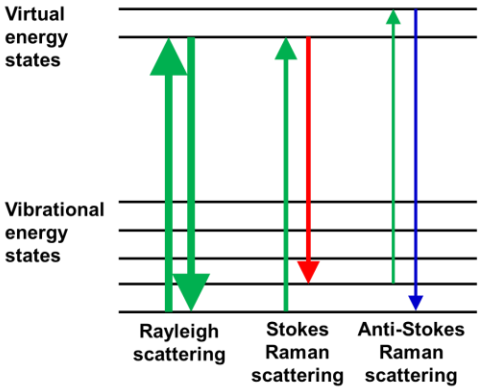

Figure 1.1: Schematic energy diagram Rayleigh scattering, and Stokes and anti-Stokes Raman scattering of light. Line thickness indicates the relative intensity (not to scale) of each form of scattering and color shows the red/blue shift of incident light.

Since the advent of the laser provided access to an intense monochromatic light source, Raman spectroscopy has been developed as a means to use Raman scattering to derive molecular information from materials. Because the energy of the incident light is shifted by an amount specific to the vibrational excitation of the material, that Raman shift can be used to identify the composition and bonding of the scattering material. Raman spectroscopy is often used to complement infrared (IR) spectroscopy, another vibrational technique. Since the IR selection rule dependent on the dipole moment instead to the polarizability different vibrational modes produce strong scattering in the two methods. Notably water, which often must be eliminated from sample to prevent its signal from obscuring of other peaks in IR spectra, is not a strong Raman scattering molecule. The sensitivity of the molecular vibrations of materials to the macroscopic and local state of the centers of vibration makes Raman spectroscopy useful in the measurement of a number of materials properties. For instance, in crystalline materials the width or shift of a peak representing a specific vibration can indicate lattice stress or deformation[13]. Alternatively, highly accurate optical measurements of temperature can be made the ratio of the Stokes and anti-Stokes peaks, which depends on the Boltzmann distribution of energy states[14]. Raman scattering is polarization dependent and can therefore be used to measure orientation of crystals, fibers or other anisotropic materials when a coherent light source is used[15–17]. In organic molecules peaks representing specific vibrations can be shifted or damped according to the polarity of nearby atoms, giving excellent chemical sensitivity among similar molecules.

The inherent problem most often encountered with Raman spectroscopy is the weak signal that arises from the low probability of a Raman scattering event. To overcome this, there have been a number of innovations that can dramatically increase signal intensity. For example, surface-enhanced Raman spectroscopy (SERS) boosts signal by adsorbing analytes a surface where surface plasmons increase field strength[18]. In resonance Raman spectroscopy the incident light is tuned to the energy of a specific electronic transition in a molecule of interest, greatly enhancing scattering[19]. Often, a simpler means of increasing signal are needed in practice. The use of a confocal microscope allows the incident light to be concentrated onto an area of interest and efficiently collected through an objective lens.

Chapter 1.2.2. Cartilage Disease

Articular cartilage provides joints with an effective viscoelastic cushion, composed of a solid and a fluid phase. This two-phase character is the essential basis for the functional properties of the tissue. As a joint is put under load the fluid phase, known as synovial fluid, is expelled. The resistance to this expulsion is what gives cartilage a relative high compressive modulus and provides the cushion effect necessary for physiological function. The detailed molecular composition and architecture of the extra-cellular matrix (ECM) produces these properties by maintaining a high osmotic swelling and low permeability (Figure 1.2). A swelling force is achieved through glycosaminoglycans (GAGs) containing a large number of

anionic sulfonate groups. The GAGs, mostly chondroitan sulfate, exist as side chains of brush-like proteoglycans, which aggregate as side chains on hyaluranic acid, a non-sulfonated GAG. A complex of type II collagen fibers, in turn, acts to confine the proteoglycans to a dense network that limits the permeability of the fluid phase.

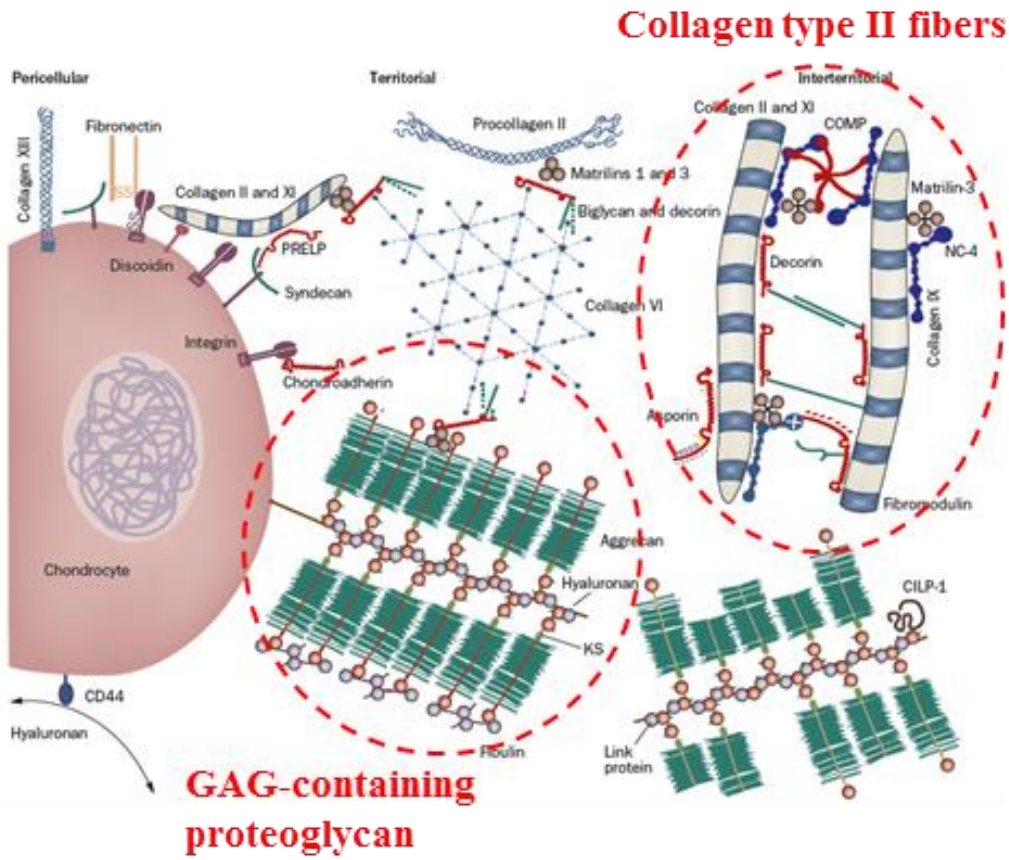

Figure 1.2: Illustration of the complex system of strutural and regulatory components of articular cartilage matrix. Glycosaminoglycan-containing proteoglycans and collagen type II fibers have been highlighted as critical elements of this mixture. Modified from Heinegård, D. & Saxne, T. Nat. Rev. Rheumatol. 7, 50–56 (2011)[20]

Disease in articular cartilage is characterized by the loss of this closely regulated structure-function relationship. The most pervasive disease affecting articular cartilage is osteoarthritis (OA), estimated to affect 67 million Americans by the year 2030[21]. While there are genetic and other risk factors, the root cause of the onset of OA remains largely unknown[22,23] In OA cartilage the normal maintenance of the balance of ECM components by chondrocytes is disrupted, causing the tissue to gradually degrade under biomechanical stress[20].

Current diagnostic methods often rely on direct observations by clinicians of morphological tissue abnormality or on changes in bulk properties, such as density, detected by radiology (*i.e.* x-ray or MRI)[24,25]. However, these gross changes in tissue characteristics are typically indicative of advanced pathological conditions, and moreover, represent secondary indicators of disease, which are frequently measured by qualitative or subjective means. Invasive and often counterproductive extraction of tissue samples for histological analysis is currently required to detect and measure the primary biochemical changes that occur in the extracellular matrix of pathological cartilage, such as reduced levels of glycosaminoglycans (GAGs). Stains such as toluidine blue can indicate the level of GAGs present in a sample and immunostaining can be used detect the presence of collagen II and other proteins of interest. These methods do not lend themselves to quantification and cannot illuminate structural organization at the molecular scale. More in depth characterization include dissociative biochemical assays such as polymerase chain reaction (PCR), which can only examine RNA-level gene expression in

chondrocytes[26,27], and enzyme-linked immunosorbant assay (ELISA)[28,29], a method of quantifying the relative compositions of pre-determined immuno-targets. Alternatively, biomarkers have been sought that can provide a simple blood test[30], but will likely always be more prone to misdiagnosis than interrogation of the effected tissue – articular cartilage. There is a current need for a minimally-invasive clinical cartilage evaluation tool that can examine these molecular changes, with the sensitivity to detect disease in pre-clinical patients.

Chapter 1.2.3. Raman Spectroscopy for Medical Diagnostics

Raman spectroscopy holds great promise as a biomedical diagnostic tool. Tissues contain a tremendous variety of biomolecules, all constructed from a relatively few number of building blocks (e.g. amino acids, nucleic acids, sugars). The incredible specificity evolved in nature has been used in many immunochemical diagnostic methods to overcome this inherent similarity. These immunological methods, however, are limited to a few molecules of interest to measure, which must be known *a priori*. The sensitivity of Raman spectroscopy to small chemical and physical changes in a material preserves, in an ideal spectrum, the collective differences between the sets of biomolecules in even two extremely similar tissue samples. Additionally, Raman spectroscopy presents a potentially minimally-invasive optical means of characterizing the biochemical state of tissues *in situ* through the use of endoscopes.[31] Historically most utilized in materials chemistry, Raman spectroscopy has only recently gained significant recognition as a tool for

biomedical diagnostics.[32–34] Raman has been shown capable of detecting differentiation in stem cells[35,36] and demonstrated as method of monitoring blood[37]. However, most research into potential Raman diagnostic methods has focused on cancer[33,37–42]. Some of these still rely on immunospecificity of conjugated SERS tags[43], though many others detect signs of cancer purely spectroscopically. The detailed characterization of cartilage by Raman spectroscopy has been demonstrated, though much of the work to date has focused on demonstrating the compositional sensitivity of the method for healthy cartilage tissue. [44–46] At the core of an effective diagnostic method is the ability to correctly distinguish healthy tissues from diseased. It follows from this that the development of a spectral diagnostic for OA should focus on considering the spectral differences between healthy and representative pathological cartilage. This has been shown feasible with the experiments on the synovial fluid from healthy and OA patients.[47] What remains to be shown is a full scale demonstration of the direct diagnosis of cartilage disease.

Chapter 1.3. Human Pluripotent Stem Cells

Chapter 1.3.1. Pluripotent Stem Cell Fundamentals

The National Institutes of Health describe stem cells as distinct populations of unspecialized cells that are capable of dividing and renewing themselves for long periods and that can give rise to specialized cell types.[13] A pluripotent stem cell is one that can differentiate to cells from all three embryonic germ lineages (endoderm, mesoderm, ectoderm). The first human pluripotent cell type to be

derived was human embryonic stem cells (hESCs). HESCs are derived by culturing the inner cell mass of a blastocyst stage embryo under specific conditions[48]. These cells can be expanded indefinitely in a pluripotent state if provided with the appropriate combination of growth factors, which has conventionally been done by co-culture with mouse embryonic fibroblast (MEF) feeder cells. In 2007 Yamanaka demonstrated the ability to create human induced pluripotent stem cells (hiPSCs) through the transduction of pluripotency transcription factors in adult somatic cells in culture[2]. These cell lines exhibit the same pluripotent behavior as hESCs[7,8], but do not require the destruction of an embryo. HiPSCs also offer the advantage of being able to derive them from the patient in which differentiated cells will be used for therapy, avoiding possible immune rejection.

Several persistent problems have been noted with the conventional methods of culturing hPSCs including the risk of xeno-contamination from the MEF co-culture or other animal derived products[49,50], frequent acquisition of chromosomal abnormalities[51], a heterogeneous cell state[52–54], as well as poor reproducibility between laboratories. To eliminate xeno-contamination a number of research groups have established defined substrates and media that permit long term hPSC culture[9,11,55–58]. The pluripotent state has been well defined by the transcriptional characteristics of hPSC populations. The transcription factors OCT-4, SOX2 and NANOG, as well cell surface proteins such as SSEA-4 and E-cadherin are all consistent

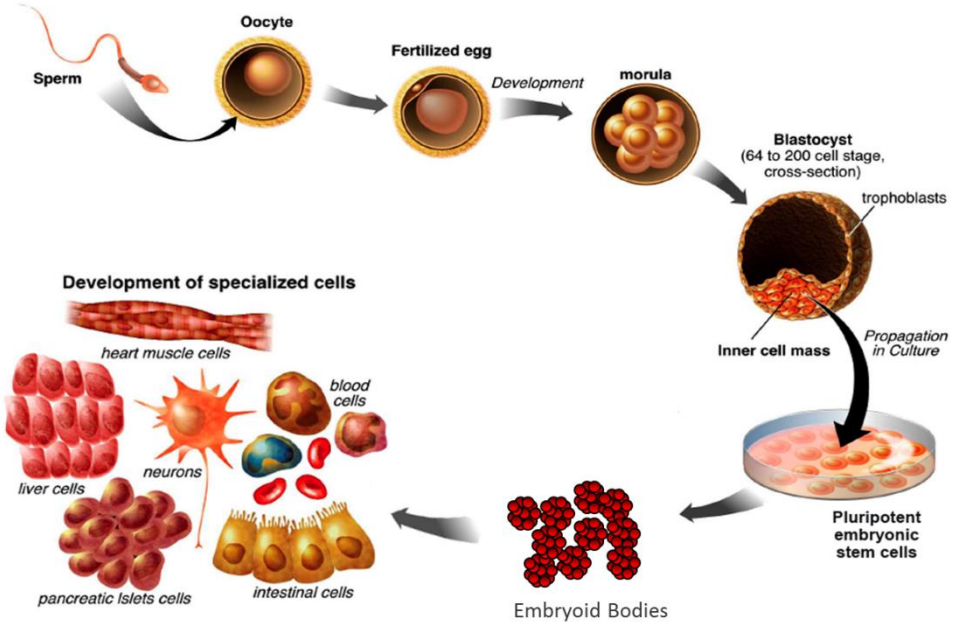

Figure 1.3: Diagram showing pictorially the process by which embryonic stem cells are derived from an embryo, expanded in a pluripotent state, and eventually differentiated to the specialized cells needed for potential therapies. Modified from Hall, CIRM 2005.

indicators of pluripotency between hPSC cultures. However, there exists a substantial heterogeneity in the expression of these and other pluripotency markers when examined on a single cell level[52–54,59–61]. This phenomenon might be linked to the observed problems with reproducibility and could have important implications for the ability to efficiently direct differentiation towards the specified cells needed for therapies[59].

Chapter 1.3.2. Patterning of Stem Cells

The heterogeneity of cell states found in culture can be limited by reducing the heterogeneity of local conditions imposed on hPSCs. To achieve this several

groups have taken the approach of confining PSC growth to colonies of uniform size and shape using microwells[62,63], stencils[64] or micro-contact printing[65–68]. While microwells and stencils provide a physical barrier to limit colony expansion, these methods can introduce additional complications either from difficulty of use in the case of stencils or integration of microwell topology with conventional culture method developed to handle planar substrates. Alternatively micro-contact printing (μCP) provides a convenient method to introduce colony confinement in concert with existing culture methods, and has been demonstrated capable of influencing the differentiation potential of hPSCs[65].

The materials and methods of μCP were pioneered by Whitesides and colleagues[69], who later applied these techniques to patterning in biological systems[70–73]. Most commonly a pattern design is replicated in negative out of a photoresist material on a silicon wafer using photolithographic methods barrowed from microelectronics processing. This negative is then used to cast a stamp in a polydimethylsiloxane (PDMS) elastomer with raised features representing the pattern to be printed. This stamp is "inked" with a solution of a compound that will react or bind to the surface to be stamped. The solution is dried and the features of the stamp are pressed into conformal contact with the surface. Self-assembled monolayers (SAMs) of alkanethiols are often used as a μCP system in which alkanethiols comprise the "ink" solute and the surface is gold or another noble metal. The sulfur of the thiol will rapidly form a covalent bond with the gold surface,

evolving hydrogen. The mobility of the surface gold atoms permits rearrangement of the bound alkanethiols to align the hydrocarbon chains at a cant angle that maximizes van der Waals interactions between them. This results in the assembly of dense monolayers presenting whatever chemical functionality is present on the end opposing the thiol on the alkanethiol. After printing a second SAM can be formed from solution in the unprinted regions.

Micro-contact printing can direct the patterning of cells using SAMs on gold[70,74–76], or by directly printing of proteins to guide cell attachment[65,66,77,78]. In the case of SAMs, the functionality presented by the monolayer can be designed to bind proteins through physical interaction[67,75,76], or it can be a peptide or other molecule with biological specificity[79]. The second non-adherent SAM typically has an oligomeric ethylene glycol functionality that resists protein adhesion through the tight binding of water to this type of molecule[80]. When proteins are directly printed the background can be rendered non-adherent by treating with a poly(ethylene glycol)-b-poly(propylene oxide)-b-poly(ethylene glycol) block copolymer[81]. While direct printing is inherently simple, the use of SAMs offers a more versatile system for controlling surface functionality and studying the broader effects of patterning cells.

Chapter 1.4. Tissue Engineering Scaffolds

Chapter 1.4.1. Tissue Engineering Materials

Langer and Vacanti describe tissue engineering as applying the principles of engineering and life sciences toward the development of biological substitutes that restore, maintain, or improve tissue function or a whole organ[82]. Suitable materials for use in tissue engineering are limited by the constraints of biocompatibility. Materials must possess the properties that allow them to function in harmony with cells to recreate a tissue. By and large, with the exception of materials for the regeneration of bone[83], the class of materials found to have the versatility to serve this function has been polymers. Polymers used in for tissue engineering can be categorized into two broad functional classes. Hydrophobic polymers form dense solid structures that can provide high modulus cues to cells and support mechanical loads. Hydrophilic polymers chains are soluble in water and when crosslinked into a 3-D network form a hydrogel.

Bioresorbable polyesters are the most extensively used class of hydrophobic polymers in tissue engineering[84,85]. Most often the ultimate function of polymer scaffold material depends on its ability to disappear over time as the tissue matures. Bioresorbable polymers degrade within the body into products that the body can either metabolize or remove without toxicity[85]. Poly(lactic-co-glycolic acid) is a polyester that has been widely implemented as a bioengineering material[86–103] (Figure 1.4a). PLGA makes an extremely attractive candidate material in many tissue engineering applications because it processes a unique combination of properties. Perhaps most critically PLGA has been demonstrated to be non-cytotoxic, bioinert and bioresorbable, earning it FDA approval for use in drugs and

implanted biomedical devices[86]. Degradation of PLGA, like other degradable polyesters, occurs by hydrolysis of backbone ester linkages in aqueous environments. As this process occurs water is absorbed into the polymer and the entire structure degrades uniformly[104,105]. This process, accelerated by enzymatic activity, results in a total degradation time *in vivo* for typical implanted structures in the range of months, an ideal time-frame for replacement of scaffold materials by regenerated tissues. In PLGA this time-frame can be further tuned by adjusting the ratio of lactic to glycolic monomer units[104,106]. PLGA is also easily processable in a variety of organic solvents or as a melt at relatively low temperatures. This has allowed for emulsion processing of PLGA into particles for the encapsulation of hydrophobic drugs or aqueous protein-based pharmaceuticals in double emulsions[99,102,103,106,107]. PLGA is also attractive because it can be processed by a number of methods into a variety of 3-D structures and easily functionalized[108] .

A number of natural and synthetic polymers have been formed into hydrogels for tissue engineering applications. Natural polymers such as chitosan[109], dextran[110–112], fibrin[113] and alginate[114–116] offer better biocompatibility, while synthetic polymers, often utilizing a bioinert PEG functionality[110,117], are more easily modified for targeted functionality[118]. Alginate is an anionic polysaccharide derived from algae (Figure 1.4b). The protonated form, alginic acid, is treated to make the sodium alginate salt. This form is highly soluble in water and is used as a thickening agent in some applications. Exchanging the sodium ions in a solution of sodium alginate for calcium or other divalent ions results in the rapid formation of a gel.

This biocompatible gelation method has made alginate a popular material for the encapsulation of cells in culture[119]. Calcium alginate gels can be dissolved under mild conditions by chelating the calcium ions to regenerate the soluble form of the

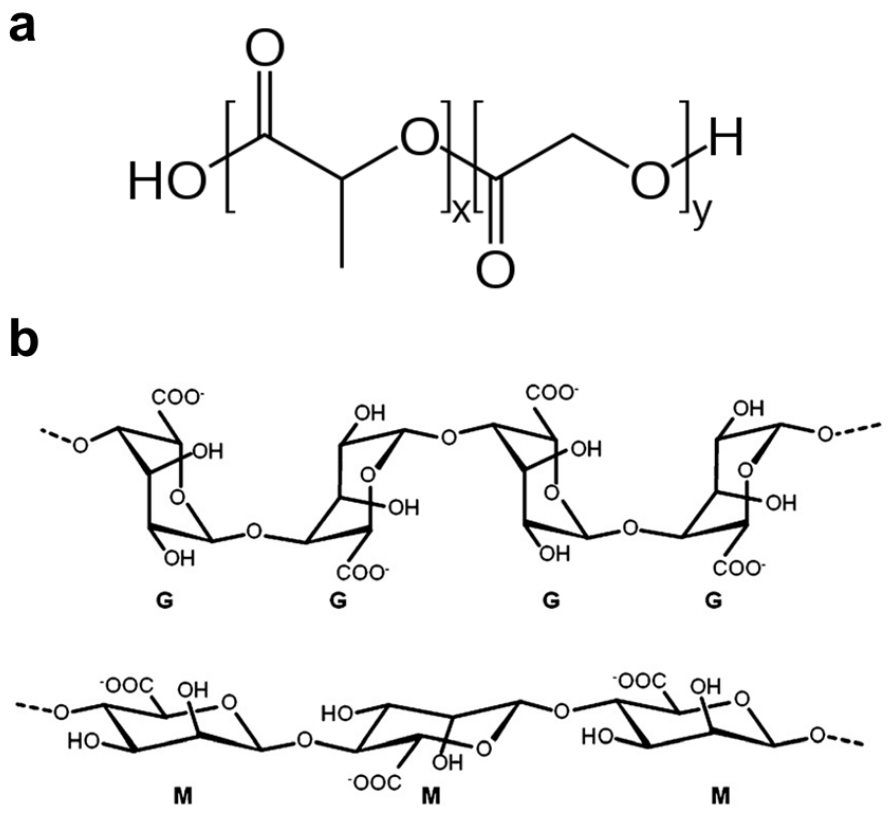

Figure 1.4: (**a**) Structure of poly(lactic-co-glycolic acid) (PLGA) where "x" indicates the number of lactic acid repeating units and "y" the number of glycolic acid repeating units. (**b**) The structure of G (top) and M (bottom) blocks of alginate.

polymer. When alginate has been employed in template scaffolds it has been used as the permanent continuous phase rather than sacrificial porogen of the

structure[120–122]. A few instances have shown the potential of alginate as a porogen that can be extracted under mild aqueous conditions[123,124], though the work presented in Chapter 4 is believed to be the first to use alginate beads to directly template the porous structure of a tissue engineered organoid.

Chapter 1.4.2. Methods for Structuring Scaffolds

A number of methods have been developed to control internal structure of cellular scaffolds made from hydrophobic polymers. Generally these scaffolds are formed either from fibers or a continuous porous structure. Fibers of polymers, including degradable polyesters, can be formed by electrospinning solutions in organic solvents[90]. Scaffolds prepared from fibers provide good mechanical strength in the fiber direction and direct the cells to grow along fibers to form unique tissue structures. Defining a scaffold's structure by including porosity offers more diversity in the possible 3-D architecture. Among the ways to introduce porosity are through gas foaming or the use of templates. Gas foaming produces highly porous structures, but require specialized equipment and result in pore sizes that can be difficult to control[125]. Templating pores with a second material that is later removed offer greater control of the final structure. The second material can be particles of wax[126], an inorganic salt[105], a sugar[104], or another material that will not dissolve when mixed with an organic solvent solution of the scaffold polymer.

A widely recognized advantage of employing a hydrogel in a tissue engineered scaffold is that cells can be encapsulated and cultured while dispersed in 3-D[127]. To

achieve this encapsulation, the soluble linear chains of the hydrophilic polymer must be crosslinked with the cells present. Photopolymerization has been successfully employed to encapsulated cell, but care must be taken as both the high intensity light and the polymerization propagating radicals can harm cells[117,128]. Alternatively, mild chemical reactions have been developed to rapidly form gels when a crosslinking molecule is mixed[110–112]. These chemical methods are gentler on cells but limit methods of gel formation. The templating has also been utilized in hydrogel scaffolds. Recent work demonstrated the use carbohydrate glass lattices to template a perfusable vascular network[129].

Chapter 1.4.3. Tissue Engineering of Cartilage

Considerable work has been done to develop bioartificial cartilage constructs. The focus of this effort has been on the use of hydrogel materials since the cartilage matrix has the properties of a hydrogel[130]. Once again, both synthetic and natural polymers have been used[131], but there is still no consensus of the best materials going forward. A number of promising results have shown that constructs produce cartilage like matrix[132–134] and can function in animal models[135], but an effective cartilage replacement therapy has not yet been realized.

Chapter 1.4.4. Tissue Engineering of the Lung

Due to its structural complexity relatively little work has been done to attempt the engineer replacement of lung tissue. The use of synthetic scaffolds has been

attempted using degradable polyesters[136], but this approach has by and large been abandoned for a lack of materials that can provide the properties of native lung ECM[137]. The most successful attempts to develop lung tissue *in vitro*, like early efforts in other organs, has relied on the use of decellularized donor lung tissue[137,138]. These biological scaffolds guide the development of tissue histologically similar to lung, but have produced low survival rates in animal model implantation studies[139].

Chapter 2. Multivariate Raman Analysis of Cartilage Disease

Chapter 2.1 Introduction and Motivation

Degenerative diseases of articular cartilage, such as osteoarthritis (OA), represent a widespread clinical challenge with deficient early diagnostic and treatment options available[21]. Current diagnostic methods often rely on direct observations by clinicians of morphological tissue abnormality or on changes in bulk properties, such as density, detected by radiology (*i.e.* x-ray or MRI)[24,25]. However, these gross changes in tissue characteristics are typically indicative of advanced pathological condition, and moreover, represent secondary indicators of disease, which are frequently measured by qualitative or subjective means. Alternatively, biomarkers have been sought that can provide a simple blood test[30], but will likely always be less sensitive than interrogation of the effected tissue – articular cartilage. Invasive and often counterproductive extraction of tissue samples for histological analysis is currently required to detect and measure the primary biochemical changes that occur in the extracellular matrix of pathological cartilage, such as reduced levels of glycosaminoglycans (GAGs). There is a current need for a minimally-invasive clinical cartilage evaluation tool that can examine these molecular changes, with the sensitivity to detect disease in pre-clinical patients. In addition, such technique could be enlisted to guide the development of engineered cartilage replacement tissue by providing routine feedback on the similarity between construct and native cartilage ECM.

Raman spectroscopy presents a potentially minimally-invasive[31] optical means of characterizing the biochemical state of tissues *in situ*, thus providing the possible basis of a sensitive early diagnostic tool[32,34]. This label-free characterization approach is achieved by inelastic Raman scattering, which reflects the distinctive molecular vibrational states of a material. Though conventionally utilized in materials chemistry, Raman spectroscopy has recently gained significant attention as a tool for biomedical characterization[33]. Importantly, the detailed characterization of cartilage through the use of Raman spectroscopy has already been demonstrated[44–46]. Although much of the work to date has focused on demonstrating the compositional sensitivity of the method for healthy cartilage tissue, this technique can now be expanded to more direct application to diagnostics. At the core of an effective diagnostic method is the ability to correctly distinguish healthy tissues from diseased. It follows from this that the development of a spectral diagnostic for OA should focus on considering the spectral differences between healthy and representative pathological cartilage[47].

In the research presented here, we demonstrate the potential for a Raman diagnostic method by taking this type of comparative approach (Figure 2.1). We have made analytical comparisons of Raman spectra from three different pairs of model training materials, with one member of each pair being representative of healthy cartilage and the other of pathological cartilage. From this analysis we have created diagnostic metrics on which a spectrum's score indicates its similarity to one material or the other. We have hypothesized that these scores will serve to

distinguish healthy from osteoarthritic cartilage. In addition, we hypothesize that by combining two or more metrics derived from different pairs of training materials we can create a redundancy of classification that will identify spectra that are misclassified by single metrics due to obscured spectral information in noisy spectra. Our results show that normal articular cartilage can be distinguished from pathological cartilage tissue with altered levels of collagens and/or GAGs by our method. The three metrics reported here are derived, respectively, from human normal articular cartilage and human osteoarthritic cartilage characterized by low GAGs and reduced collagen type II, rat articular cartilage and rat injury-induced fibrocartilage rich in collagen type I, and also collagen type II and collagen type I alone.

To create these metrics we employed a multivariate analysis of sets of spectra from the training materials. The complex biomolecular composition and organization within a biological sample lead to a continuous series of vibrational bands which result from a variation in the local bonding environment of the different biological building blocks (*i.e.* amino acids, lipids, sugars, nucleic acids). The detailed information encoded in this complexity provides the basis of sensitive spectral classification. Variation in the spectra of complex tissues can be thus seen as means of comparison in a parameter space with dimensionality equal to the number of wavenumbers scanned. While univariate analysis of spectral intensity at specific wavenumbers can be useful for examining specific known changes[44,45,140], this traditional approach discards a majority of these dimensions, and with them

most of the information obtained with a Raman spectrum. Multivariate methodologies consider all or most of the wavenumber dimensions simultaneously, and have been shown to be effective in characterizing vibrational spectra of cartilage[44,141,142].

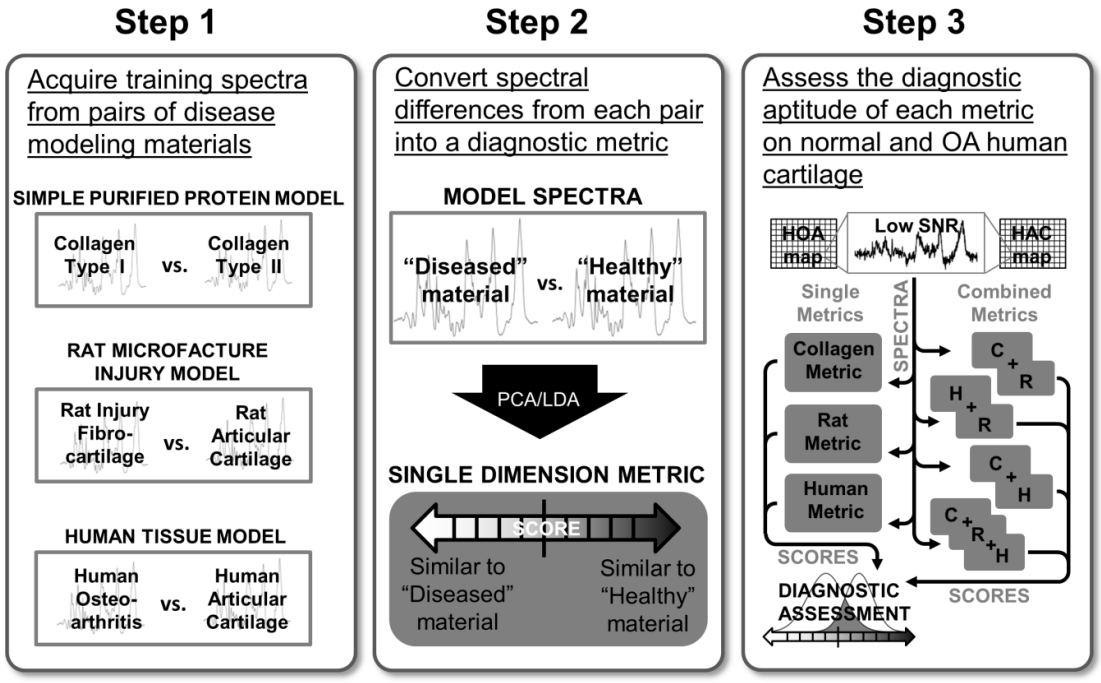

Figure 2.1: A schematic representing the experimental process presented in this report. Abreviations: OA (osteoarthritis), HOA (human osteoarthritis), HAC (human articular cartilage), SNR (signal-to-noise ratio), C (collagen metric), R (rat metric), H (human metric)

The multivariate method we have utilized combines principal component analysis with linear (Fisher) discriminant analysis. Principal component analysis (PCA) is a numerical method used to reduce the dimensionality of a dataset while retaining a majority of the useful information it contains. This is achieved by

transforming the original variables (wavenumbers) into a new, equal number of variables called principal components (PCs). PCs are orthogonal linear combinations of the original variables and are ordered by the amount of the variance for which each PC accounts within the dataset. This ordering of the PCs permits many of the higher order PCs to be discarded without losing a significant amount of information regarding variation within the dataset. PCA is often combined with linear discriminant analysis (LDA) so that the resulting analysis is termed PCA-LDA. LDA also involves a linear change of basis, but unlike PCA, the linear combination of original variables that is calculated is the one that maximizes the ratio of between-group variance to within-group variance. Groups correspond to two known classes (training materials) to which individual observations (data points) in the dataset are assigned. In a geometric sense this chooses the direction in multidimensional spectral space along which the data best separates into its assigned classes. The projection of an individual spectrum onto this new axis is that data point's LDA score. However, the number of variables input into an LDA must be smaller than the number of observations. This is accomplished by reducing the dimensionality of the Raman data using PCA. After applying the combined PCA-LDA to training spectra from two different tissues or materials, scoring any spectrum on the axis derived from the analysis will quantify its characteristics with respect to the characteristics that most effectively distinguish those two training classes.

We have found that combining Raman spectroscopy with multivariate analysis was effective at producing three classification metrics based on the distinct

scoring of each training set pair. Additionally, each of the metrics produced has been demonstrated to classify low SNR spectra from healthy and osteoarthritic cartilage as predicted, according to similarity with the training materials represented in each metric. Finally, we have shown that these metrics can be combined to improve the misclassification rate over any single metric for the same low SNR spectra.

Chapter 2.2. Experimental Methods

Chapter 2.2.1. Materials

Human normal and osteoarthritis cartilage specimens (International Cartilage Repair Society (ICRS) grade 2-3 were obtained from either National Disease Research Interchange (NDRI) or Dr Marcel Karperien (University of Twente, Netherlands). Wild type Sprague-Dawley adult 3-4 month old male rats from Charles River (San Diego, CA) were used for animal studies. Optical quartz was purchased from Ted Pella.

Chapter 2.2.2. Rat injury model

The surface joint defects were generated in the femoral intra-condylar region of a knee joint in rats using methods previously described[143]. Briefly, the rats of 11 weeks old were anesthetized and medial para-patellar arthrotomy were carried out under a dissection microscope (Olympus, USA) using procedure previously described. Full-thickness osteochondral defects were made with special metal tools. At week 4, rats were sacrificed and dissected for examination.

Chapter 2.2.3. Raman sample preparation

Tissue samples for Raman analysis were prepared by fixing samples in {2%} paraformaldehyde then embedding in paraffin wax for sectioning. Sections 10 microns thick were prepared on quartz microscope slides and wet-mounted under 0.25mm quartz coverglass to avoid fluorescence from standard soda-lime glass.

Chapter 2.2.4. Raman spectroscopy

Raman spectra were acquired with a Renishaw InVia micro-Raman spectrometer equipped with a 1800 lines mm^{-1} grating, Rayleigh line rejection edge filter, Peltier-cooled deep depletion CCD array detector (576 x 384 pixels). The excitation source was the 514 nm line from argon ion laser at 25 mW. A 63x/1.2NA water-immersion objective was used to produce a spot size of approximately 1 μm on the sample. Spectra used to create training sets were acquired by collecting data for 300 seconds following 60 seconds of photo-bleaching. In the case of cartilage these were obtained from matrix in the interterritorial regions of the middle zone. Spectral maps were prepared using an XYZ automated mapping sample stage with 0.1μm step size, and an individual spectral acquisition time of 30 seconds with 30 seconds of photobleaching.

Spectral training sets were derived from 48 rat articular cartilage (RAC) spectra and 59 rat injury-formed fibrocartilage spectra (RIF); 80 human adult articular cartilage (HAC) spectra and 80 osteoarthritis-effected cartilage (HOA) spectra; and 16 purified collagen type II (CL2) spectra and 16 purified collagen type I (CL1) spectra.

Chapter 2.2.5. Multivariate data analysis

Spectra were prepared for analysis by first truncating the data to include wavenumbers from 650 to 1800 cm^{-1}. Sample spectra, as well as spectra taken from blank areas on the same samples (*i.e.* water and quartz only) were then both subjected to a modified range-independent algorithm to remove background fluorescence not eliminated through photobleaching[144]. An average of the cleaned blank spectra was then subtracted from the cleaned tissue spectra. Each modified tissue spectrum was then leveled and normalized to its standard deviation. Using built-in functions in Matlab (Mathworks), PCA was first performed on the combination of two training sets to obtain PCs representing the variance of the combined data set. LDA was then performed using these PCs as the input variables to determine the spectral features that best differentiate between the two training sets.

To improve the quality of our classification, training sets were subjected to an iterative leave-one-out (LOO) method. The leave-one-out procedure is often used as a means of validating such PCA-LDA analyses[145]. In this procedure, each observation (spectrum) is tested by removing it from the set prior to analysis, running the analysis without it, then applying the resulting classification metric to the removed observation and examining if it was classified correctly. In our method each incorrectly classified spectra was removed from the data set and the process was repeated. Because removing all misclassified spectra at once will affect the overall analysis, new misclassifications can be produced. This iteration was repeated until no further misclassifications were produced. Misclassification was

defined as a PCA-LDA score of the opposite arithmetic sign from what was designated for the spectrum's class.

The number PCs input into the LDA was varied between 2 and 20 and the analysis, including the iterative leave-one-out, was repeated for each increment. The number of PCs used in the final analysis was determined by measuring the spread of the training set PCA-LDA scores, defined as the difference of the mean score of each set, divided by the sum of the standard deviation of two sets. The highest number of PCs after which no further increases in this value was observed was the number of PCs used in the analysis. In this way, over-fitting[146] is avoided.

Chapter 2.2.6. Spectral map construction

Spectral maps are color-coded representations of LDA/PCA scores collected at regular intervals in a 2-dimentional array on a sample. Sample scores equal to the mean score of the first training set (cartilage-like) are mapped as blue, a score equal to the mean score of the other training set (pathological-like) is mapped as red and intermediate scores as a linear mix of red and blue. Scores falling outside the means are represented as a linear mix of black with either red or blue, becoming fully black at a score of three times the training set mean with the same arithmetic sign. Each pixel in a map represents a square the size of the distance between acquisition spots and no smoothing algorithm is employed between pixels.

Chapter 2.3. Results

Chapter 2.3.1. Rat injury model

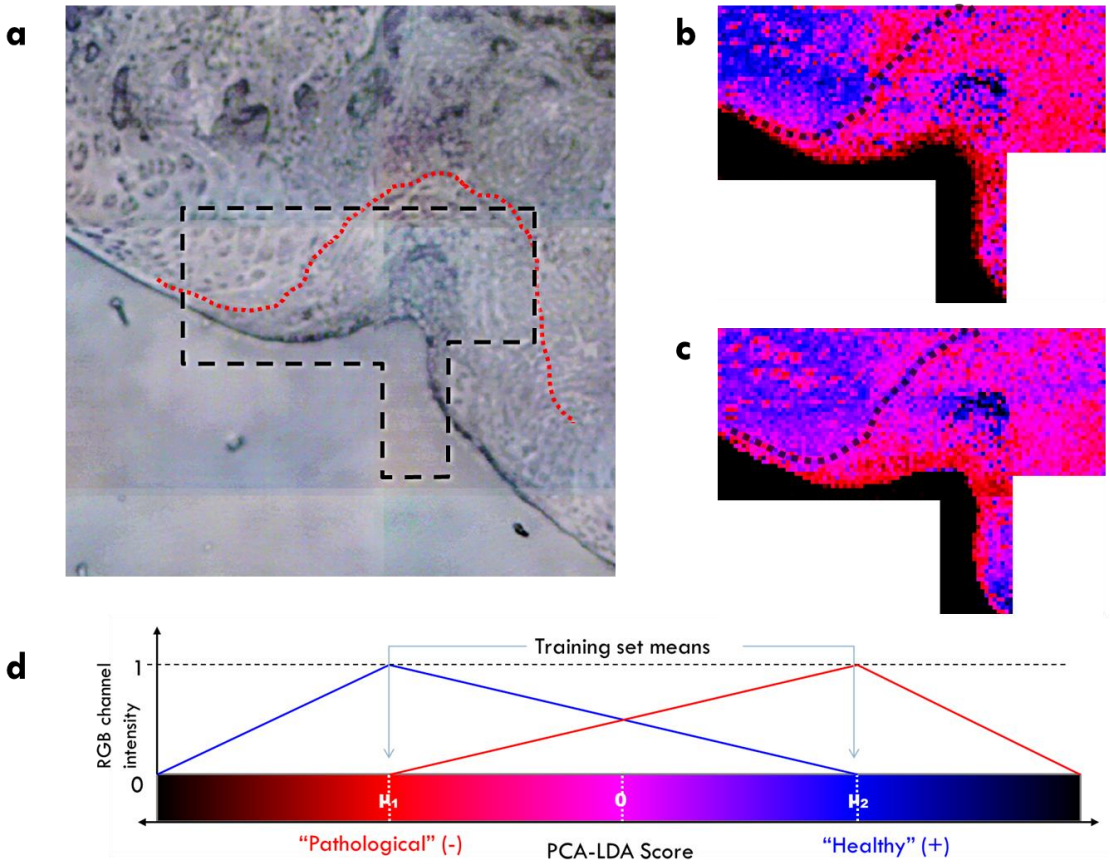

Figure 2.2. (**a**) A phase contrast image of a 10 µm-thick cross-section of surgically injured rat patellar articular cartilage, 4 weeks post-injury. The red dotted line indicates the approximate injury site. The black dashed line marks the region covered by spectral Raman mapping. (**b**) Raman spectral map for which the coloration of each pixel (7 µm x 7 µm) represents the rat metric PCA-LDA score of the low signal-to-noise spectrum taken at that location. (**c**) Raman spectral map scored with the collagen metric. (**d**) Schematic of the relationship between a spectrum's score and its representative color

Microfracture surgery is an articular cartilage repair surgical technique that works by creating tiny fractures in the underlying bone. The fibrocartilage tissue that results does not exhibit the same biomechanical functionality as native cartilage and the operation produces mixed outcomes for patients. We have employed an

analogous surgery in rats to model the molecular differences between healthy cartilage and the functionally similar but defective fibrocartilage produced in the injury site.

The surgical injury to the rat femoral head produced the expected formation of a fibrotic tissue filling much of the cavity of the wound 4 weeks after the surgical procedure. A cross sectional micrograph in Figure 2.2a shows a clearly distinguishable morphological boundary between the injury site and adjacent native cartilage. Images of sections stained for the presence of GAGs, as well as collagen type I and II are reported in Figure 2.3.

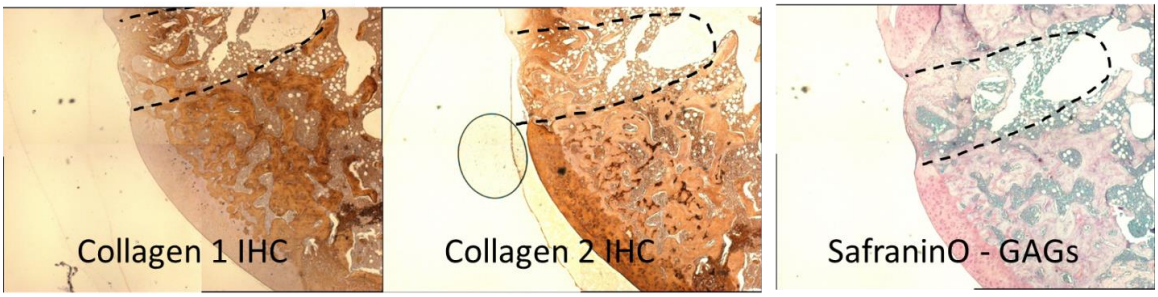

Figure 2.3: Brightfield images of the sections taken from the rat microfracture injury model 4 weeks post injury and stained for **(a)** Collagen type I - immunohistochemical, **(b)** Collagen type II - immunohistochemical, and **(c)** glycosoaminoglycans – SafraninO.

Chapter 2.3.2. Raman spectra

Raman spectra were obtained from three pairs of materials, each modeling the healthy and pathological cartilage in a different way. Comparison of spectra from two purified collagen isoforms provides a simplified model of the disruption of collagen type II in the matrix of diseased cartilage. The spectra obtained from the rat

injury model present an exaggerated model of dysfunctional cartilage. Human osteoarthritic cartilage offers a direct model of cartilage disease. These model spectra are then used for training a diagnostic method to distinguish healthy from diseased cartilage.

The average spectrum for each training material, after background and fluorescence removal, is represented in Figure 2.4a. The average spectra for tissue and collagen samples are each similarly characterized by several prominent Raman bands – the complex amide I band (1665 cm^{-1}), the C-H stretch band (1451 cm^{-1}) and the amide III band (1245 cm^{-1}) dominate the higher wavenumbers, while the sharp peak associated with the phenylalanine ring-breathing mode (1004 cm^{-1}) as well as several C-C bands assigned to the protein backbone (940 cm^{-1}, 816 cm^{-1}), proline ring (922 cm^{-1}, 857 cm^{-1}) and hydroxyproline (922 cm^{-1}) are prominent in the lower wavenumbers. The complete list of peak assignments is compiled in Table 1. All of these features are consistent with published spectra from other sources[31,45,147,148]. The similarity of all of the tissue-derived training spectra highlights the benefit of employing a multivariate analysis that can rely on many small variations. The strong resemblance between the tissue spectra and purified collagen spectra suggests that the Raman scattering from the collagen component of cartilage tissues may dominate due to a combination of concentration and scattering efficiency.

Chapter 2.3.3. PCA-LDA metrics

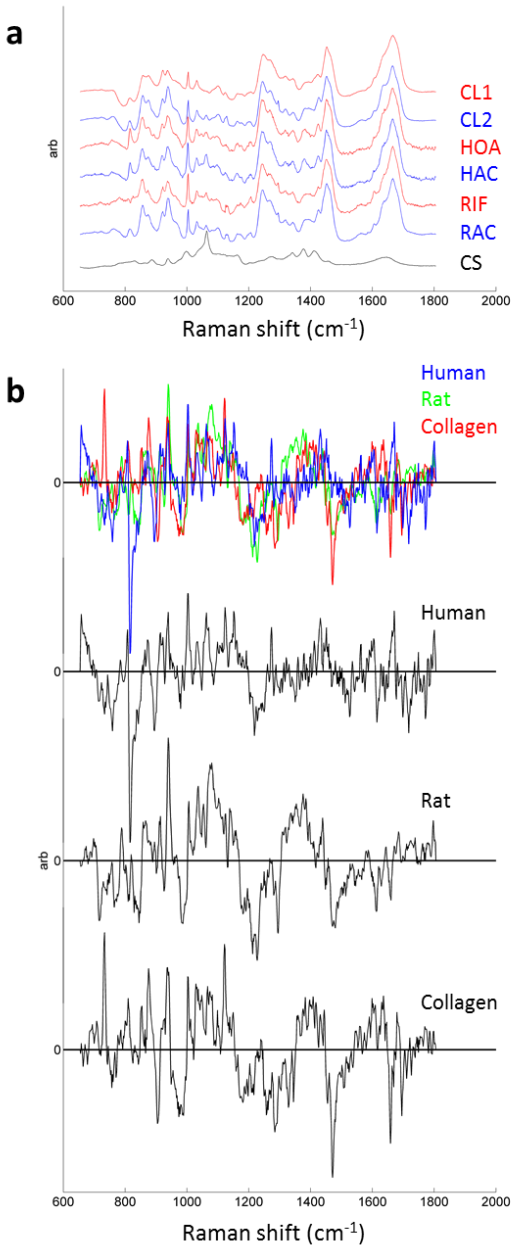

Table 2.1: Raman peaks and their assignments

Peak	ref.		Assignment
1665	b,c	s	Amide I
1637	c	sh	Amide I
1606	c,d	w	Phe, Tyr
1560	b	br	Amide II
1460	c	sh	CH2 def.
1452	a,b,c	s	CH2 def.
1442	a	sh	CH2 def.
1425	c	m	COO- (GAGs)
1390	c	m, br	unassigned
1343	c,d	w	CH2 wag.
1319	c,d	w	CH2 twist
1295	a,d	sh	CH2 def
1270	c	s	Amide III
1245	c	s	Amide III
1207	b,c,d	m	Hypro, TYr
1165	c	w	C-C/C-N str.
1130	c	w	C-N str.
1070-1100	c	w	PO2- str. (DNA/RNA)
1062	a,b,c	m	OSO-3 symm. str. (GAGs)
1031	d	s	Phe C-H in-plane
1004	a,b,c,d	s	Phe ring breathing
965	c	w	Amide III'
940	b,c,d	s	C-C protein backbone
922	a,c	sh	C-C Pro
874	a,b,c	s	C-C Hyp
857	a,b,c,d	sh	C-C aromatic amino acid
817	c	s	C-C protein backbone

Abbreviations: s (strong), m (medium), w (weak), sh (shoulder), def (deformation), str (stretching), wag (wagging), Phe (phenylalanine), Tyr (tyrosine), Pro (proline), Hypr (hydroxyproline)
Refs: (a) Esmonde-White 2011, (b) Bonifacio 2010, (c) Fruchour 1975, (d) Notingher 2004

Figure 2.4: (**a**) The average spectra for the training sets acquired from rat articular cartilage (RAC), rat injury-induced fibrocartilage (RIF), human articular cartilage (HAC), human osteoarthritic cartilage (HOA), purified collagen type II (CL2), and purified collagen type I (CL1). Also included for reference is the average spectrum from 15 spectra taken from purified chondroitin sulfate (CS). (**b**) PCA-LDA coefficients for the metrics from the HAC vs. HOA (Human), RAC vs. RIF (Rat), and CL2 vs. CL1 (Collagen) analyses.

PCA-LDA metrics are the result of a statistical comparison of Raman spectra from the pairs of training materials. They provide the means of distinguishing spectra from healthy and pathological cartilage. We produced three PCA-LDA metrics (HAC vs. HOA, RAC vs. RIF, and CL2 vs. CL1) that were all demonstrated to distinguish between their respective pairs of spectral training sets. The classification of each metric was optimized by limiting the number of PCs considered as variables in the LDA portion analysis, and by removing poor training examples through the iterative LOO method. The human, rat, and collagen metrics were derived to produce a maximum separation of their corresponding training spectra distributions by using 17, 12, and 12 PCs and removing 1, 5, and 3 misclassified training spectra, respectively. The distinct distributions of PCA-LDA scores for the training sets can be seen in Figure 2.5a.

The collagen metric achieved the greatest separation of its training classes (*i.e.* narrower class score distributions and greater difference between mean class scores), likely reflecting the simplified task of distinguishing purified training materials as opposed to the complex organizations of multiple macromolecules presented by whole tissues. Meanwhile the distinct distributions of the training scores for the human and rat metric demonstrate the sensitivity of this multivariate method to the molecular changes in cartilage that characterize the progression of osteoarthritis, as well as those changes induced by injury.

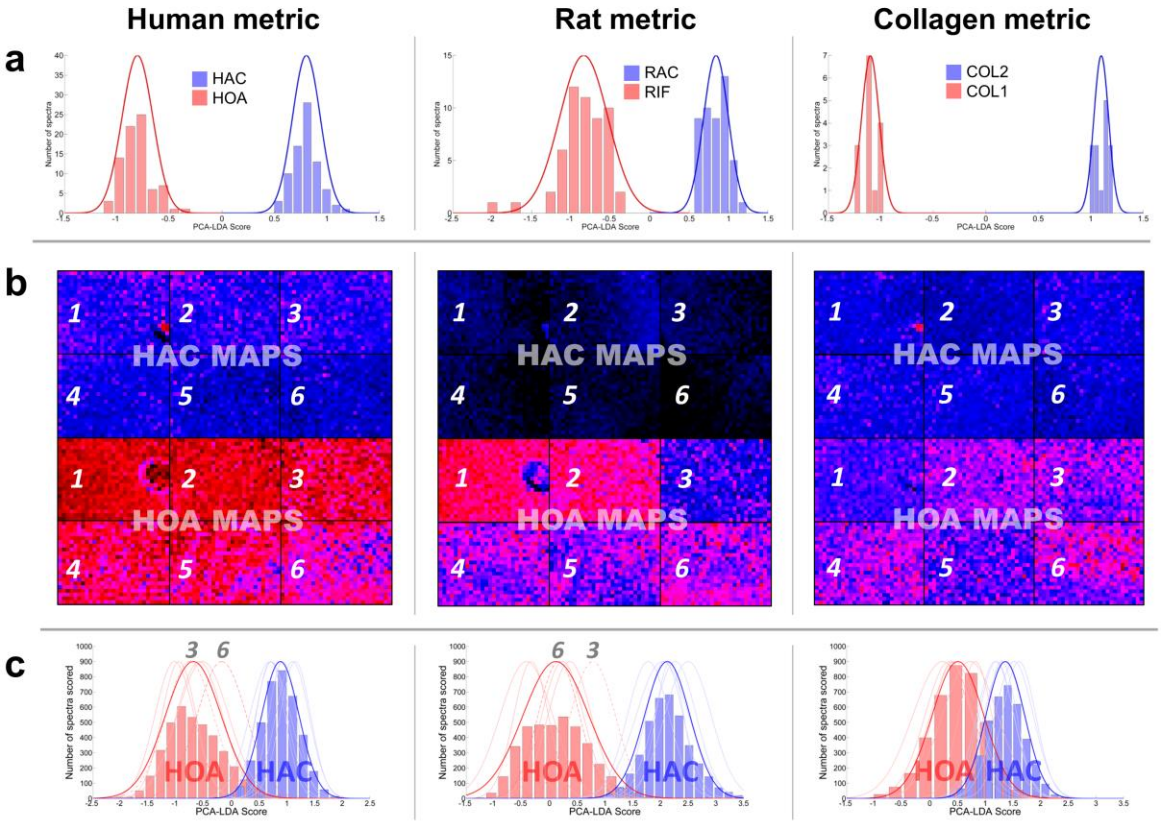

Figure 2.5. (**a**) Histograms (red and blue bars) and fitted Gaussians (red and blue curves) of the PCA-LDA score distribution of the training sets for the HAC vs. HOA (Human, left), RAC vs. RIF (Rat, middle), and CL2 vs. CL1 (Collagen, right) metrics. (**b**) Low signal-to-noise Raman spectral maps taken from HAC (top) and HOA (bottom) samples, and scored by human (left), rat (middle), and collagen (right) metrics. (**c**) Distributions of PCA-LDA scores from the maps in **b**, as scored by human (left), rat (middle), and collagen (right) metrics. The histograms and dark Gaussians curves represent the combined distributions for the HAC maps (red) and HOA maps (blue). The light curves represent the distributions of individual HAC maps (red) and HOA maps (blue). Differential scoring of HOA maps 3 and 6 are highlighted by dotted and dashed lines respectively.

To connect the derived scoring metrics back to spectral information, and thus to the physical meaning of the scores, we extracted combined PCA-LDA coefficients. These are calculated by multiplying the PC coefficients, which transform spectral data into a PCA score for each PC, by the coefficients that define the LDA axis in PC space, and then summing them for each wavenumber. In mathematical terms it is the dot-product of the PCA coefficients with the LDA coefficients. The result is a spectrum with the same number of wavenumbers as the original spectrum, which describes the relative influence of each wavenumber variable on the score of a spectrum on that particular PCA-LDA metric. The PCA-LDA score is equal to the dot-product of this PCA-LDA coefficient with the original spectral data, plus a constant. Positive scores and PCA-LDA coefficients were chosen to be associated with the cartilage or cartilage-like member of the training set pair .

A comparison of the PCA-LDA coefficients for the RAC vs. RIF, HAC vs. HOA, and CL2 vs. CL1 metrics, presented in Figure 2.4b, reveals a number of similarities and differences. Prominent features common to each of these coefficient spectra correspond to wavenumbers of specific observed Raman bands for the phenylalanine ring breathing mode at 1004 cm^{-1}, and C-C protein backbone modes at 940 cm^{-1} and 1130 cm^{-1}. Moreover, the overall shapes for all three coefficient spectra appear to follow similar trends in certain regions. The coefficient remains generally positive from approximately 1000 cm^{-1} to 1150 cm^{-1} and from 1350 cm^{-1} to 1450 cm^{-1}, while they are largely negative between 1200 cm^{-1} and 1300 cm^{-1}. This negative region corresponds roughly to the range of the amide III band complex.

However, a close comparison of the coefficient spectra reveals that, even in the regions where broad features seem to be consistent for the coefficient spectra, the sharper local features often fail to line up with one another. Most notably, the HAC vs. HOA coefficients are characterized by a prominent peak corresponding to the C-C protein backbone band at 817 cm^{-1}, which is not observed in either RAC vs. RIF or CL2 vs. CL1 coefficients. Conversely, only the RAC vs. RIF and CL2 vs. CL1 coefficients indicate the presence of a peak for the C-H deformation at 1460 cm^{-1}. In the region representing the amide I band complex, between 1600 cm^{-1} and 1700 cm^{-1}, the three coefficient spectra show little agreement in coefficient values at wavenumbers corresponding to specific spectral features. The Pearson correlation values were calculated to be 0.318 between the human and rat metric coefficients, 0.424 between the rat and collagen coefficients, and 0.182 between the human and collagen coefficients. These observations suggest that, while not completely uncorrelated, the metrics produced by the different training materials are based on substantially dissimilar features in the training spectra. Metrics based on overly similar spectroscopic features would not make good candidates for combination.

Chapter 2.3.4. Low-acquisition-time spectral maps

We constructed spectral maps from low SNR spectra taken from equally spaced points to test the classification of our metrics. Spectral maps serve as a means for visualizing the spatial distribution and local variation of PCA-LDA scores. Mapping the injury site region in the rat injury model sample, shown in Figure 2.2b provided a convenient way of validating our PCA-LDA method in the rat metric. In

this map we observe the accurate reproduction of the tissue features, with the red and pink region of the injury site clearly distinguished from the blue of the surrounding articular cartilage. The effectiveness of the PCA-LDA is further supported by applying the collagen metric scoring to this same injury site map (Figure 2.2c). This CL2 vs. CL1 map closely mirrors the features of the RAC vs. RIF map with spectra from the uninjured cartilage scoring as very similar to collagen type II and the fibrocartilage in the injury site scoring as more similar to collagen type I. This is in agreement with the histological staining for collagen type II and type I, as well as the established matrix characteristics of tissue formed after microfracture surgery[149,150].

The accuracy of the three metrics was tested by the unguided classification of quickly-obtained, low signal-to-noise ratio (SNR) spectra from healthy and osteoarthritic cartilage. Low SNR spectra were used because short acquisition times go hand-in-hand with the non-invasive appeal of a potential Raman diagnostic method, and so clinically derived spectra might be expected to exhibit relatively low SNR. We acquired six low SNR spectral maps each from the normal human articular cartilage and human osteoarthritic cartilage samples, and performed an unguided classification of the maps by scoring them with each of the three metrics. These maps provide the large number of spectra required for statistical confidence, as well as the ability to observe local variation within the mapped region and variation across the sample. The resulting spectral images in Figure 2.5b, show that for all of the metrics, spectra of healthy cartilage sample score distinctly different values

from osteoarthritic sample. This is also represented in Figure 2.5c as a distribution of scores. Here, it can be more clearly observed that the human and rat metrics each produce scores well fitted by normal distributions. The variation in scores between maps (different sample regions) is greater than within-map variation, particularly for the OA maps. A purely unguided classification – the classification boundary fixed at zero on the PCA-LDA metric – results in only the human metric producing a reasonably small misclassification rate of 5.3%. To assess only efficacy at separating one class of spectrum from the other, the metrics were calibrated by shifting the boundary to maximize this separation. The small overlapping tails in the fitted Gaussians then represent the probability of misclassification. In this case, misclassified spectra make up 4.1% of the 7656 total spectra from the 6 healthy cartilage and 6 osteoarthritic maps when scored with the human metric, and 2.7% of the total when scored with the rat metric. Meanwhile, despite the exceedingly good classification of its training sets, the collagen metric did not perform as well as a diagnostic for osteoarthritic cartilage, misclassifying 14.7% of the map spectra.

The heterogeneity of the average rat and human metric scores of the maps in Figure 2.5b, in particular the osteoarthritic maps, warranted further examination. Given the arbitrary location of the maps within the middle zone we speculated that the scores might vary according to location relative to the articular surface. We pursued this hypothesis by acquiring spectral maps covering a large portion of the depth of the samples from the articular surface through the middle zone (Figure 2.6). The human and collagen metrics score both healthy cartilage and osteoarthritic

maps consistently throughout the depth examined, approximately 550 μm. In contrast, the rat metric produces a gradient of scoring in the osteoarthritic map - more fibrocartilage-like near the articular surface and more cartilage-like deeper into the tissue. A similar, though significantly less pronounced pattern is also observed in the rat metric scoring of the healthy cartilage map. These results indicate that the rat metric scores are a function of the zonal cartilage depth, while the variation of the scores from the human and collagen metrics appear to be largely spatially independent.

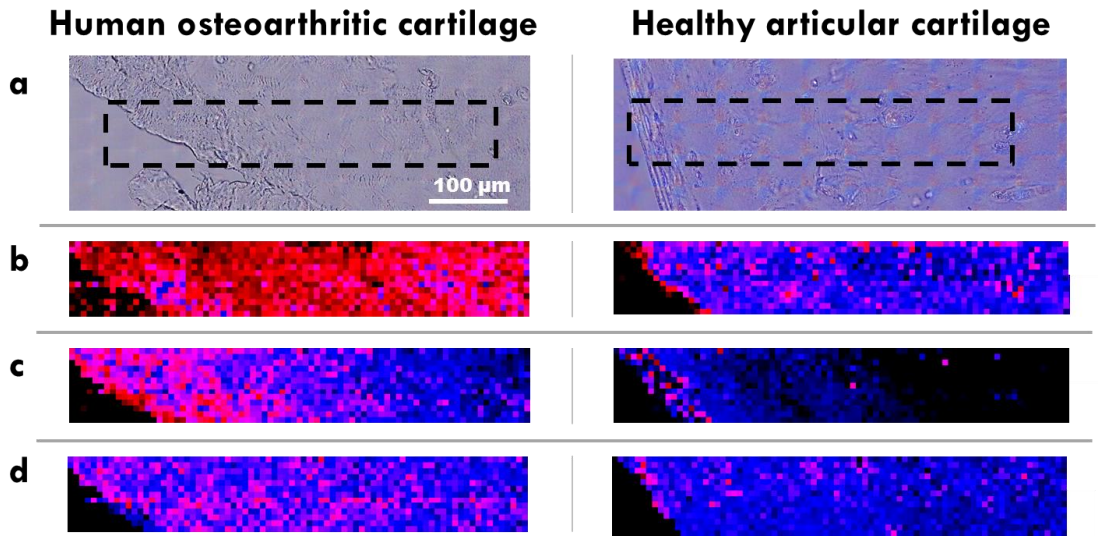

Figure 2.6: Depth-profile spectral maps of human osteoarthritic cartilage (left) and human articular cartilage (right). (**a**) Bright-field image indicating the region from which the maps were obtained (dashed line). Spectral maps were scored by the human metric in (**b**) the rat metric in (**c**) and the collagen metric in (**d**)

Chapter 2.3.5. Combination of PCA-LDA metrics

To test our hypothesis that multiple PCA-LDA metrics, applied in concert could classify noisy cartilage and OA spectra better than a single metric, we calculated the linear combination of the metric coefficients that best reduced the

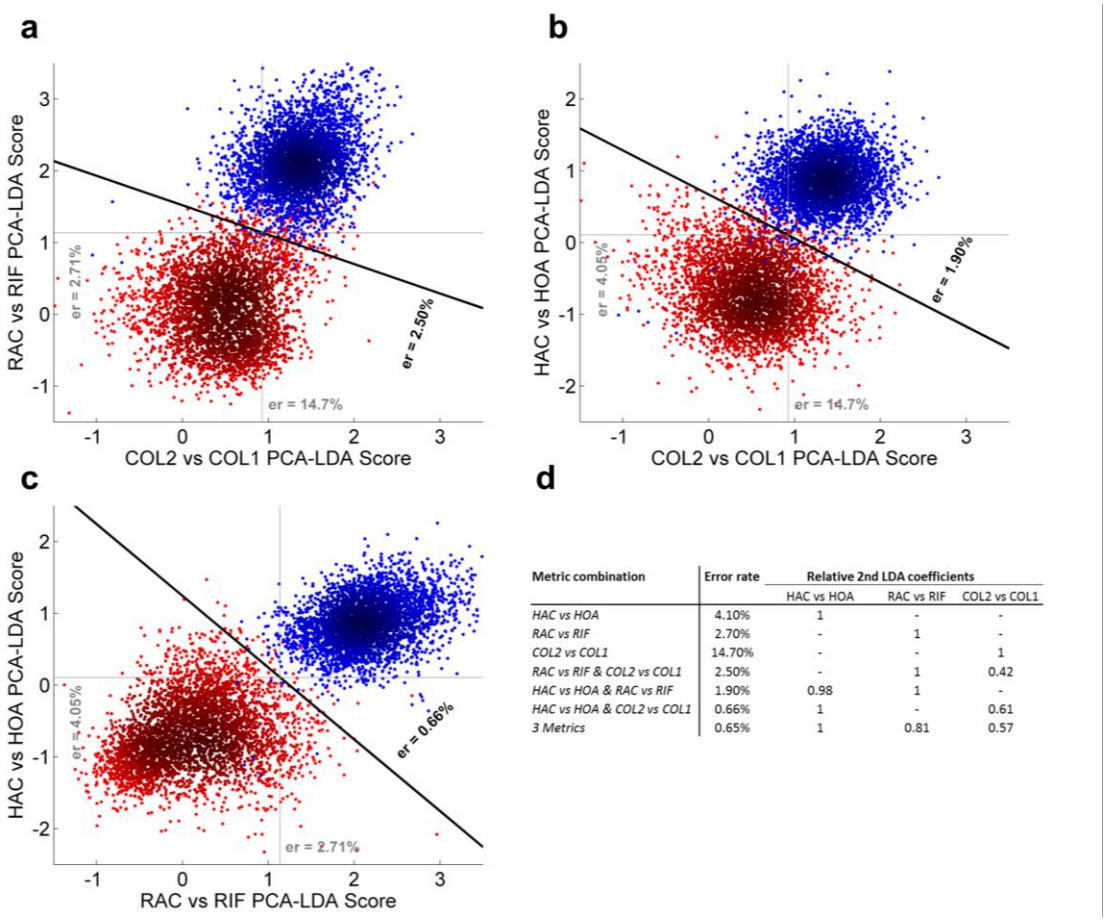

Metric combination	Error rate	Relative 2nd LDA coefficients		
		HAC vs HOA	RAC vs RIF	COL2 vs COL1
HAC vs HOA	4.10%	1	-	-
RAC vs RIF	2.70%	-	1	-
COL2 vs COL1	14.70%	-	-	1
RAC vs RIF & COL2 vs COL1	2.50%	-	1	0.42
HAC vs HOA & RAC vs RIF	1.90%	0.98	1	-
HAC vs HOA & COL2 vs COL1	0.66%	1	-	0.61
3 Metrics	0.65%	1	0.81	0.57

Figure 2.7: Scatter plots of the human metric score versus collagen metric score (**a**), human metric score versus rat metric score (**b**), and rat metric score versus collagen metric score (**c**) of each spectrum from the HAC (blue) and HOA (red) low signal-to-noise maps. Light vertical and horizontal lines represent present the single metric PCA-LDA classification boundary. Dark diagonal lines represent the classification of boundary resulting from the combination of two metrics through a second LDA (er = error rate). (**d**) Table summarizing the classification of low signal-to-noise map spectra.

misclassification rate for the low SNR healthy and osteoarthritic cartilage map spectra. This was done by performing a second LDA, using combinations of the three different metric scores from the maps as input variables. The scores of one metric are plotted against those of another in Figure 2.7a. The diagonal line that best separates the two classes of spectra represents the optimal combination of metrics as calculated by the LDA. The misclassification rates calculated by employing this method of combining metrics are given in Figure 2.7b. Reduced misclassification was achieved for all metric combinations. Although the greatest reduction was obtained by combining all three metrics this value was statistically the same as the 0.66% error rate observed for the combination based on the human and rat metrics. Other metric combinations also lead to a decrease in misclassification rate as shown in the Table in Figure 2.7d. Taken together, these results indicate that combining PCA-LDA scoring metrics through a second LDA will generally improve classification, but that the extent of the advantage will be determined by the specific metrics used.

Chapter 2.4. Discussion

To examine the potential of Raman spectroscopy as a cartilage evaluation tool, we have demonstrated an effective method for distinguishing Raman spectra from samples of normal and diseased human cartilage. This method is based on the use of different materials that model cartilage disease to create spectroscopic metrics on which a test spectrum is scored as being normal or pathological. Because each metric performs its diagnostic classification based on different spectroscopic

characteristics gleaned from the model it was derived from, combining them can prevent misclassifications made by individual metrics. We have found that some of these combinations eliminate nearly all misclassification of noisy, low-acquisition-time normal and OA spectra. The three metrics we have developed were derived from spectra taken from pairs of training materials representing diverse approaches for modeling cartilage disease. We selected purified protein training materials as the simplest way of representing the molecular differences between healthy and diseased cartilage. Collagen type II is the primary proteinaceous component of hyaline cartilage, and a reduction or disruption of this component is often associated with cartilage disease. While collagen type I is not highly expressed in OA cartilage, it was chosen to contrast collagen type II in this metric because it is spectroscopically similar enough to collagen type II (unlike purified GAGs) not to skew classification of tissue spectra dominated by collagen features. Use of the rat microfracture injury model was undertaken to derive a metric based on training samples with exaggerated structural differences analogous to those that eventually result in the loss of function in diseased cartilage. Fibrocartilage formed after a full-thickness penetration cartilage wound is an entirely remodeled tissue that offers only partial functionality and durability. Finally, the derivation of the HAC vs. HOA metric from the same samples upon which we ultimately tested the low SNR classification of all the metrics was intended to provide a positive control – *i.e.* the metric that should provide the best classification. Each of these metrics was found to

be useful, to a greater or lesser extent, for distinguishing the low SNR spectra of normal and OA cartilage from one another.

While the classification performance of the collagen metric was, as expected from its simplicity, the least effective of the three, the similarity of classification rate between the rat and human metrics was surprising. The two fibril forming collagen isoforms we examined are ostensibly very similar materials. However, the PCA-LDA produces the best training set separation for the collagen sets out of all the metrics, highlighting the sensitivity of the analysis while indicating that significant differences do exist between the spectra of the two proteins. This separation of the training sets does not translate to the accurate classification of human cartilage and osteoarthritic cartilage. This may result from the relative simplicity of the purified training material, or may reflect the weak connection between the collagen type I training spectra and osteoarthritic cartilage tissue. While only the human metric accurately classifies human map spectra as-derived, the human and rat metrics are similarly accurate when a shift of the classification boundary is made. Given the rat metric's basis on samples from a different species, with unrelated degradative mechanisms, it is surprising that detailed molecular changes characterized by that metric are so accurate at identifying OA in human cartilage. Even lacking a full understanding this result is very encouraging for the use of model material sets for Raman diagnosis.

The improved classification that is achieved through the combination of metrics appears to relate to the similarity of the metrics combined. By combining

metrics through an LDA, some metric dissimilarity is implied by any observed classification improvement, since a linear combination of very similar metrics could only create equally similar classification. The correlations calculated between PCA-LDA coefficients quantify the degree of similarity between the spectroscopic basis of each metric. The rat and human metrics, whose combination produces the greatest reduction in misclassification, have an intermediate correlation between their coefficients (0.318). The most highly correlated metric coefficients, the rat and collagen (0.424), have a comparatively low combinatorial effect. The resulting similarity in classification can be observed as the diagonal spread of the corresponding rat-metric-versus-collagen-metric scatter plot in Figure 2.6c. It seems likely that these two metrics were too similar in molecular basis for their combination to result in a significant advantage. This similarity also suggests that the rat metric is strongly influenced by the differing collagen content of the cartilage and fibrocartilage training materials, but also by some additional complex tissue-specific features that account for the more accurate classification of the human samples. In the third case, a relatively high misclassification rate is achieved by combining the collagen and human metrics, though the metric coefficients are the least correlated (0.182). However, the reduction in misclassification from the human metric alone (4.1% to 1.9%) is much greater than the reduction observed between the rat metric and the combination of the rat and collagen metrics (2.7% to 2.5%). To achieve a low misclassification rate through metric combination, future

efforts should look to find metrics that have dissimilar spectroscopic bases while each providing independent classification that is as high as possible.

We have analyzed the metric coefficients to better understand the additional molecular changes that the rat and human metrics exploit to achieve more accurate OA classification than the collagen metric. While the nature of the multivariate analysis – simultaneous consideration of all spectral changes - precludes attributing classification to one, or even a few specific Raman bands, examination of the PCA-LDA metric coefficients provides insight into the molecular differences that are described by a metric. It seems likely that the similarity noted in the general shape of the coefficients relates mostly to the change in collagen as it is present in all three metrics and least consistently observed in the human metric. Conversely, areas of agreement between the rat and human coefficients that differ considerably from the collagen coefficient could give clues to possible common non-collagenous molecular changes exploited for classification. For instance, several features in the amide III region between 1225 cm^{-1} and 1300 cm^{-1}, including the polar and non-polar peak positions[147] at 1270 cm^{-1} and 1245 cm^{-1}, match well between the rat and human coefficients, but poorly with the collagen coefficient. The amide III mode is particularly sensitive to side chain effects[151]so this could indicate a shared response to differences in non-collagenous proteins in the rat and human metrics. Nevertheless, these exclusively shared features are a small minority of the spectral bandwidth and the lack of feature alignment in the majority of the coefficients suggests once again a largely unrelated molecular underpinning for the rat and

human metrics. Particularly notable is the lack of shared features in the amide I band. This band is sensitive to protein secondary structure[151], suggesting that conformational changes between the training set pairs may be an important difference in the three metrics

The rat and human coefficients are conspicuously missing features that would indicate the strong influence of GAGs on the classification mechanism. Change in the GAG content of cartilage is a well-established characteristic of OA, particularly in later stages[152]. The most prominent peak in a spectrum of chondroitin sulfate (CS), the primary GAG in cartilage, is located near 1062 cm^{-1}. In several multivariate Raman studies of cartilage this feature has been successfully utilized in the analyses to represent the presence of GAGs in the matrix[44,46,142,153]. Indeed, we observe this peak in the coefficients of some of the lower order PCs from both the rat and human metrics (Figure 2.8), but not in the coefficients representing the full PCA-LDA. One reason that GAGs are not represented in the PCA-LDA coefficients is possibly a lower Raman scattering cross-section for that material. The CS peak at 1062 cm^{-1} is a relatively weak one in the average spectra. Because the PCA-LDA is guided only by spectra of the training materials, it will produce metrics that are sensitive to the differential spectral changes and not to molecular changes. It is also possible that changes in GAG content are accounted for in the metrics through more subtle spectral features that are difficult to interpret directly from the coefficients. The human cartilage and OA depth-profile maps in Figure 2.6 support this possibility. The gradient in the scores shown in the RAC vs. RIF scoring of these maps,

correspond to the gradient in GAG concentration observed to exist between the superficial and middle zones in articular cartilage[152]. Sensitivity to changes in GAGs could explain the better-than-expected classification of the rat metric relative to the human metric, which produces no depth-profile scoring gradient. Such sensitivity could arise from the exaggerated loss of GAGs observed in the rat cartilage injury repair, relative to OA degradation. Importantly, a depth-profile gradient is not a product of collagen metric scoring, which would preclude connecting such gradients to proteoglycans.

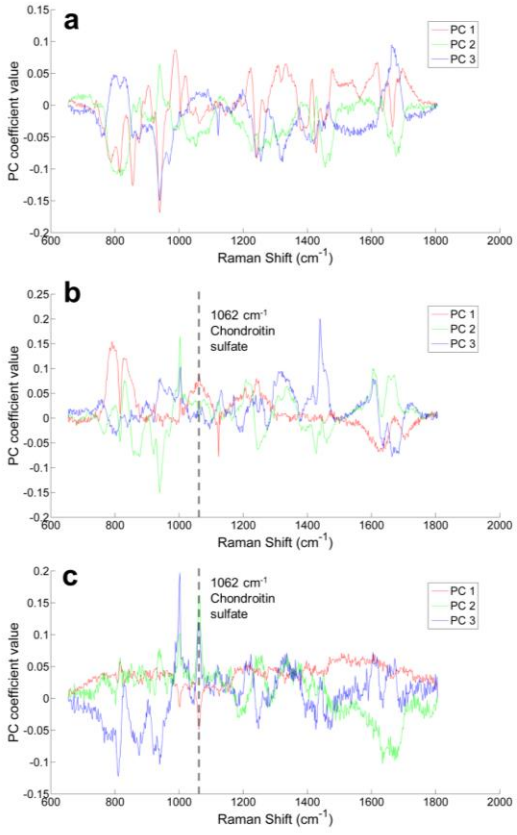

Figure 2.8: Coefficient spectra for the first 3 PCs from the PCA-LDA analysis which derived the (**a**) collagen metric, (**b**) the rat metric, and (**c**) the human metric.

Ultimately, further development of this method of diagnosis will require the implementation of large training sets that can overcome disease variation among individuals as well as variation throughout the progression of disease. Accumulating these training sets will likely require a concerted clinical effort, as animal samples will always be sub-optimal and a large cohort of patients is desirable. The results presented here offer a proof of concept that can be leveraged in such a larger scale effort. First, our work suggests a significant advantage in using multiple metrics to increase confidence in a diagnosis. The successful metrics described here can also guide the choice of the source materials for the clinical training sets. The performance of the rat model used here points towards the potential of spectra taken from patients following micro-fracture surgery as a source of training data. This could be accomplished through the use of a fiber-optic probe that could obtain spectra with minimal intrusion during arthroscopic follow ups that are routine after this procedure. Similarly, a training set based directly on OA cartilage could be obtained during arthroscopic exams on tissue clearly indicating the onset of the disease. Preferably, another OA training set would be composed of spectra taken from pre-clinical OA cartilage. The difficult task of obtaining a large training set of this type would likely require the fiber-optic acquisition of spectra during routine arthroscopic joint examinations on patients that could subsequently be followed for the development OA. While this is a long term proposition, these preliminary results give confidence that multivariate Raman classification has the intrinsic sensitivity to

make that investment worthwhile. Finally, while the collagen metric provided relatively poor OA classification, it did demonstrate the rudimentary ability of a metric based on purified single macromolecules to provide classification in tissues in which those molecules are differentially expressed. Through a careful selection of proteins or combinations of molecules that better approximate healthy and diseased cartilage, an improved non-clinical metric could be potentially derived.

Chapter 2.5. Conclusions

We have found that multivariate analysis can be applied to pairs of Raman spectral sets from diverse model materials to produce classification metrics. These metrics have been demonstrated to correctly classify OA and normal cartilage in low SNR spectra. We have additionally concluded that the combination of a number of metrics similar to the ones reported here might form the basis of a sensitive clinical diagnostic. Current study employed specimens from patients with relatively progressed stages of OA to obtain distinct Raman data sets for initial validation.

From the clinical prospective, the most valuable application of Raman spectroscopy is expected in patients with pre-clinical and pre-pathomorphological stages of OA not detectable with MRI or other currently used techniques. Many additional steps remain before clinical Raman diagnosis in cartilage can be realized, including further technical development of *in vivo* fiber-optic spectral acquisition. Yet, our results reflect what now appears to be clear - the inherent sensitivity of the Raman spectroscopy to the molecular variations that characterize cartilage disease is more than adequate. In fact, our analysis suggests that many future problems

might be solved after spectral acquisition is complete, through the development of new methods of decoding of the enormous information stored in a Raman spectrum.

Outside of the clinic, the techniques demonstrated in this chapter may prove very useful in our efforts to develop tissue engineered cartilage. The ability to measure a sample's spectroscopic similarity to functional cartilage matrix using a number defect models might be especially useful in experimental constructs where potential miscues in development will be unknown.

Chapter 3. Automated Confocal Image Analysis of Confined hPSC Colonies

Chapter 3.1. Introduction

There is enormous heterogeneity in cell composition and genetic and epigenetic gene expression during hPSC differentiation, which is a key bottleneck to translation to therapeutic treatments. The propensity of human pluripotent stem cells (hPSC) to grow as colonies introduces a spatial element to the numerous cues that regulate pluripotency and differentiation. An individual cell's local environment, with respect to both physical and chemical signals, may vary with that cell's location within a colony, as well as changes in the pluripotent character of the colony as a whole. While heterogeneity within the pluripotent state has been observed to vary with respect to a cell's location within a colony[54], further investigation of these effects spatial has been limited. The limitations may be traced to the tools being employed. To examine the pluripotent state on a single cell level using molecular assays or flow cytometry, cells must be removed from colonies, precluding detailed consideration of the position or condition of the cell within the colony[59,60]. Alternatively, imaging of immunohistochemically stained colonies allows for the examination of single cells in their native state, but is most often utilized to provide support for quantified measures in the form of examples. Recent research has shown that computer driven analysis can be employed to produce automated reconstructions of structures within cultured tissues using confocal image stacks[154,155]. Utilizing this approach, the inherent advantages of imaging in the area

of hPSCs can be extended by obtaining a large number of experimentally consistent colonies to include enough cells for statistical confidence. In conventional cultures, hPSCs grow as colonies of heterogeneous size and shape, which limits one's ability to make direct comparisons or to aggregate spatially specific data among many colonies. Quantified image analysis from regular colonies could thus fill an important gap in understanding hPSC spatial heterogeneity.

Meanwhile, in anticipation of the stringent requirements of the clinical translation, the concept of producing patterned colonies of hPSCs has been investigated by several groups as means of increasing the reproducibility and scalability of hPSC culture[62–67,156]. HPSC patterning has been achieved by various methods including physical confinement in microwells and confinement through chemical surface modification by optical and soft lithographic techniques. We have shown that culturing hPSCs on substrates patterned by micro-contact printing (μCP)[157] can produce uniform circular colonies of a predefined size that maintain pluripotency over a number of passages under defined conditions[68]. This method of uniform culture appears quite promising for the large scale production of hPSCs. Despite this promise, relatively little has been studied about the detailed effects of colony patterning on pluripotency and differentiation. Bauwens et. al. showed that the size of a μCP patterned hPSC colony could affect lineage fate, but did not address how that fate varied by location within the colony nor the effects of confined growth through altered colony morphology[65].

We have developed a method to study the *in situ* spatial variation of hPSC within uniform colonies laterally confined to chemically defined regions. We have demonstrated this method by examining altered pluripotency and differentiation markers, as well as cellular and colony morphological changes in these patterned cultures. Uniform size and shape makes it possible to measure collective spatial variation in many equivalent colonies. In addition, their symmetry permits this spatial variation to be projected to a single radial dimension. We have exploited these advantages by combining the μCP culture platform with confocal microscopy and automated image analysis as a means of spatially tracking single cell hPSC transcription factor expression by immunofluorescence (IF). In our image analysis software, individual cell nuclei are identified and demarcated in confocal image z-stacks of fixed colonies via DAPI staining. These 3-dimensional reconstructions reveal information about cell and colony geometry. Expression of nuclear antigens can then be measured from the other IF channels and summed in these distinct nuclear regions. The single-cell expression of these antigens, including transcription factors, can then be evaluated as a spatial distribution in the radial and vertical dimensions of the colonies, and as a function of characteristics of the colonies of which they are members. We have demonstrated this system by tracking expression of the pluripotency-associated transcription factor OCT-4 as well as three early transcriptional differentiation markers, though it could be employed more widely to examine any antigen localized to the nucleus. We make the general observation that, as hPSC colonies become thicker in confined patterns, the expression of OCT-4 is

diminished. Furthermore, this occurs first towards the center of thinner colonies and spreads outward in thicker colonies. The loss of OCT-4 is mirrored by a loss of baseline expression of some early differentiation markers. Nuclei showing high levels of these differentiation markers increased in number in colonies of different thickness depending on the marker.

Chapter 3.2. Experimental Methods

Chapter 3.2.1. Materials

16-mercaptohexadecanoic acid, triethylene glycol mono-11-mercaptoundecyl ether, and anhydrous ethanol were purchased from Sigma Aldrich. #1.5 circular coverglass was purchased from Ted Pella. All reagents and solvents unless otherwise stated were used without further purification.

Chapter 3.2.2. Surface Patterning by μCP.

The process of preparing μCP-patterned cultures of hESCs has been described previously[67]. Briefly, a polydimethylsiloxane (PDMS) stamp coated with a carboxylic acid-functional thiol was pressed into conformal contact with a gold coated coverglass substrate. This reproduced the pattern of 200 μm circles present on the stamp as regions of protein-binding carboxylic acid-functional self-assembled monolayers (SAMs) on the substrate. These regions were then surrounded by a protein-resistant oligo(ethylene glycol)-functional SAM by immersing the substrate in an ethanolic solution of a thiol of that functionality. Unpatterned control

substrates were made by immersing a clean gold-coated substrate in a solution of the carboxylic acid-functional thiol. In order to be able to perform confocal microscopy after culture the substrates were then mounted with epoxy glue to the bottom of a 3 cm dish in which a hole had been hot-punched. These custom glass bottom dishes were then incubated with a 1:400 dilution of Matrigel in PBS overnight prior to cell seeding.

Chapter 3.2.3. HESC Culture

Human embryonic stem cells (hESCs) lines, H9 (WiCell) cultured in hESC medium consisting of Dulbecco's Modified Eagle Medium-F12 (Invitrogen) supplemented with 20% Knockout Serum Replacement (Invitrogen), 1 mM L-Glutamine, 2 mM 2-Mercaptoethanol, 1mM Non-essential Amino Acids, and 4 ng/ml basic Fibroblast Growth Factor (bFGF, Invitrogen). Prior to seeding on Matrigel-coated SAMs cells were cultured on gelatin coated plates with mitomycin C-treated mouse embryonic fibroblasts (MEFs) derived from embryonic day 13.5 embryos from CF1 mice. To generate conditioned medium (CM), MEFs were cultured with hESC medium for 24 hours. Culture on μCP SAM substrates first involved dissociating hPSCs to single cells using 0.05% trypsin-EDTA (Invitrogen) and filtering with a 40 μm nylon mesh strainer (BD Falcon) to remove feeders and aggregates. After the addition of trypsin inhibitor (Invitrogen), hESCs were centrifuged at 1,000 rpm and resuspended in either CM with 10 μM HA-1077 dihydrochloride (Sigma). The Matrigel solution was then aspirated from the

patterned SAM s and each dish rinsed three times with PBS. A dilution of 50,000 hESCs in 4 mL was then seeded into each μCP SAM dish. Cells were allowed to attach undisturbed for 1 day and then fed by removing only half of the medium and replacing it with fresh medium.

Chapter 3.2.4. Immunofluorescence Staining

After 4 days in cultures the patterned hESCs were rinsed in PBS then fixed with 4% paraformaldehyde for 30 minutes. After rinsing again with PBS each well was treated with 0.1% Triton X-100 in PBS. Another PBS rinse was next followed by the addition of a blocking solution of 10% goat serum for 1 hour at room temperature. Each well was then incubated with the manufacture's recommended concentration of primary monoclonal antibodies (OCT-4, mouse, Santa Cruz; PAX6, rabbit, Covance; Brachyury, rabbit, Santa Cruz; GATA6, mouse, R&D) overnight at 4°C. Wells were rinsed with PBS, then incubated with the secondary antibodies (anti-mouse IgG, FITC; anti-rabbit IgG, Rhodamine) for 2 hours before more PBS rinsing. Each well was the treated with 1 drop of VECTASHIELD Mounting Medium with DAPI (Vector Labs) in PBS before imaging.

Chapter 3.2.5. Confocal Microscopy

Confocal image z-stacks were acquired on a Zeiss LSM 700 laser scanning inverted confocal microscope through a plan-apochromat x63/1.4NA oil immersion objective. All patterned cultures were prepared on #1.5 coverglass matched to this

objective. Optical sections at 1 μm intervals were obtained using a pinhole of 70 μm. Scan speed was set to a dwell time of 5.8 micro-seconds per pixel per channel. Electronic gain of the photomultiplier tube was set for each channel to leave minimal number of saturated pixels in a representative image and maintained for all z-stacks with the same staining. Each IF channel was measured in a separate scan to limit cross talk.

Chapter 3.2.6. Image Analysis

Images were processed by importing RGB TIFF files into a custom made Matlab (Mathworks) routine. First, nuclear regions within each optical section of an image stack were delineated as a binary image by applying an adaptive threshold subroutine to the DAPI (blue) channel image, then employing a series of dilation, erosion and median filter operations. As nuclei appeared to intersect in some images, a watershed algorithm was then used to distinguish individual nuclei. By adapting a routine intended for tracking particles in a time-lapse image series, the nuclear domains of all of the optical sections in a stack were assembled into reconstructed 3D nuclei. The nuclear domains were then used as a mask to sum the fluorescence intensity from the other two image channels in each nuclear space independently. In this way a list was compiled for each image stack containing location, geometric and fluorescence data for individual nuclei. The data from multiple colonies were then combined so that interrelation of these properties could be queried on a colony or single cell basis. The colony height was chosen to be

defined as the optical section number at which the number of nuclei drops below 10% of the highest number of nuclei in any single section in the stack. All nuclei identified were included in the analysis, even those above the defined height of the colony.

Chapter 3.3. Results

Chapter 3.3.1. Studying hPSCs with automated image analysis of patterned colonies

We have developed a new method to produce dependable information on spatial variation and the effects of confinement in hPSC colonies. As Figure 3.1 illustrates this method is accomplished by the combination of four distinct processes. First, micro-contact printing is employed to create a chemical pattern on a culture substrate that limits the growth of colonies to defined regions. In the work presented here 200 μm circles are used as the pattern, but the size and geometry of the regions can be easily tailored. Second, hPSCs are seeded onto the patterned surfaces and cultured under standard conditions to form arrays of regular colonies. In previous studies we have achieved uniform patterned colonies by seeding at a high density – ensuring all patterned regions are blanketed with cells[67]. In these experiments, however, we have reduced the seeding density to purposely produce patterned regions with varied initial cell density. This has allowed us to fix colonies at varying stages of confined growth in a single time point. In the third part the IF signal distribution of patterned cultures is captured in 3-D in confocal image z-

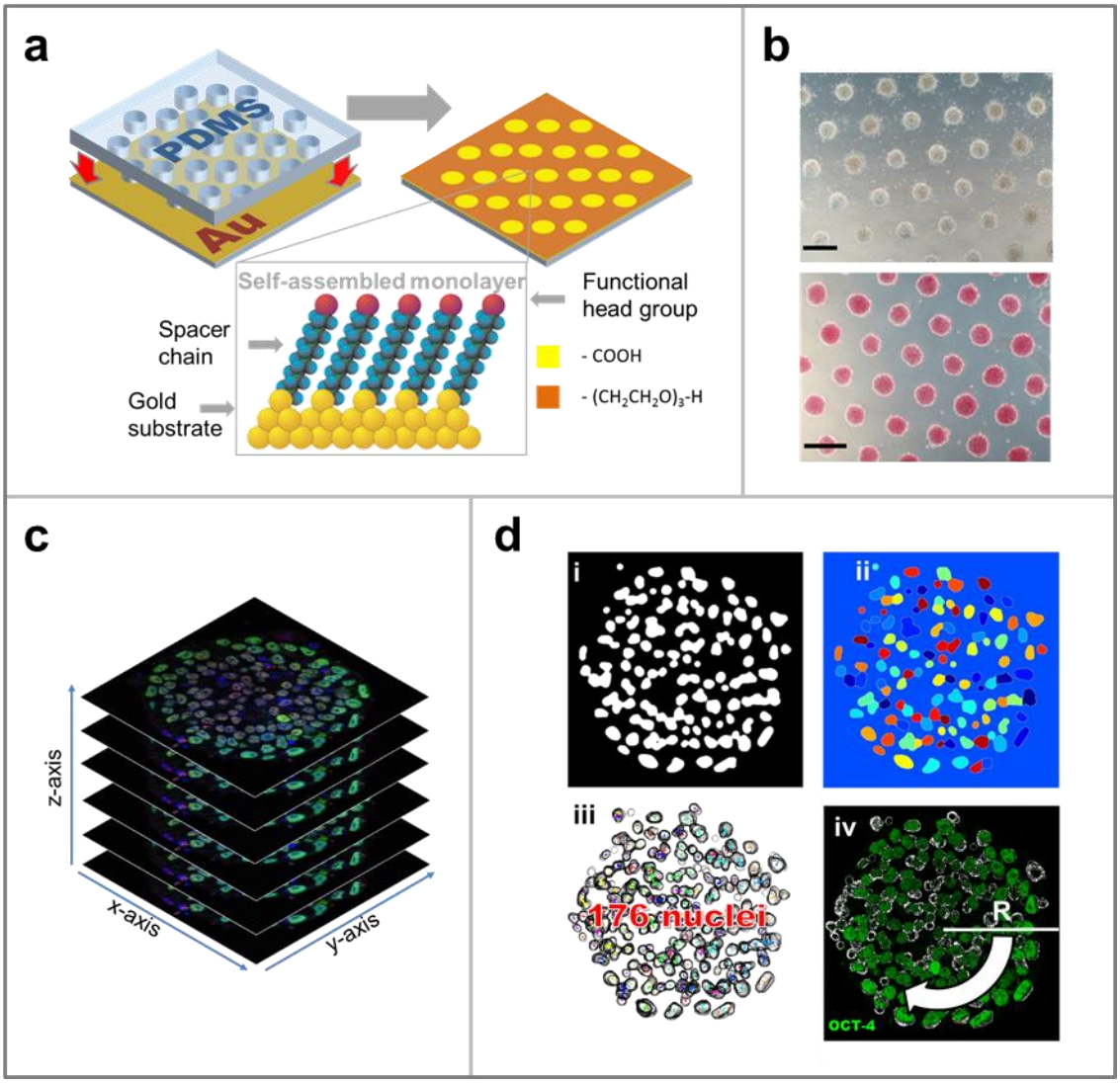

Figure 3.1: (**a**) Micro-contact printing (μCP) produces patterns of uniform circles by modifying the surface chemistry of the substrate. (**b**) hPSC colonies, seeded as single cells with ROCK inhibitor, grow to fill only the 200 patterned regions (top) and remain pluripotent as shown by AP (bottom). (**c**) Confocal imaging measures immunofluorescence (IF) signal in 3-D as a series of stacked 2-D images. (**d**) The collected images of many colonies are input into custom software to analyze spatial variation in IF intensity. The DAPI channel is used to identify the nuclear regions (i). Individual nuclei are then segmented by a watershed algorithm (ii). Isolated nuclei are then tracked through the stack based on proximity to give an accurate cell count (iii). The localized IF intensity in each of these nuclear regions is summed to give single cell fluorescence values (iv).

stacks. In the final component of the process, the image analysis we have developed allows for the automated characterization of many properties of single cells within these colonies. Image stacks from many colonies are manipulated and analyzed in the custom software. By utilizing only the DAPI fluorescence channel in the confocal image z-stacks, this software closely approximates the 3-D shape and location of individual nuclei within a colony. These reconstructed nuclei permit us to assign additional IF signal to individual cells and generate characteristics of whole colonies.

Chapter 3.3.2. Cell and colony morphology of patterned hESCs

The laterally confined growth of hESC colonies in chemically-defined patterns results in changes to both cell and colony morphology as the cells proliferate within a limited colony footprint area. We have characterized these morphological effects by reconstructing the cell nuclei within colonies in 3-D through the automated analysis of confocal image z-stacks. A hallmark of the variation achieved by sparse seeding was a darkening of some colonies in bright field microscopy that we could observe prior to analysis (Figure 3.1b). This suggested either an increase in vertical colony thickness, or an increase in cell density. Changes to hESC colony morphology that result from patterned culture could be understood based on collective nuclei locations. By measuring the distance between the substrate and the highest optical slice in which nuclei are observed we have demonstrated that that hESCs can increase a colony's thickness by close to a factor of five as they proliferate in a confined region. The thinnest patterned

colonies were found to have a height of approximately 5-10 μm, similar to unpatterned controls, while the thickest patterned colonies grow to more than 40 μm (Figure 3.2a).

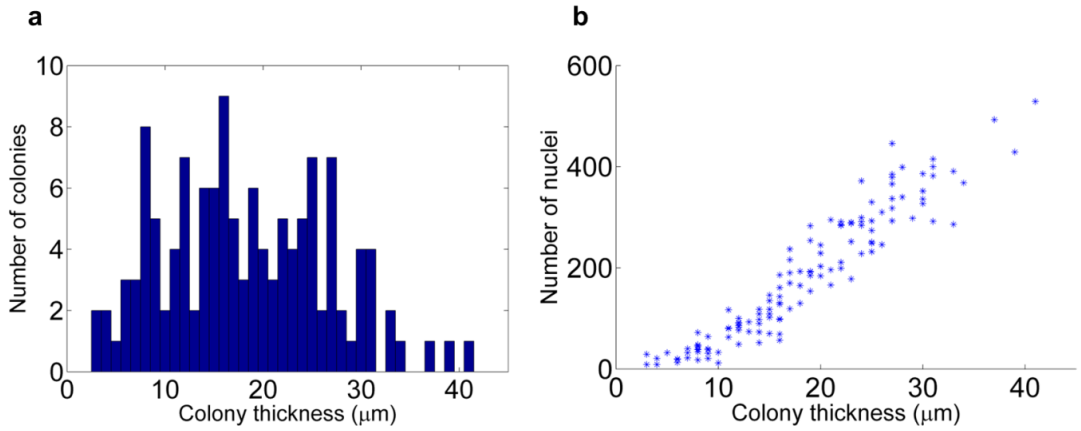

Figure 3.2: (**a**) Histogram of the thickness of all patterned colonies that were analyzed. (**b**) Scatter plot tracking the correlation between the number of nuclei that were counted within a colony and that colonies thickness.

Reconstructing the nuclei within colonies also permits accurate cell counts, which confirm the connection between colony thickness and proliferation (Figure 3.2b). Automated counts were verified in several colonies of varying thickness by hand counting and found to be within 5% in all cases. Thin colonies have many fewer cells, around 30 in a 200 μm diameter pattern, compared to thick colonies, which contain as many as 500 cells. While it is expected that a thicker colony would contain more cells, we were also interested in effects of confinement on the volumetric density of the cells in these colonies. By approximating the volume of each colony as its footprint area summed over its thickness we converted the cell counts produced by our image analysis to a measure of cells per unit volume, or it's

inverse, average cell volume. We found there was a clear trend indicating an increase in cell density in thicker colonies (Figure 3.3c).

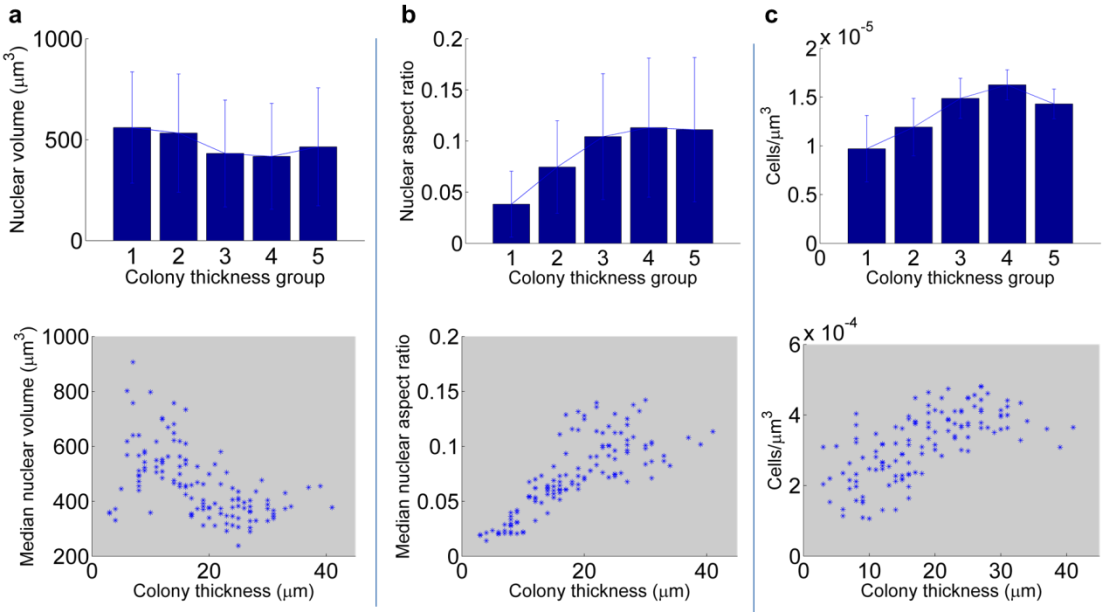

Figure 3.3: The colony thickness related variation of (**a**) nuclear volume, (**b**) nuclear aspect ratio, and (**c**) volumetric cell density, averaged for each colony thickness group (top) and for each colony (bottom).

Additionally, we could observe that the nuclear cross-sections from the optical slices of thin colonies were considerably larger than those of thick colonies. We measured the volume and aspect ratio (nuclear height divided by maximum cross-sectional area) of the reconstructed nuclei to examine how this translated to the 3D size and shape of the nuclei. Figure 3.3a shows that the cell nuclei in thick colonies may reduce in volume, though within group variation makes this uncertain. Nuclei more clearly do alter shape as colonies become thicker, becoming more rounded. The vertical elongation of the nuclei alone cannot account for the height of

thick colonies, and by locating the tops and bottoms of the reconstructed nuclei, the presence of multiple cell layers has been confirmed. Thin colonies, in contrast, grow as single layers like those in conventional, unconfined culture.

Taken together, these results have shown that thicker patterned hESC colonies are composed of multiple layers of cells with smaller nuclei exhibiting a more isometric or vertically elongated shape, while thin colonies resemble convention cultures with a single layer of cells with flattened nuclei (Figure 3.4). Additionally, colonies of all thickness in between these extrema were also produced and exhibited intermediate properties.

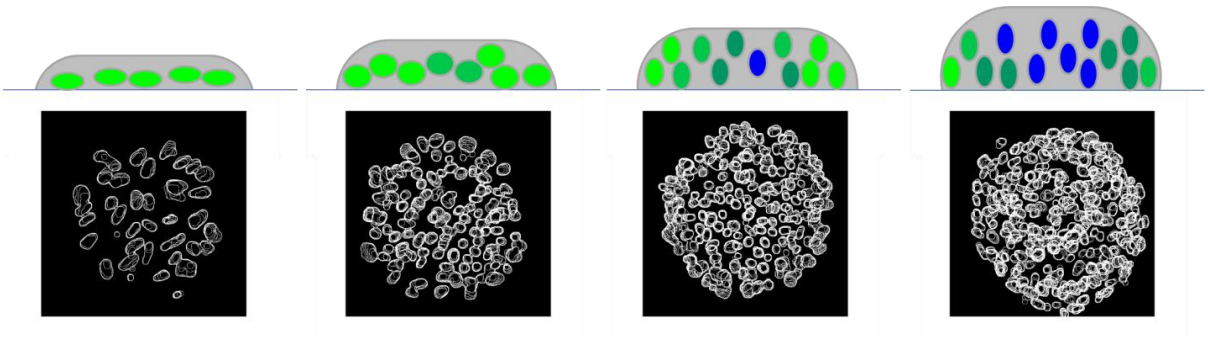

Figure 3.4: Cartoon summarizing the observed morphological trends for nuclei in thin (left) and thick (right) colonies. Each depiction is paired with a contour map derived from the nuclear reconstruction of a representative colony.

Chapter 3.3.3. Spatial heterogeneity of hESC in patterned colonies

Assessing spatial variation of geometric and IF characteristics of cells within the reconstructed patterned hESCs colonies is simplified by their radial symmetry. The lateral variation from all colonies can be projected onto a single axis measuring the distance from the center of a colony in microns. Including an axis representing

the vertical direction allows all spatial variation to be captured in a 2D plot. In Figure 3.5a a series of these vertical-vs-radial plots represents the spatial distribution of nuclear center points from 5 sets of colonies grouped by their thickness. The radial probability distribution function (PDF) is a better representation of the distribution of cells in the radial dimension than a scatter plot because it can be corrected for the linear increase of circumference with radius. In each of these plots the PDF shows that there is little radial dependence of cell density, except in the thinnest colonies. This is due to incomplete pattern filling near the edges of these colonies. Similarly, cells appear to be fairly evenly distributed in the vertical dimension.

Colonies were stained for OCT-4, as well as markers associated with differentiation to early mesoderm (Brachyury), early endoderm (GATA6) and early neuronal (PAX6) lineages. We have observed considerable heterogeneity in the level and pattern of these markers between different experiments, even using the same cell line. Some patterned cultures we examined produced virtually no fully OCT-4 negative cells, though all of our experiments resulted in some tendency towards decreased in OCT-4 in thicker colonies. To illustrate the useful attributes of our method this chapter will focus on results from an experiment that presents a strong geometric influence on the pattern of pluripotency and early differentiation markers. This data set will better serve to demonstrate the method we have

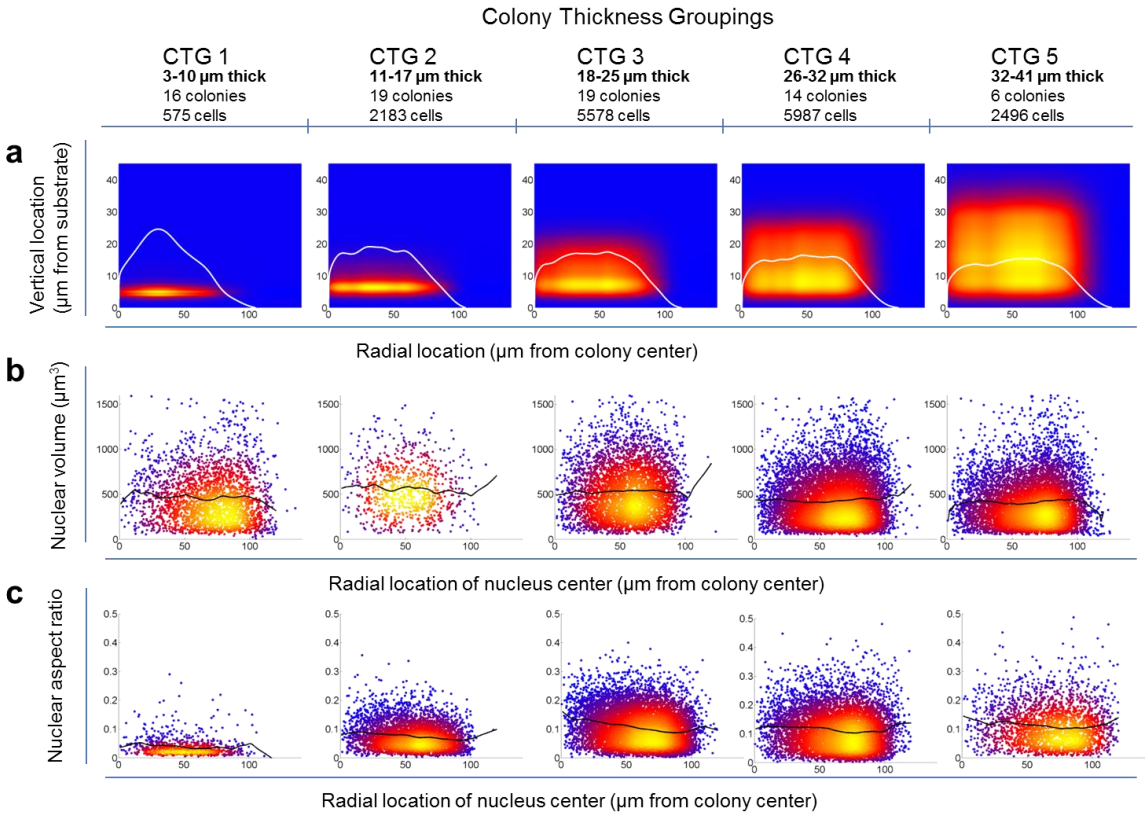

Figure 3.5: The spatial and morphological characteristics of patterned colonies divided into five groupings from thinnest (left) to thickest (right) colonies. (**a**) The spatial distribution of nuclei in each colony thickness grouping (CTG) is represented as a color map of the probability distribution function (PDF) as corrected for the expected linear increase in nuclei number with radial location. The white curve shows the radial PDF alone. (**b**) Scatter plots showing the volume of nuclei versus their radial location for each of the CTGs. Black curve is the average nuclear volume as a function of radial location after smoothing. (**c**) Scatter plots showing the aspect ratio of nuclei versus their radial location for each of the CTGs. Aspect ratio was calculated as the measured height of a nucleus divided by the nucleus' maximum cross-sectional area. Black curve is the average nuclear aspect ratio as a function of radial location after smoothing. Yellow signifies a higher density of nuclei and blue a lower density.

developed, but a much larger future effort could implement this platform to systematically address the broad heterogeneity that makes that limitation necessary now. In this experiment the fraction of nuclei which recorded high OCT-4 IF sums

was observed to decrease in thicker colonies. This was accompanied by thickness-dependent loss of baseline IF from PAX6 and Brachyury in many cells, and an increase in the number of cells with high GATA6 signal.

In Figure 3.6a, by once again separating the colonies into 5 groups based on colony thickness and plotting against the radial dimension, the observed variation in the pluripotency marker OCT-4 in individual cells is seen to have a significant radial dependence. OCT-4 IF signal is measured to be strong for over 90% of nuclei in the thinnest two groups, representing colonies up to 18 μm thick. A notable reduction in OCT-4 is found to occur first in the third group, representing colonies 19-25 μm thick, accumulating a population of cells with very low OCT-4 signal concentrated at low radial distance. This population increases in the fourth and fifth groups, and in the thickest colonies only a relatively small fraction of nuclei concentrated near the colonies' edges retains a normal level of OCT-4 IF signal. Curves showing the average intensity clearly show the radial dependence of OCT-4 (Figure 3.6a). OCT-4 IF intensity does not vary significantly as a function of a nucleus' location in the vertical dimension (Figure 3.6b).

Most nuclei stained for PAX6 and Brachyury possess a consistent baseline level of IF signal in thin colonies resembling conventional cultures (Figure 3.7). We found that in thicker colonies this low level IF signal is lost, mirroring the pattern of radially dependent loss observed for OCT-4. Greater than 56% of nuclei in the thickest colonies have very low Brachyury signal and more than 43% have very low PAX6. Conversely, there does not seem to be a baseline level of GATA6 IF signal (i.e.

nuclear intensity matched background intensity, and most nuclei were measured to have this null value at all colony thicknesses). Also similar to OCT-4, these low intensity nuclei do not display a preference for location in the vertical dimension (Figure 3.8).

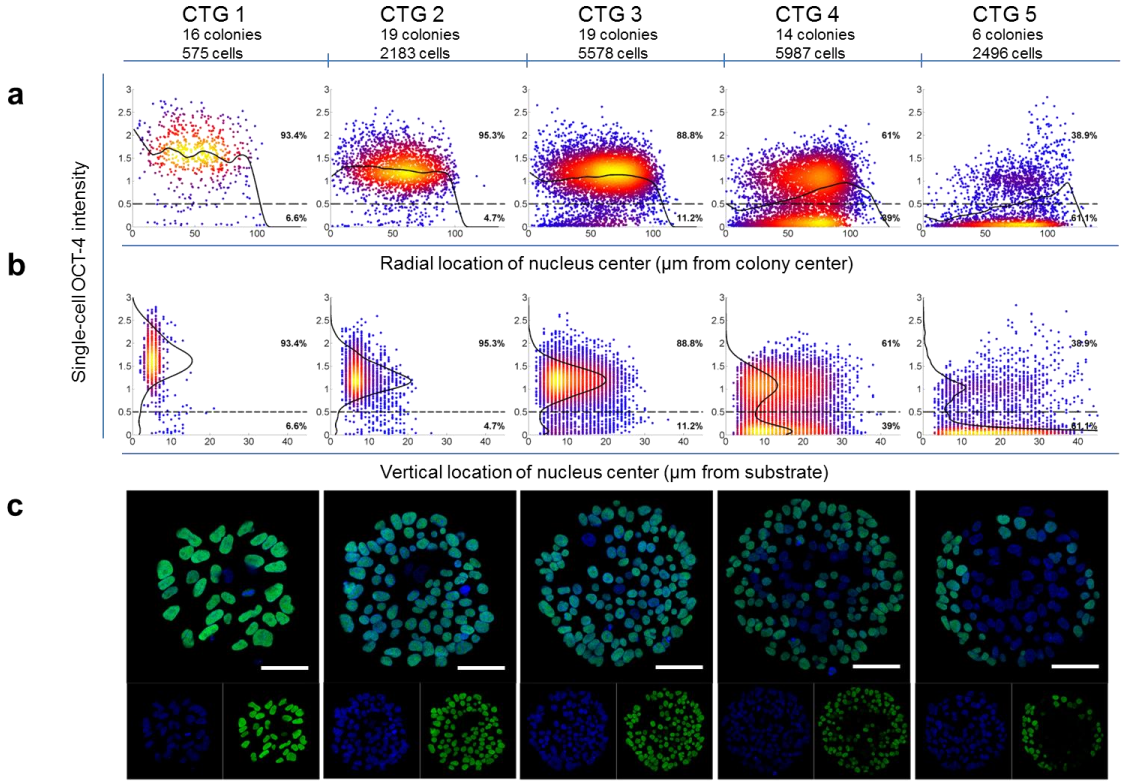

Figure 3.6: The single cell OCT-4 intensity of patterned colonies divided into five groupings from thinnest (left) to thickest (right) colonies. Scatter plots show the OCT-4 intensity measured in each reconstructed nucleus versus the (**a**) radial location and (**b**) vertical location of the center of the nucleus. Percentages indicate the fraction of nuclei located within plot regions designated by dashed lines (**c**) Representative images from a colony in each thickness grouping. Scale bar is 50 μm.

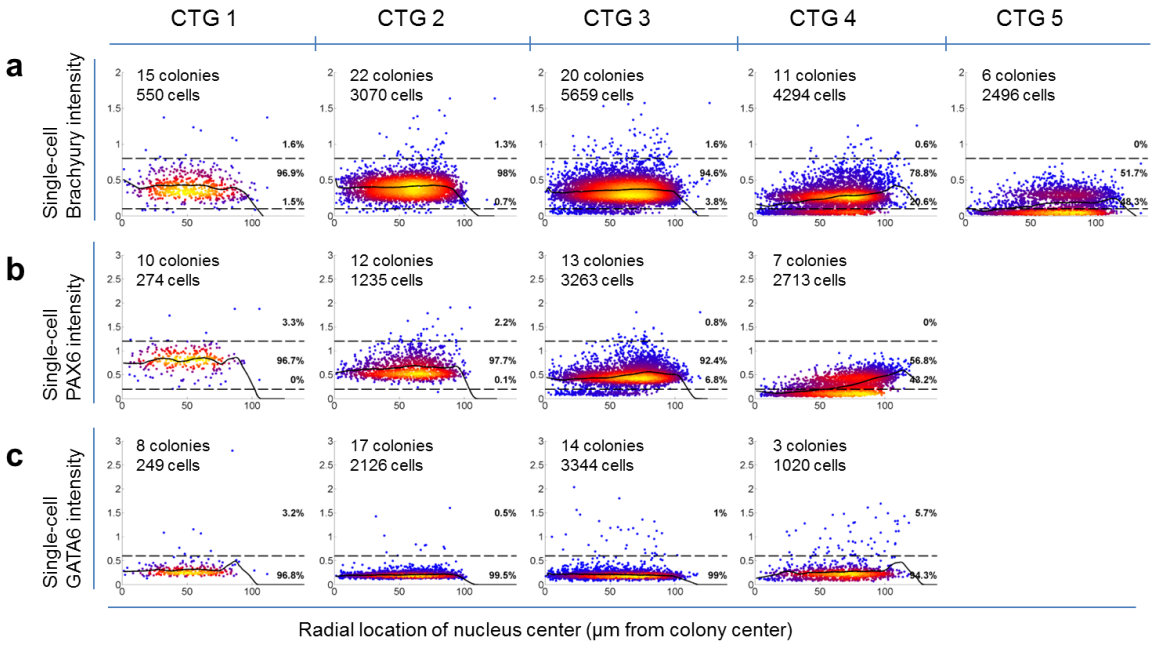

Figure 3.7: Scatter plots of the single cell (**a**) Brachyury, (**b**) PAX6, and (**c**) GATA6 intensity of patterned colonies divided into five groupings from thinnest (left) to thickest (right) colonies, as function of radial location.

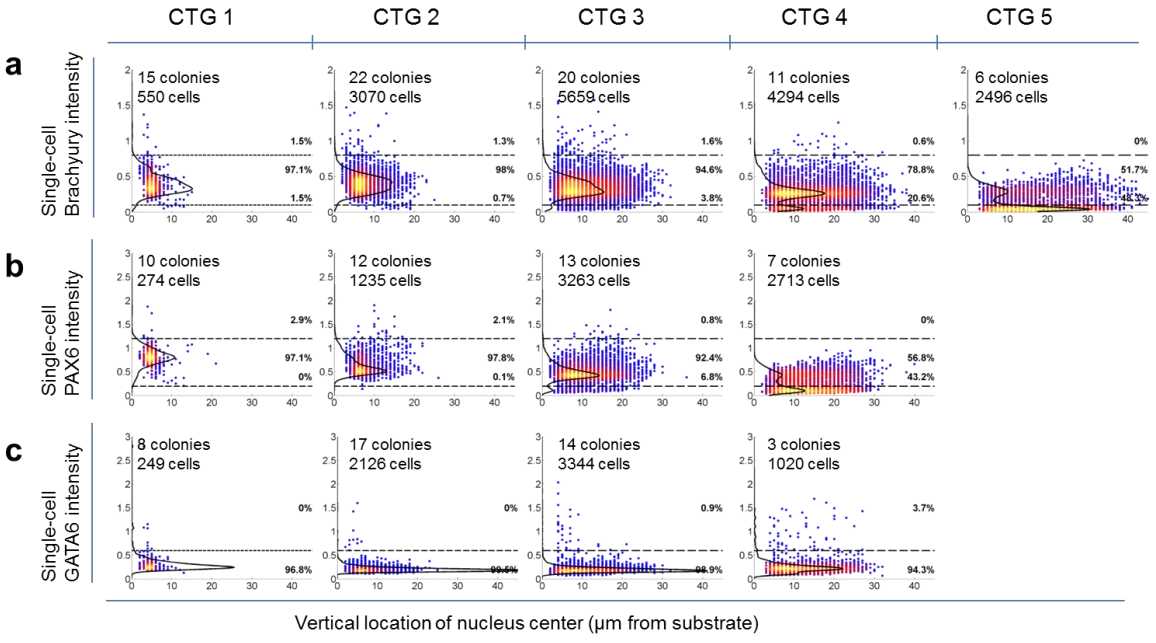

Figure 3.8: Scatter plots of the single cell (**a**) Brachyury, (**b**) PAX6, and (**c**) GATA6 intensity of patterned colonies divided into five groupings from thinnest (left) to thickest (right) colonies, as function of vertical location.

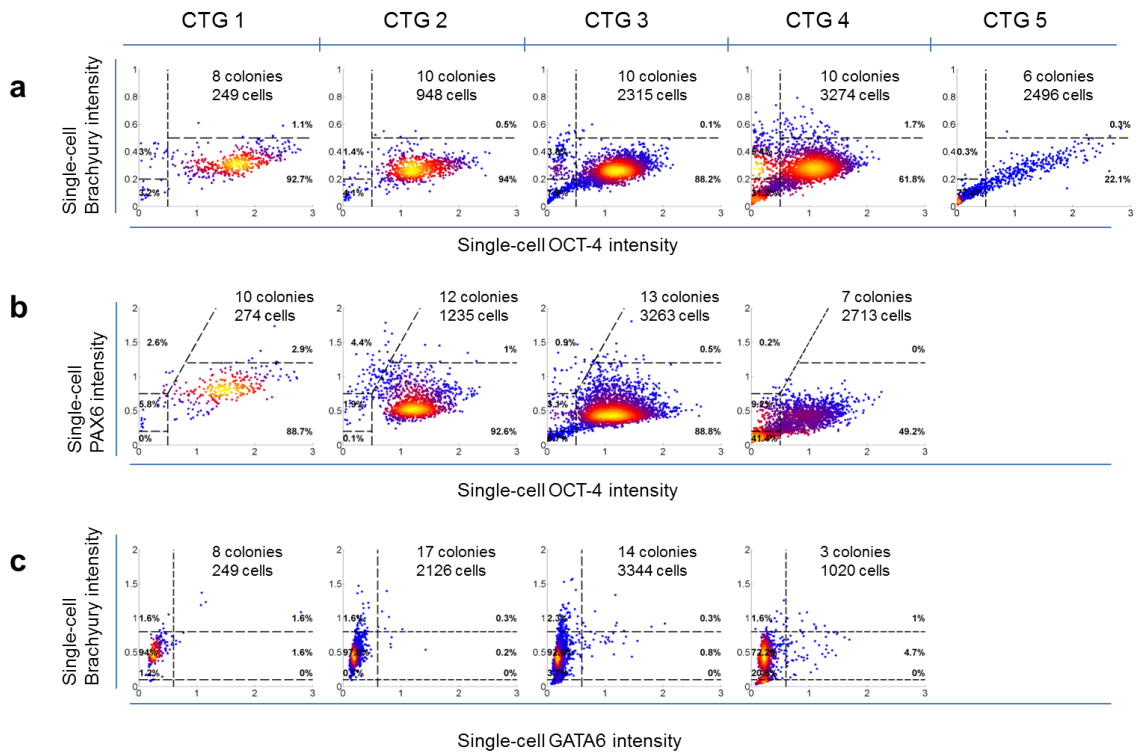

Figure 3.9: Scatter plots for each colony thickness group showing the correlation between the single cell intensity of (**a**) Brachyury versus OCT-4, (**b**) PAX6 versus OCT-4, and (**c**) Brachyury versus GATA6.

The colonies also contain a small number of bright nuclei that have summed IF signals above the average values for each early differentiation marker. For Brachyury and PAX6 these bright nuclei diminish as a fraction of the total and are also more likely to be centered in the outer portion of the colony as colonies become thicker. Alternatively, nuclei that have bright GATA6 signal become more prevalent in thicker colonies and appear to be equally distributed in the radial dimension. In the vertical dimension GATA6 and Brachyury bright nuclei are concentrated near the bottom of colonies, though this effect appears reduced in thicker colonies.

Nuclei staining bright for PAX6 are the least frequent and do not show any strong tendencies with z-height.

Direct correlation between two markers can be examined in colonies that were stained for both (Figure 3.9). The respective relationships of OCT-4 intensity with PAX6 and Brachyury follow the same broad trend. Scatter plots comparing both sets of markers in the thinnest colonies show nearly all nuclei as having baseline PAX6 or Brachyury, and OCT-4 intensity. In the thickest colonies a large fraction of nuclei have very low IF signal for all markers. In colonies between 11 μm and 18, nearly 4% of nuclei μm make up a population with high PAX6 and low OCT-4 signal. Notably, nuclei with high Brachyury and low OCT-4 are observed most frequently in colonies thicker than 26 μm, while the high PAX6 nuclei are found in colonies this thick. We were also able to directly compare GATA6 and Brachyury intensity. In the thinnest colonies, the Brachyury-bright nuclei are also GATA6-bright. In all colonies other than the thinnest, nuclei bright in only one marker or the other are present.

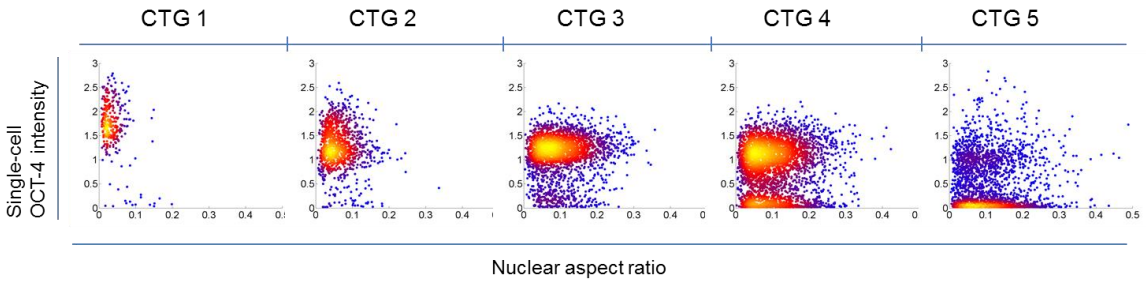

Figure 3.10: Scatter plots for each colony thickness group showing the correlation between the single cell intensity of OCT-4 and nuclear aspect ratio.

The geometric characteristics of the reconstructed nuclei, volume and aspect ratio, do not appear to vary meaningfully with the cells location within the colony (Figure 3.3b-c). Neither is there any strong direct correlation between these properties and the IF signals from the nuclei (Figure 3.10). While changes in both morphological and IF signal occur with increased colony thickness, if a causal relationship exists between these two effects it must be indirect, possibly acting on the colony as a whole and then propagating via paracrine signaling.

Chapter 3.4. Discussion:

To study the spatial variation of hPSCs within colonies requires examination on a single cell level. Confocal imaging can provide the connection between the biochemical state of a single cell, which can now be measured more efficiently using other conventional tools of modern biology, and the physical state of a cell, which is often discarded in these other methods during cellular dissociation. However, the irregularity of hPSC cultures poses challenges to any effort to study spatial patterns in colonies in which the fundamental spatial parameters of size and shape are uncontrolled. By combining confocal microscopy with uniform colonies in a patterned culture system, spatially-informed single cell data can be generalized for many colonies. The work presented in this chapter demonstrates several advantages that this system offers that complement existing technologies, which will be discussed in this section. Critical to these advantages is the automated software that allows a large number of colonies containing thousands of cells to be

analyzed together. It is important to consider that this type of automation can introduce artifacts into the processed data. This section will also discuss the steps that have been taken to proof against this in our method.

Chapter 3.4.1. System Capabilities

We have developed a method of studying hPSCs in patterned uniform colonies. This method offers the unique ability to examine the *in situ* spatial, morphological and transcriptional state of a large number of individual cells within intact colonies. Additionally this system has the potential to assess the effects of colony confinement on maintaining pluripotency or driving differentiation. By performing an automated analysis of confocal image z-stacks acquired from uniform circular colonies, the location, shape, and IF staining of individual nuclei are reconstructed in 3D. These data can then be aggregated for any number of equivalent uniform colonies and the nuclear characteristics examined in relation to one another in ways not possible by other means.

The ability to measure *in situ* spatial morphological properties of populations of hPSCs in colonies makes our approach complementary to conventional methods. Fluorescence activated cell sorting (FACS) would certainly provide high throughput data on transcriptional markers for a large number of hPSCs, but hPSCs dissociated to single cells will assume a spherical conformation in suspension. In this case all information regarding the biomechanical influences from the cells native conformation is lost. Such biomechanical cues have shown capable of significantly influencing lineage commitment[158,159]. Similarly, the relative location of individual

cells within colonies cannot be tracked once cells are dissociated for analysis. While single-cell qPCR has been employed to compare RNA expression from cells in different regions of colonies, this method is difficult and costly, and thus limited in the number of cells that can be examined[54]. Furthermore, in conventional cultures location must be crudely estimated within irregular colonies. The location information presented here can be represented precisely for a large number of cells because of the equivalent geometry of the patterned colonies.

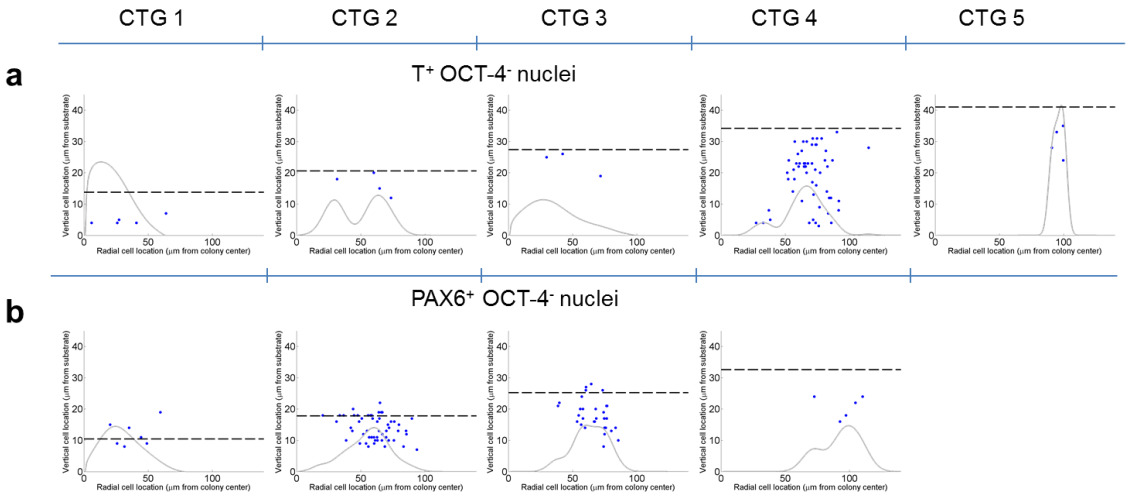

Figure 3.11: Sub-populations separated based on having low OCT-4 intensity and high intensity from an early differentiation marker from each colony thickness group. Scatter plots show the radial and vertical locations of (**a**) T^+ $OCT\text{-}4^-$ and (**b**) $PAX6^+$ $OCT\text{-}4^-$ nuclei. Gray curves show the radially corrected PDFs for each sub-population. Dashed lines indicate the nominal thickness limit for colonies in each thickness group.

The confidence placed in information extracted from conventional confocal microscopy can be limited by the small size and number of images, as well as an inability to reliably combine data from multiple images. Introducing quantifiable

methods with a large number of samples can overcome these limitations, but extracting spatially informed data then requires spatially equivalent samples[154]. To best quantify spatial information within a large number hPSC colonies, the spatial aspects of the colonies should be regularized to provide good equivalency of spatial data from multiple images. Our results show that by patterning colonies using μCP, the variability of transcription factor IF as a function of cell location can be measured from a large number of colonies. Measuring this type of variability provides new insights to understanding the dynamic heterogeneity that seems to exist in hPSC colonies, and to tuning culture conditions at all stages to be optimized towards the desired lineage-specific differentiation. This system also allows the investigator to first identify populations of nuclei based on multiple IF channels, then track the spatial trends of only that population. For example, the population of cells identified in Figure 3.9 with nuclei that stain bright for PAX6 and dim for OCT-4 ($PAX6^+/OCT\text{-}4^-$) have been separated and located in the vertical and radial dimensions as a function of colony thickness (Figure 3.11). The radially corrected PDF can then calculated for only these isolated nuclei. The peaks of these PDFs show that the population is observed to exist near the center of thin colonies, and then move gradually toward the periphery as colonies become thicker. They also tend to be found near the tops of colonies of all thicknesses. Being able to predict the location of rare populations of differentiating cells within an hPSC colony could be a powerful tool to aid in directing lineage specification from the pluripotent stage onward. While the trends observed here may not be realistic due to the small

numbers of cells, the ability of this system to accumulate significant numbers of rare cells from a large number of equivalent colonies puts this tool within reach. Moreover, individual nuclei can be picked out and examined in the original images for morphological information not quantified in the analysis. For instance, a very dim nucleus can be found in the original image, identified as a large piece of debris with non-specific DAPI staining, and removed from the dataset (Figure 3.12). This ability represents an important failsafe, which is made possible by the convenience of using images as the raw data for analysis.

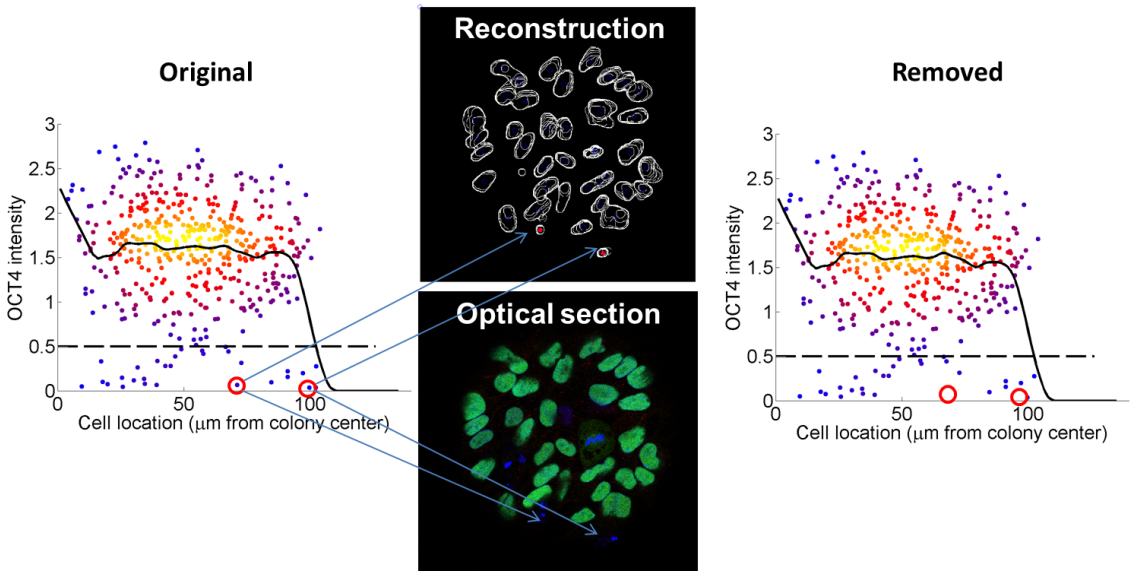

Figure 3.12: Demonstration of the removal of erroneous data points though inspection of original images. Points in question are identified in a scatter plot (left), then traced back to colony and optical section showing them to be debris falsely recognized as nuclei, and then eliminated from the analysis.

Regularizing the culture of hPSCs may be important for scaling-up and improving reproducibility of differentiation potential for wide clinical translation in

the future[156]. While creating colonies of uniform size and shape can be achieved in a number of ways, to do so has required that colony growth be confined to defined areas on a culture platform, either chemically or physically. While this approach has been shown to be effective at creating uniform hPSC colonies that can be tailored to prime for specific lineage differentiation[160], the effects of the confinement itself, either useful or deleterious, have not been fully explored. The combination of automated confocal image analysis with μCP confined hPSC colonies investigated here once again represents a well-suited tool for this undertaking. We have shown that patterned confinement has the potential to induce a significant increase in the thickness of colonies not found in unconfined colonies. The loss of OCT-4 in the center of thicker colonies suggests that extra care may need to be taken to tightly control the seeding distribution and time in culture for patterned hPSCs to be maintained in the pluripotent state. Alternately, the varying rate of incidence of cells with high levels of early differentiation markers may provide clues to allow the confinement induced thickness of a pluripotent colony to be optimized for the onset of directed differentiation.

Although the unique capabilities of our system offset some of the limitations of current analytical methods, the system also has limitations that should be clearly outlined to direct its development and use. An important limitation, shared by other imaging methods as well as FACS, is that the reliance on IF tags to measure the presence of biomolecules limits the number of targets that can be simultaneously studied. Typically, a maximum of 4 dyes are used to prevent cross-talk, which

prevents the direct correlation of many antigens in a single colony. To overcome this limitation, more cultures could be used in combination, but this must be weighed against the other principal limitation of this system, which is the time-consuming nature of imaging. While larger numbers of cells can be easily analyzed compared to single cell qPCR, the throughput is much slower than FACS. Possible methods of addressing these shortcomings are discussed in Chapter 6.

Chapter 3.4.2. Eliminating Potential Artifacts

In automated analysis such as the one described here, the generation of artifacts that can alter the real results must be considered and guarded against. We have tested our system against several anticipated potential sources of artifacts and built in protections to ensure that the results obtained represent real phenomena. An error that we have observed and optimized our system to minimize is the incorrect tracking of nuclei which results in multiple nuclei being analyzed as a single nucleus. Despite, our efforts this type of error is difficult to guarantee against as some nuclei will inevitably be too close to each other laterally or be directly above or below one another. In addition this error would be expected to affect thicker colonies disproportionately since those colonies have more layered nuclei packed more closely together. Consequently, measurements of cell density, nuclear geometry, and how these properties relate to colony thickness could be called into question. However, our observation that cell density increases with colony thickness is in direct opposition to the artifact that would be predicted from a large number of nuclei being counted in clusters. Similarly, another predicted effect would be an

increase of nuclear volume in thicker colonies if multiple nuclei were merged. Once again we measure an opposite trend towards smaller nuclear volumes in thicker colonies in Figure 3.3a.

Of particular concern with consolidated nuclei was the effect this would have on single cell IF signal results. Since small populations of bright cells can represent an important result, even a small number of double-nuclei could skew conclusions. To prevent this artifact, each IF value is normalized to the nuclear volume of that nucleus. Additionally, this guards more generally against any error in accurately reconstructing nuclear shape. Due to static parameters in the image manipulation routines that define nuclear regions, this error likely scales with the size and shape of the nuclear cross-section, which can vary even within colonies. The presence of this type of error is supported by the notable spread of nuclear volumes indicated in Figure 3.5b. Indeed, comparing analysis utilizing non-normalized intensity sums in Figure 3.13 to normalized intensities in Figures 3.6 and 3.7 shows loss of distinct populations indicating the that this error is sufficient to obscure more subtle IF features. The non-normalized intensities also show a significant increase in the number of high intensity nuclei, likely representing the effects of the spurious consolidation of nuclei.

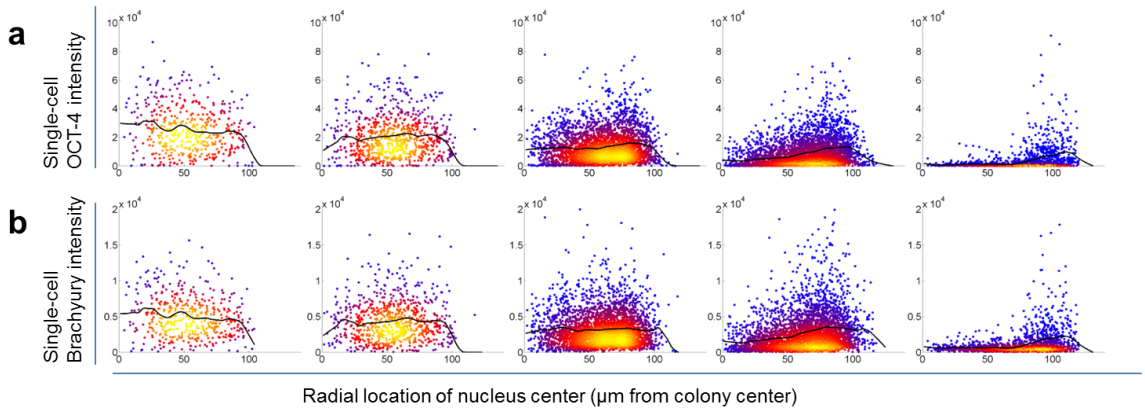

Figure 3.13: Scatter plots for each thickness group showing IF intensities not normalized by the volume of the nuclei for (**a**) OCT-4 and (**b**) Brachyury versus radial location. Source data is the same as used to prepare Figures 3.5a and 3.6a where volume normalization was employed.

Another important consideration is the error in the estimation of colony height, and subsequently colony volume. Since the colony height is based on the top most vertical location of signal from the nuclei, some volume from the cytoplasm of the top layer is excluded. Once again the observed trend of greater cell density in thicker colonies does not appear to be unduly influenced by this effect. Ignoring cytoplasmic volume from only the top layer should introduce a proportionally greater error in thinner colonies resulting in an overestimation of the cell density in those colonies over the thicker ones, opposite to what is observed. It is likely that effect is limited by the small volume that the ignored cytoplasm represents.

In addition to artifacts introduced in the image analysis, there are several that might arise in arise in the acquisition as well. In quantitative confocal analysis there is a significant potential for error coming from variation in IF signal with z-

height[161]. The excitation and fluorescent light going in and coming out of the sample is scattered by cells as it passes through them, making an equally bright nucleus appear dimmer if it is located at a higher position. To combat the distortion this could cause in our results, the IF signal from each pixel in an optical section is normalized to the average per-pixel intensity of the DAPI channel in that section. DAPI staining is assumed to be invariant with z-height. For simplicity this design must also assume equal scattering between different wavelengths.

Despite the protections engineered into the Zeiss confocal system, we were concerned that signal might be "leaking" between channels, meaning that fluorophores bound immunohistochemically to one protein of interest, might contribute to the signal of a channel representing another protein. This concern arose from the similar pattern we observed for OCT-4 and the differentiation markers in the variation of single cell IF signal with thickness. In each marker the average intensity drops near the center of the colonies in thicker colonies. Additionally, some degree of direct correlation can be observed between OCT-4 and Brachyury and PAX6, respectively. Given the relatively strong signal of the OCT-4 IF compared to Brachyury and PAX6, it was possible that even a small signal crossover from the former could dominate the latter. However, IF cross-over would produce signal correlation down to the level of pixels[162]. By examining the detailed co-localization of the fluorescence within the nuclei we have shown that channel "leaking" cannot account for these correlations. Had this been the case we would expect to observe a reproduction of the pattern of OCT-4 intensity within a nucleus

in the Brachyury or PAX6 of that nucleus. We found instead that most nuclei had easily discernible differences (Figure 3.14), indicating that that correlations in summed nuclear intensity between channels represent a biological phenomenon.

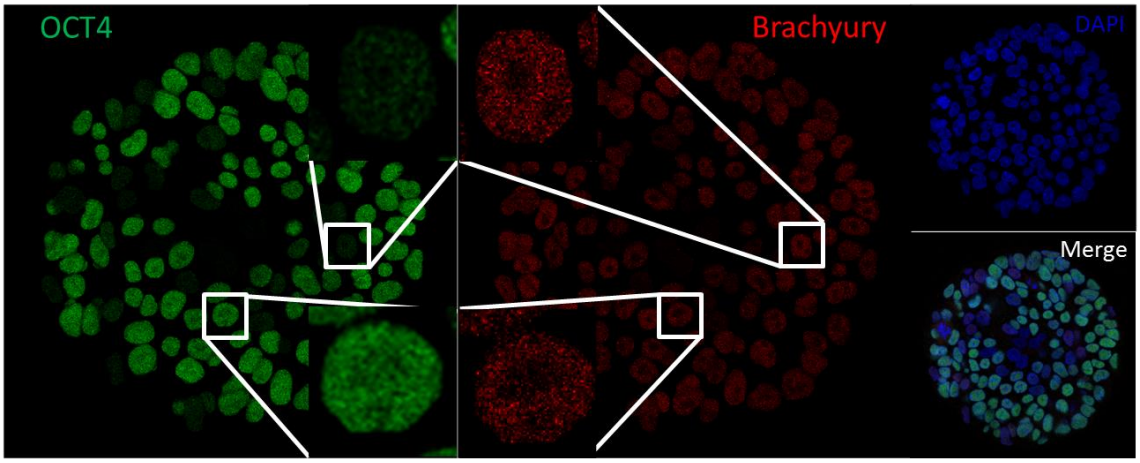

Figure 3.14: Confocal images showing the distinct localization of IF signal in the OCT-4 and Brachyury channels from a representative colony. Details visible in enlarged individual nuclei (inset) show the regions of high and low intensity do not agree between the two channels.

Finally, because the IF signal, especially OCT-4, decreases near the center of thicker colonies, it is prudent to consider the possibility that this effect results from restricted antibody penetration[163]. However, once again examining the images reveals that this is likely not the case. The expectation in the case of poor antibody penetration would be the appearance of a gradient of signal from the surface cells exposed to free solution to the cells deepest within the colony. While some colonies do seem to exhibit a radial gradient, many others contain a mix of bright and very dim nuclei adjacent to one another and located at various radial locations.

Moreover, we observe neither gradient nor any variability in OCT-4 signal in the vertical dimension. Given that this dimension represents a shorter diffusion distance for antibodies to reach the cells furthest from a colony surface, explaining radial variation by a diffusion-limited process is not realistic.

Chapter 3.5. Conclusions

Studying hPSC colonies confined to uniform size and shape through the automated analysis of confocal image z-stacks provides an important new tool for the stem cell biologist. Importantly, this tool offers the ability to examine spatial variation in the properties of single hPSCs in colonies with controlled geometric parameters. We have demonstrated that this ability has the potential to uncover a wealth of meaningful biologically relevant relationships between the physical and transcriptional state of hPSCs. The full complexity of these interactions can now be investigated in expanded studies involving any number of equivalent patterned colonies. This system's unique combination of capabilities affords new opportunities to understand the spatial component of heterogeneity in the pluripotent state, to uncover new insights into the spatial dynamics of early differentiation within colonies, and to assess the potential advantages and pitfalls of large-scale standardized culture of hPSCs in patterned colonies. While many improvements and modifications will surely be needed, the work presented here has laid the groundwork for these important applications.

Chapter 4. Templated scaffolds for tissue engineering applications

Chapter 4.1. Introduction

Developing methods to replace diseased tissue with engineered constructs remains a central therapeutic goal in regenerative medicine. Many tissue engineering approaches focus of artificially reproducing the native structure of a tissue within constructs. The structural design of these constructs may directly influence the final function of the organoids[96], or provide cues to encourage the cellular mechanisms that lead to the development proper function[164]. In many cases scaffolds are used to provide the structuring as well as mechanical support so that the construct can be cultured outside of the body under controlled conditions before being implanted. While scaffolds have been successfully prepared from a number of materials by a variety of techniques, one established means of introducing structure in scaffolds is templating[96,121,165,166]. Typically, a template material and a scaffold material are integrated together in some structured manner during the formation of the scaffold. When the template is removed, the structure of the scaffold is defined by the void space created.

This chapter will detail work in which we have employed structural templating to recreate two different types of tissue engineered constructs. In the first of these, we have built upon the conventional method of templating pores within a solid polymer material by leaching a sacrificial porogen. This method provides a large polymer surface area which is available for cell attachment and colonization, while the pores allow for efficient nutrient infusion and room the

eventual tissue formation, including vascularization. In this way we have constructed poly(lactic-co-glycolic acid) (PLGA) scaffolds with hierarchical porosity by the inclusion and subsequent leaching of salt particles in order to develop a cartilage mimicking construct. The second construct we have created represents the first step towards the development of a functional engineered lung tissue. In this case, templating the gas compartment of the tissue was critical, but the conventional paradigm of templating the pores in a solid support needed to be rethought. The presence of a solid support was considered likely to interfere with the extremely intimate cellular contact required for gas exchange. Our solution was to directly template the structure of the organoid as it grows in culture. This was achieved through the use of alginate microbeads to template the alveolar sacks. Alginate is non-toxic, and both its presence and removal are compatible with cell culture.

Chapter 4.2. Experimental Methods

Chapter 4.2.1. Materials

Poly(lactic-co-glycolic acid) was purchased from Evonik. Calcium chloride, sodium chloride, methylene chloride, low melting point agarose, and low viscosity sodium alginate were purchased from Sigma-Aldrich. Heptadecafluro-1,1,2,2-tetrahydrodecyl-1-trichrlorosilane was purchased from United Chemical Technologies.

Chapter 4.2.2. Preparation of salt-templated PLGA foam scaffolds

Sodium chloride (NaCl) particles were milled for 2 hours with ceramic milling media on a rolling ball mill. The resulting powder was sieved sequentially

through brass wire sieves with nominal size cutoffs of 250, 106, 55, and 38 μm. PLGA was dissolved in methylene chloride at a concentration of 100 mg/ml. In a typical experiment 1.67 g of salt grains in the 106-250 μm size range was mixed by vortex with 390 mg of salt grains less than 38 μm. The salt mixture was added to 0.5 mL of the PLGA solution, then mixed by vortex, and sonicated for 5 min prior casting. Sheets of PLGA-salt composite were cast onto polytetrafluoroethylene (PTFE) circular mold with a diameter of 35 mm. Molds were lined on the bottom with a coverglass of the same size which had been clean in a bath potassium hydroxide in ethanol, then treated under vacuum with heptadecafluro-1,1,2,2-tetrahydrodecyl-1-trichrlorosilane. This produced a sheet approximately 2 mm thick. The mold was held under vacuum over night to remove the methylene chloride, and then the PLGA was detached from the mold side wall with a blade. The perfluorinated glass liner made it easy to remove the casting from the mold first, and then carefully detached from the coverglass. Circular scaffolds were next prepared from the sheet by using a steel punch with an inner diameter of 6.35 mm. These disks were then placed in a jar of deionized water to remove the NaCl template, which was changed twice in 24 hrs. After a final rinse in deionized water the foam scaffolds were sealed in 100% ethanol to sterilize them.

Chapter 4.2.3. Biphasic bioartificial cartilage construct formation

Human fetal tissues were obtained from Novogenix Laboratories, LLC (Los Angeles, CA) following informed consent and elective termination. All donated material was anonymous and carried no personal identifiers. Developmental age

was determined by ultrasound. Periarticular cartilage tissue was isolated under dissection microscope from 17-week-old human fetuses. Cartilage was digested for 20–22 h in collagenase type II (0.15%) in DMEM supplemented with penicillin (100 U/mL) and streptomycin (100 mg/mL). Chondrocytes were then cultured in chondrocyte proliferation medium (DMEM/F12 supplemented with 10% FBS and 100 U/ml penicillin and 100 μg/mL streptomycin). Medium was refreshed every 3-4 days.

Bone marrow was flushed out from femur and tibia bone marrow cavity. Mesemchymal stromal cells (MSCs) were obtained by plating the whole bone marrow at a density of 50k/cm^2 in a culture flask in MSC proliferation medium (α-MEM, supplemented with 20% fetal bovine serum, 100 U/ml penicillin and 10 μg/ml streptomycin). Medium was refreshed every 3-4 days until confluence.

PLGA foams were removed from ethanol soaked in sterile water overnight. Foams were then rinsed with water then PBS and placed in a 24-well plate. MSCs were resuspended in Matrigel at a density of 10×10^6 cell per mL. Foams were drained of excess water with a sterile cotton applicator prior to slowly seeding the 100 μL of the MSC suspension onto each. The Matrigel was then set by incubating at 37 °C for 5 min. Agarose was melted in a double boiler then cooled to 37 °C in a water bat at that temperature. Chondrocytes were resuspended in argarose at the same density as MSCs and 100 μL was formed into a drop let on top of the Matrigel filled PLGA foam. Constructs were brought to room temperature to set the agarose before adding medium and returning them to the incubator. Bi-phasic constructs

were cultured in MSCs proliferation medium for 14 days before histological examination.

Bi-phasic constructs were fixed in 10% formalin for 15 min, dehydrated with ethanol and embedded in paraffin using routine procedures. A microtome (Leica, Germany) was used to cut 5 μm sections. Slides were then deparaffinized and stained with hemataxyline and eosin (H&E). For immunohistochemistry, paraffin sections were processed using routine techniques. Rabbit antibodies against COL (Abcam, USA) were used, followed by incubation with HRP conjugated secondary antibodies against rabbit IgG (Vector Laboratories, Burlingame, CA). Antibodies were then visualized with Peroxidase substrate Kit DAB (Vector Laboratories, Burlingame, CA).

Chapter 4.2.4. Scanning electron microscopy

Foams were prepared for imaging by drying under vacuum for 24 hrs, cooling them in liquid nitrogen, and then fracturing them with a blade. Foams were then mounted and sputter coated with approximately 10 nm of a Au/Pd alloy. Imaging was done with a Hitachi S4700 SEM at an accelerating voltage of 5 kV and a current of 5 mA.

Chapter 4.2.5. Alginate bead generation

Sodium alginate was first dissolved overnight in deionized water at a concentration of 3 wt%. This solution was then sterilized by filtration with cellulose acetate syringe filter with nominal pore size of 0.45 μm in a sterile cabinet. The sterile alginate solution was then loaded into a sterile 20 mL syringe and capped

with 30 gauge blunt needle with a 90 degree bend, which was mounted in a syringe pump (Harvard Apparatus). A 100 mM solution of $CaCl_2$ was made with deionized water and sterile filtered. This was stirred magnetically below the needle of the alginate filled syringe. To form the beads the syringe pump was set to a flow rate of 6 mL/min. The needle was charged to a voltage of 6 kV via a 0-30 V power supply amplified with a low current HV module (EMCO), and a grounding lead was submerged in the $CaCl_2$ bath. Beads were washed multiple times with sterile water and stored at 4°C in a solution of 1 mM perimycin in sterile water.

Chapter 4.2.6. Lung progenitor fibroblast derivation from hiPSCs

Fibroblast cells (1 x 105) from lung biopsies were plated in a CELLstart-coated well of a six-well plate in MSCGM-CD medium. After 8 hours, the cells were transduced with vector concentrate (7 × 106 TU/ml) in 1 ml of MSCGM-CD medium containing 10 μg/ml polybrene and incubated overnight at 37°C in 5% CO2 incubator. The vector-containing medium was aspirated, and the cells were rinsed three times with MSCGM-CD and further cultured for 3 days in the same medium. Cells were replated on the fifth day in 50:50 TeSR2/Nutristem containing 10 ng/ml bFGF in two 6-cm dishes coated with CELLstart and cultured until hiPSC-like colonies were formed. The colonies were picked mechanically and cultured in CELLstart-coated dishes, passaged mechanically using the EZPassage tool as per the manufacturer's protocol. The colonies were collected by gentle pipetting using a serological pipette, transferred to a 15-ml tube, and passaged at the ratio of 1:6 into a new CELLstart-coated plate. Colonies were expanded and stored.

Five to seven days before the start of the mesenchymal differentiation protocol, one confluent 3cm2 dish of IPF patient lung fibroblast derived iPSC culture was split 1:6. The iPSC's were at least 40-50% confluent by day 5-7. Embryoid bodies were prepared by washing the plate once gently with DMEM/F2 (Cat# 11330-032, Invitrogen) followed by incubation with 1 ml/well of warm 1mg/ml dispase (Cat # 17105041, Life Technologies) at 37oC. After 5-7 min of incubation, the wells were rinsed gently 3 times with 1 ml warm DMEM/F12. Colonies were scrapped, collected in medium, allowed to settle and then washed once with 5ml of embryoid body (EB) medium. The EB's were then plated on ultra-low attachment plates and incubated at 37oC, 5% CO2 humidified incubator for 6 days.

The EB's were allowed to spontaneously differentiate by collecting them and re-seeding them on gelatin-coated dishes in the differentiation medium as adherent cultures. Media was changed every other day and outgrowths were collected after 30 days by trypsinization, passed through a 40u filter and re-seeded on gelatin-coated dishes. The procedure was repeated for two passages, and the culture at this point contained mainly cells of mesenchymal lineage.

Chapter 4.2.7. Sodium citrate alginate bead dissolution

In a 24-well tissue culture plate 50k fibroblasts were plated and cultured for 2 days to allow attachment. DMEM media supplemented with 10% FBS was doped with varying concentrations of sodium citrate. These solutions were then each added to one well with the attached fibroblast, and one well with 500 mg of ~3 mm beads prepared without electrostatic size reduction. The solution on these wells was

changed every 2 hours and the state of the beads and cells was monitored for changes for 24hr.

Chapter 4.28. Lung organoid formation

IPSC-derived lung fibroblasts were maintained in DMEM/F12 containing 10% Fetal Calf Serum, MEM Non-Essential Amino Acids, GlutaMAX (Life Technologies) and 100 ug/ml Primocin (InvivoGen). Cells were harvested using TrypLE (Life Technologies) and approximately 400,000 cells were seeded for each experiment.

Prior to organoid formation alginate beads were soaked overnight in DMEM F12 media. Beads were washed with sterile water and dried by centrifuging in a 100 μm mesh strainer then placed on ice. The components of the 3-D Life Dextran-CD Hydrogel (Cellendes) were thawed on ice. In a typical experiment, 11 μL of the maleimide-dextran solution (30 mM maleimide groups) was added to 22 μL of water and 8 μL of pH 5.5 reaction buffer. This was treated with 33 μL of the RGD thiolated peptide (3 mM) for 5 minutes. Dissociated single cells were spun into a pellet and the supernatant was aspirated before briefly chilling the pellet with ice. The peptide-modified dextran was used to resuspend the cells and this was combined with 100 mg of beads in a well of a 24-well plate also chilled on ice. To this 20 μL of the MMP-cleavable dithiolated crosslinker (20 mM thiol groups) was added and rapidly mixed. This was immediately place in a 37°C incubator for the gel to set for 5 minute, after which time media was added. This media was changed

after 1 hour and subsequent media changes were made every 1-2 days while the organoid developed.

Chapter 4.2.9. Live cell confocal microscopy

Live organoids were incubated in 50 μL of a 1 mg/mL solution of Calcien in DMEM media with 10% FBS for 60 min at 37°C. This stained the cytoplasm of live cells. Confocal image z-stacks were acquired on a Zeiss LSM 700 laser scanning inverted confocal microscope through a x5/.5NA objective. Optical sections at 10 μm intervals were obtained using a pinhole of 7.4 airy units. Scan speed was set to a dwell time of 1.58 micro-seconds per pixel. Electronic gain of the photomultiplier tube was set to leave minimal number of saturated pixels in a representative image and maintained for all z-stacks with the same staining.

Chapter 4.3. Results and Discussion

Chapter 4.3.1. PLGA Foams for Tissue Engineered Cartilage

The overall design approach of our tissue engineered cartilage was a biphasic construct. This design was based on biological evidence observed in Prof. Denis Evseenko's lab that signals provided by mesenchymal stem cells (MSCs) support the ability of chondrocytes to produce cartilage extracellular matrix (ECM). To utilize this signaling in a construct required that we provide the distinct environment necessary for the two cell types and prevent MSC matrix production from interfering with development of a functional cartilage matrix. In our biphasic design the first material phase is a hydrogel that encapsulates chondrocytes in the spherical geometry observed *in vivo.* The role of the second component, templated

PLGA foam, is to both provide mechanical support for the construct as a whole, and support the growth and signaling function of the MSCs.

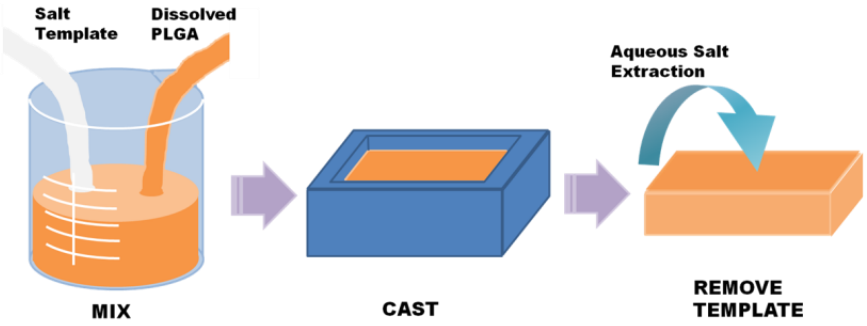

Figure 4.1: Schematic representation of the process of preparing a NaCl templated PLGA foam scaffold.

The selection of an appropriate commercial PLGA was critical to the aims of this research. As described above the properties of PLGA can be varied widely to by adjusting the molecular characteristics, such as molecular weight and ratio of lactic to glycolic acid monomer units. For our cartilage tissue construct the important parameters were a relatively short degradation time, and sufficient mechanical support. While a lower molecular weight and ratio of lactic to glycolic acid near unity will produce the most rapid degradation, we have found experimentally that high-surface area structures made from PLGA with a nominal glass transition temperature (T_g) below 45°C will undergo some form relaxation deformation over long periods of time in culture at 37°C. To overcome that we selected for our scaffolds a polymer that exhibited a T_g of 51°C. This polymer has a 3:1 ratio of lactic to glycolic acid but does not produce a measurable melting point. This indicates that

in large part the higher T_g is result of higher molecular weight. This is preferable to the presence crystalline domains, which would also impart thermal stability (PLGA melting points tend to be near 150°C), but would also greatly reduce degradation rates.

To create a scaffold structure that would offer both a large surface area for the attachment of MSCs and sufficiently open porosity to permit efficient transport of signaling molecules to the chondrocytes in the gel phase, we designed a hierarchical architecture. To realize a hierarchical porosity by salt templating we used salt grains in a mixture of sizes (Figure 4.1). In this simple but effective approach sieved salt particles were combined in a volumetric ratio based on approximating them as close-packed spheres at two scales. That is, small particles were supplied in a volume that would fill 77% (the close-packed fill fraction) of the close-packed void space left between the large particles supplied (approximated as 23% of the total). Though these approximations cannot represent an accurate space-filling model, the resulting scaffold structures demonstrate that they provide adequate guidance. In Figure 4.2, the electron micrograph of the scaffolds following salt leaching show that two pore size ranges are present and are highly interconnected. In addition to providing more surface area for MSC colonization, filling a majority of the interstitial space between the large salt grains with fine ones reduces the fraction of PLGA in the final foam. The finely structured thin walls visible in the micrograph are anticipated to shorten the degradation time after implantation[104].

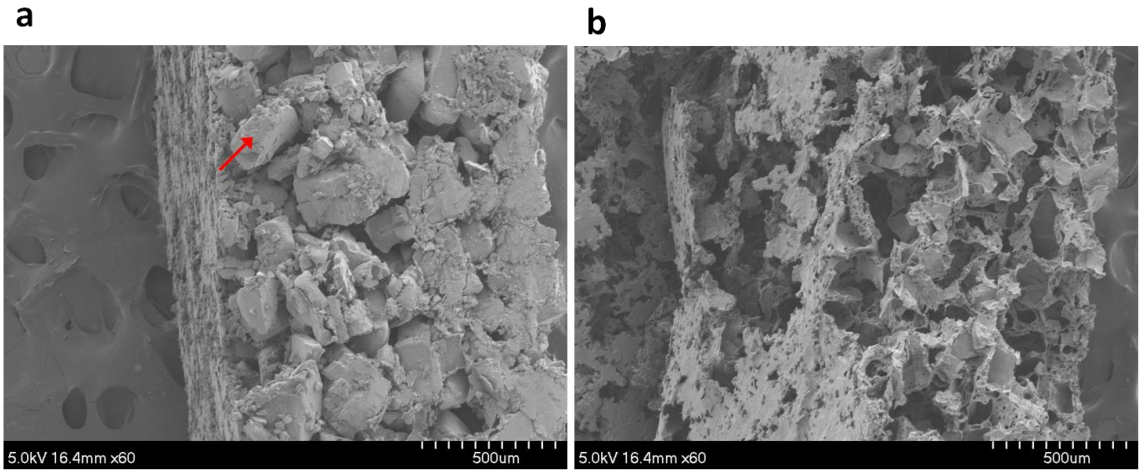

Figure 4.2: Scanning electron micrographs showing the structure of a PLGA sheet templated with a mixture of NaCl grains between 102-250 µm and less than 38 µm in size, (**a**) before and (**b**) after the aqueous extraction of the template. Arrow indicates a large salt template particle.

Templating our PLGA scaffolds with NaCl provided two additional benefits during the preparation of the complete construct. First, the presence of salt in the as-cast composite monolith gives it resistance to compression that allows it to be cut into small scaffolds while preserving the pore structure. A non-templated pore-forming method would require additional steps to achieve this, whereas we have prepared scaffolds approximately 1 mm in diameter by simply punching with a blunted and beveled 16-gauge needle (Figure 4.3). Furthermore, porosity in scaffolds prepared made molded directly to be this size would likely be dominated by edge effect. This potential for producing small scaffolds of a defined size is an important feature which will allow for the construction of implants that fit properly into surgically prepared defects in the joints of small animal models, the first stage in the development of a clinical treatment. Second, due to the aqueous extraction of

the template the entire surface area of the structure is hydrated prior to cell seeding. Once again, this simplifies manufacture by eliminating additional surface modification steps that would be required to overcome the surface tension in scaffolds where the hydrophobic PLGA surface interfaces with air in small pores. In our scaffolds the suspension of MSCs in Matrigel readily displaces the water already present in the pores.

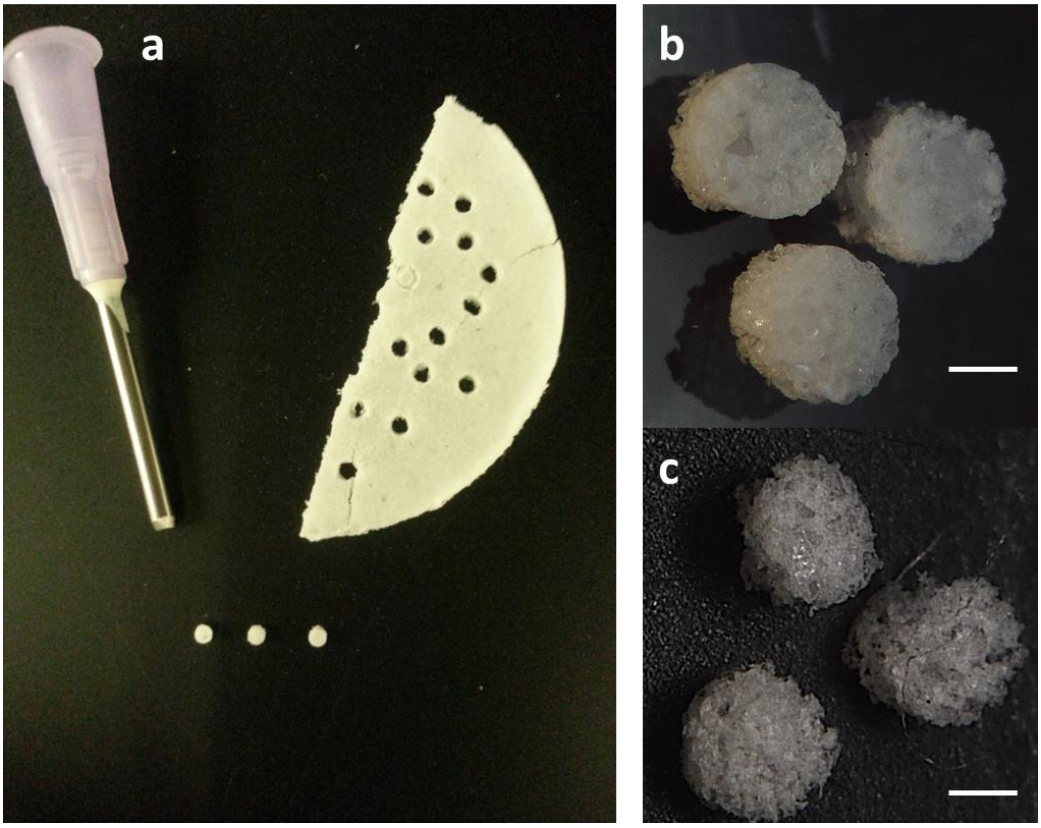

Figure 4.3: (**a**) Photograph of 1 mm PLGA circular scaffolds (bottom) fashioned from the cast composite sheet (right) using a blunted 27-gauge beveled into a punch tool (top). Optical images (high-depth of field Hirox microscope) of 1 mm PLGA circular scaffolds (**b**) before and (**c**) after NaCl template leaching. Scale bars are 300 µm.

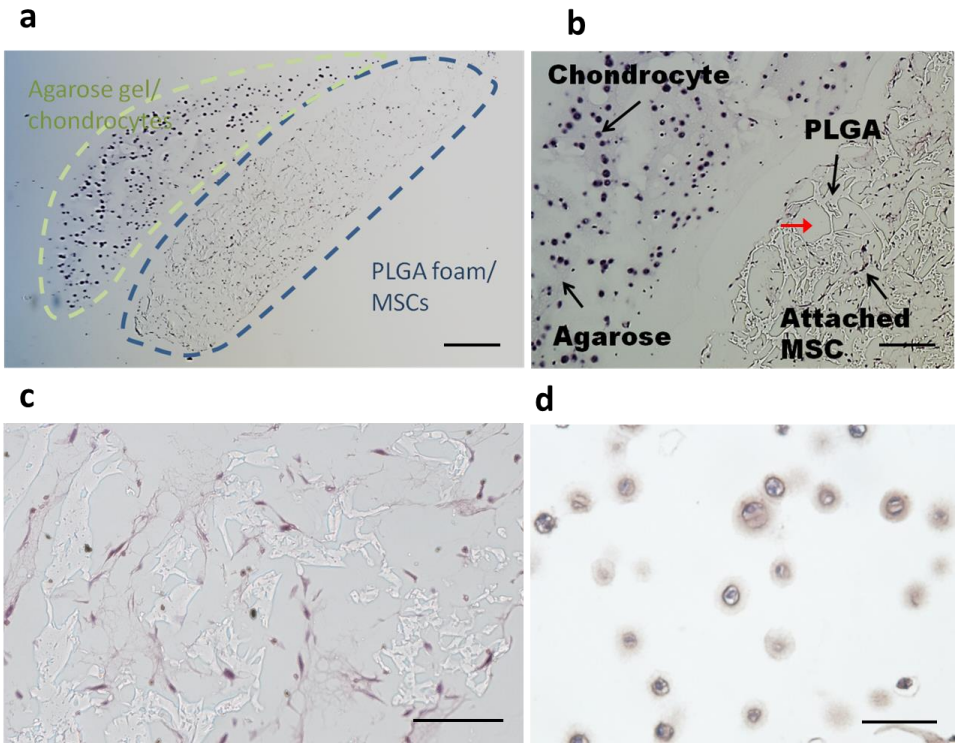

Figure 4.4: Histological staining of the biphasic bioartificial cartilage construct after 2 weeks in culture. H&E staining is shown at (**a**) 5x, **(b**) 20x and (c) 40x magnification (red arrow indicates a large templated pore preserved after extended culture at 37°C). (**d**) Immunohistochemical staining for collagen type II is shown at 40x, where positive domains are visible around chondrocytes. Scale bars are 500 µm, 200 µm, 30 µm, and 20 µm.

Complete biphasic constructs produce promising results. Constructs were well-integrated after formation and could be manipulated easily in culture. Figure 4.4a-c shows the resulting tissue construct following fixation, sectioning and H&E staining. The PLGA foam scaffold is seen to retain its structure indicating the good mechanical stability during prolonged culture at physiological temperature. Additionally, the MSCs are found to have colonized a large portion of the smaller pores demonstrating the interconnectivity achieved between scaffold pores. MSC

also appear to be attached and are estimated to have proliferated substantially based on seeding density. While the ultimate success of this scaffold to support MSC chondrogenic signaling remains unproven, these results appear encouraging. The chondrocytes embedded in agarose have also proliferated and have produced significant domains of ECM containing collagen type II, the major protein constituent of cartilage (Figure 4.4d). By inspection this response is similar to control constructs formed without MSCs and more detailed analysis is needed to fully assess the effects of biphasic co-culture in future studies.

Chapter 4.3.2. Alginate-Templated Lung Organoids

Our conception of an alginate-templated lung organoid was inspired by latex-templated inverse opals of inorganic solids[167]. As seen in Figure 4.5, these open porous structures bear a strong resemblance to lung tissue, but in our adaptation latex is replaced by biocompatible alginate beads and the inverse-opal-like structure is formed by the growth of lung tissue around the beads. We were able to produce alginate beads in the size range that matched the alveolar cavities that they would template by manipulating the voltage and geometry of a custom electrostatic extrusion apparatus (Figure 4.6). Alginate beads can be dissolved by chelating the calcium ions and sodium citrate offers a potential means of accomplishing this *in situ* with a

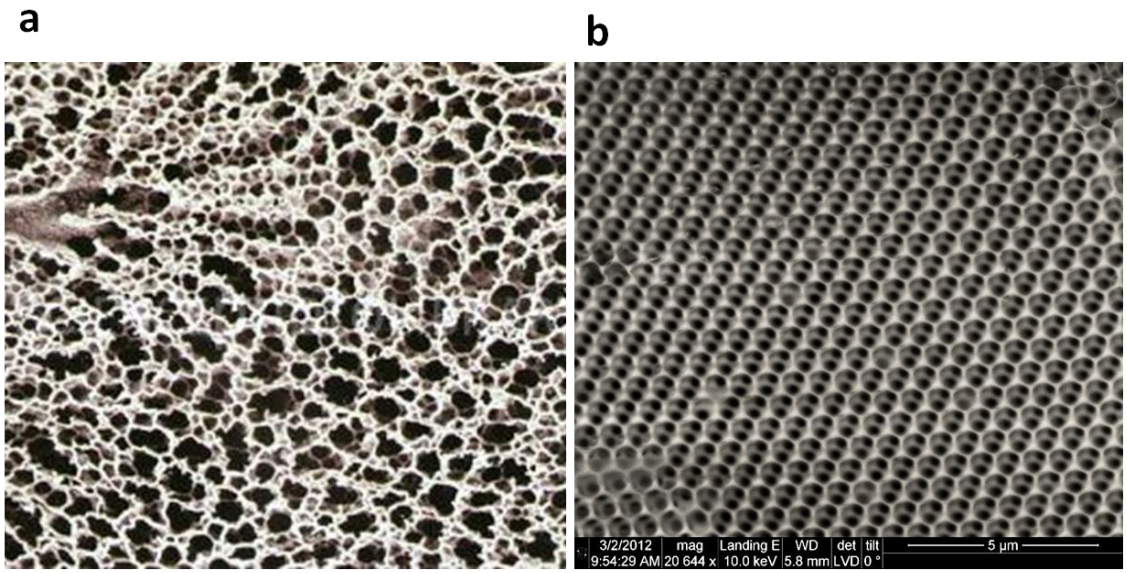

Figure 4.5: Scanning electron micrographs showing the similar structures apparent in the (**a**) lung tissue[168] and (**b**) an inverse opal prepared by templating cerium oxide with polystyrene latex. Cerium oxide synthesis and imaging perform by Danielle Casillas.

limited impact on cells in culture. To first prove the feasibility of dissolving the templating beads with citrate while not disrupting cell adhesions we simultaneously measured the effects tittered citrate concentrations in media on adhered lung fibroblasts and alginate beads (Table 4.1). These results showed that 10 mM sodium citrate was able to dissolve large alginate beads in an acceptable time frame, while showing no negative effects on the attached culture of fibroblasts. In our first straightforward attempts at forming a construct, cells were seeded directly on the surface of alginate microbeads that were packed into a culture dish. However, these preliminary experiments determined that native calcium alginate surfaces, in the form of a sheet or microbead, could not support the attachment and growth of lung

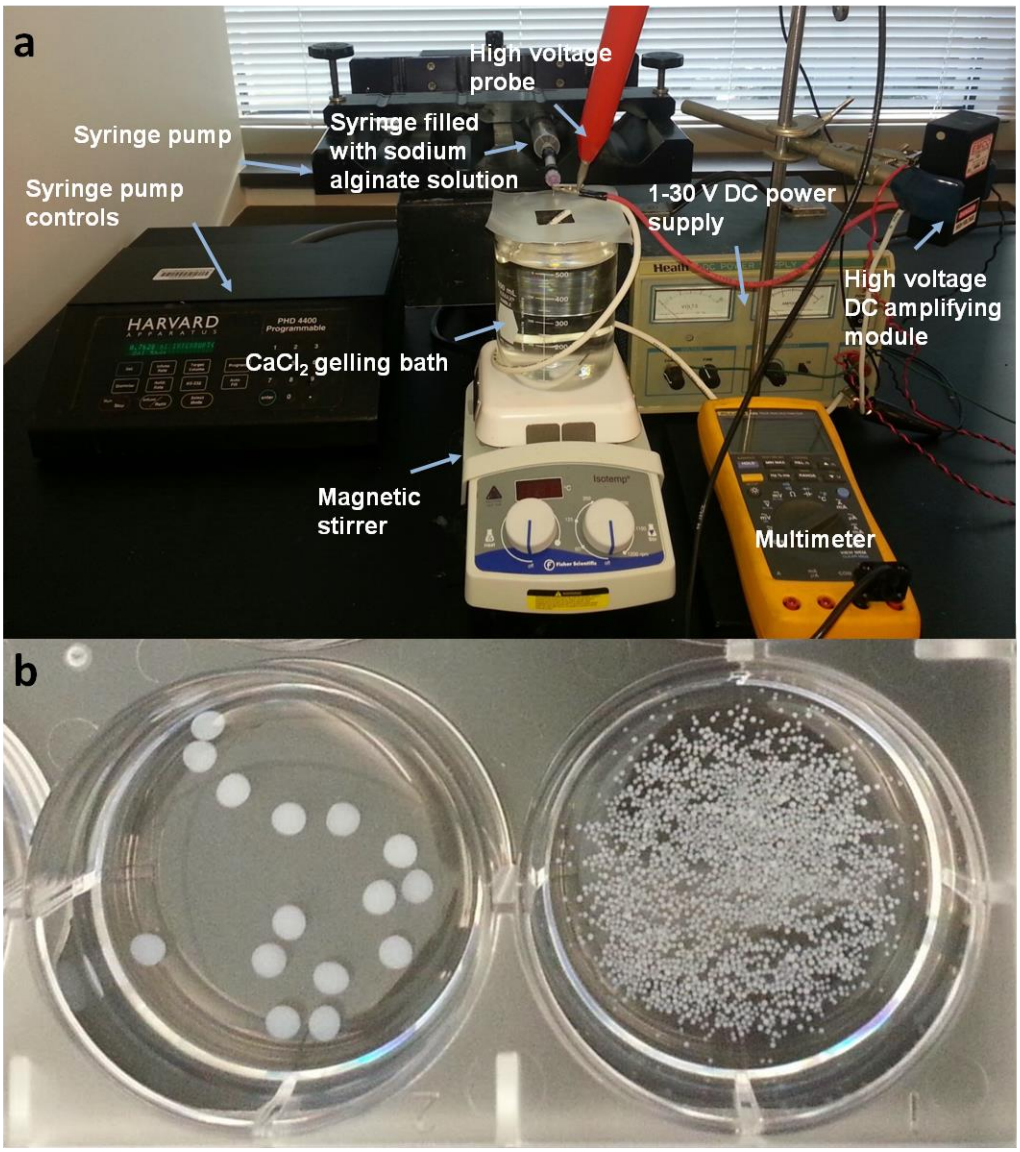

Figure 4.6: (**a**) Photograph of the electrostatic alginate bead generating apparatus. Alginate beads can be produced with this apparatus in a range of sizes (**b**). Beads produced with no applied voltage (left) are ~3 mm in diameter, while those produce under a 6kV potential drop (right) are ~ 300 µm in diameter, shown here in the well of a 6-well plate.

fibroblasts, the most adherent of the cell types needed to reconstitute the lung. In an effort to overcome the poor cell attachment on alginate we employed a chemical modification of the polymer chains with the integrin-binding peptide RGD. While the attachment of fibroblast to the planar alginate gel improved somewhat, we still did not observe cells growing attached to the surface of the alginate beads. We concluded that the effects of gravity caused the cells to roll off of the beads and settle before the attachment could take place.

Sodium Citrate Concentration	0.1 mM	1 mM	10 mM	100 mM
Alginate Bead Result	Not dissolved @24 hrs	Not dissolved @24 hrs	Dissolved @ 8 hrs	Dissolved @ 2 hrs
Attached Fibroblast Result	Unchanged @ 24 hrs	Unchanged @ 24 hrs	Unchanged @ 24 hrs	Detached and assumed spherical conformation @ 1.5 hrs

Table 4.1: Results from simultaneous treatment of attached iPSC-derived fibroblasts and alginate beads with sodium citrate of various concentrations

Our revised design incorporated a second gel phase to suspend the cells and allow them to grow into a 3D tissue structure around the alginate beads. There have been numerous advances in the 3D suspended culture of cells (see Chapter 1.3). This progress has been such that we were able to find a suitable material among several options sold commercially. Our criteria for the gel phase material were that it, 1) undergo gelation in a way that is not harmful to cells and allows for integration with alginate beads; 2) permit the proliferation and migration of cells necessary to form a tissue; 3) be compatible with long-term cell culture and not pose concerns

for eventual implantation in human patients. We elected to use a product produced by Cellendes (Figure 4.7). The 3-D Life Dextran-CD Hydrogel system is based on the chemical crosslinking of modified dextran linear polymer chains under mild conditions tolerated well by mammalian cells[111]. The dextran backbone of the gel introduces a highly bioinert substrate that can be easily processed if present after

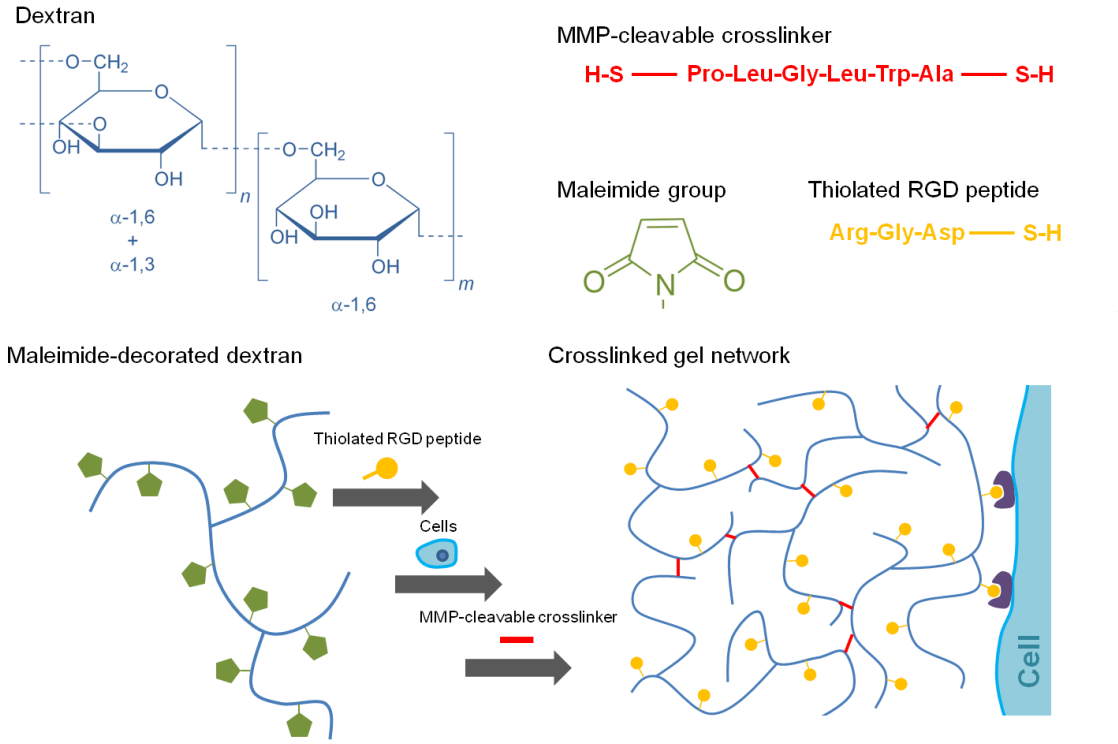

Figure 4.7: Schematic outline of the gelation process of the Cellendes CD-link 3-D Life Hydrogel for the 3-D culture of cells.

implantation[110–112]. The primary chains are decorated with maleimide groups that react rapidly with thiols in aqueous solution to form stable thioether linkages. Gelation is achieved by combining these chains with homobifunctional thiol crosslinking molecules in solution. When the reaction is performed at neutral pH or below the reaction is highly specific since amines will be protonated and unreactive towards the maleimides. This allows the gel to be formed after the addition of cells without harming them. However, preserving reaction conditions that were mild to cells was necessarily balanced in Cellendes' methods against the need to allow time for uniform mixing. To slow the kinetics the reaction buffer was supplied at pH 5.5, where thiols are partially protonated. Since the complete gelation still takes less than 5 minutes, cells can be encapsulated without undue stress. In our experiments it was necessary to extend the mixing time further to adequately coat the alginate beads. Since further reduction in the pH could be potentially harmful, reduced reaction kinetics were achieved effectively by performing the reaction on a bed of ice with all chilled components. The maleimide functionality also permits the tethering of the RGD peptides onto the gel network allowing the cells to attach and apply tension to the gel, and thus the potential to migrate. Migration, and especially proliferation, also requires the disruption of the gel network, which has pores too small for cells to pass through. This is facilitated be the inclusion of a matrix metalloprotease (MMP) cleavable peptide in the bi-thiol crosslinker. Cells will express the MMPs in response to the environment and produce the additional space needed for migration and growth, eventually degrading most of the network[169].

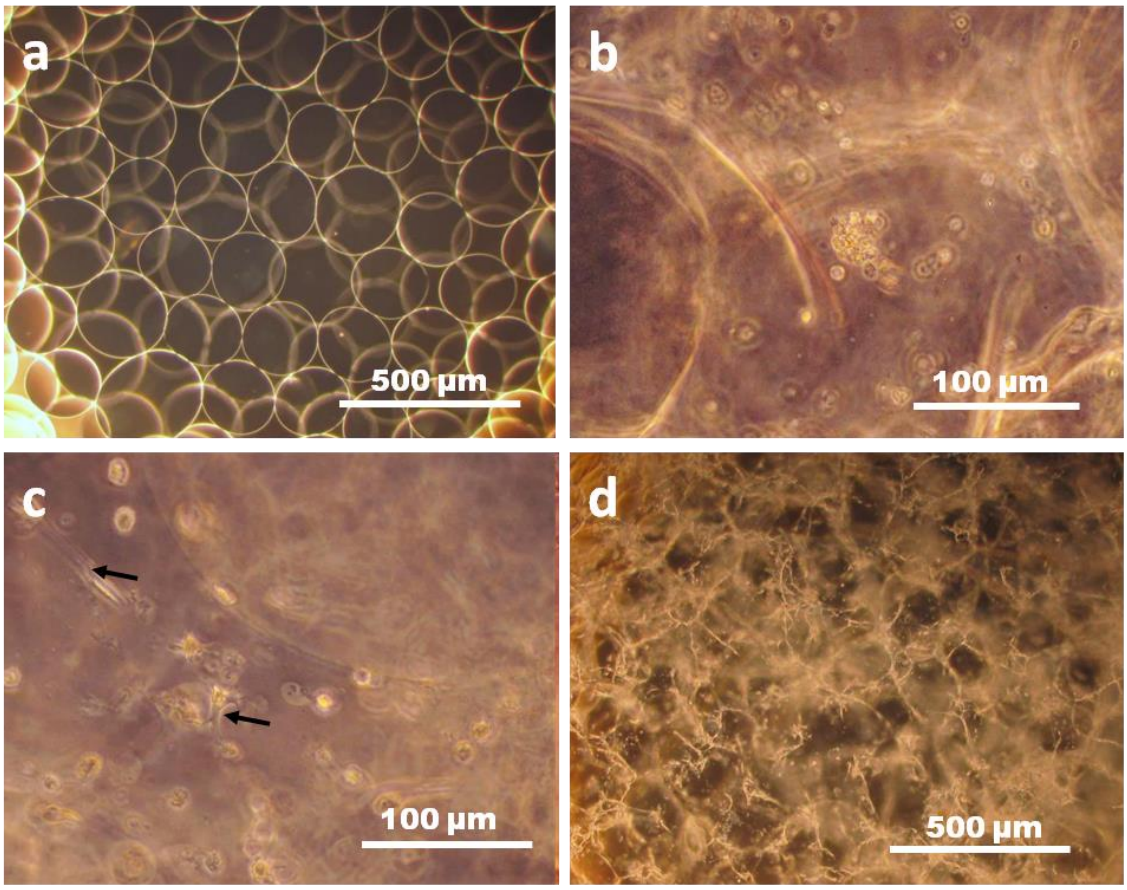

Figure 4.8: Images showing early progress of alginate template lung organoids. (**a**) Alginate beads are seeded with iPSC-derived lung fibroblasts (**b**), which remain suspended upon gelation. (**c**) After 2 days in culture the cells can be observed to extend processes (arrows) indicating they are spreading in the gel, and (**d**) after 7 days in culture a fibrotic nextwork of cells has begun to form.

We have found that iPSC-derived lung fibroblasts remain suspended in the dextran gel and begin to spread after 1 or 2 days in culture (Figure 4.8). After 1 week, brightfield microscopy shows that the cells have proliferated significantly, have taken on pronounced elongated morphology in the gel phase, and have begun to form a network around the beads. The ability of orgnoids to reach this stage of growth has been observed to depend on the state of the alginate beads at the time of

cell seeding. Constructing organoids with alginate beads that have been pre-equilibrated with cell culture media produces more rapid, consistent, and sustained cell spreading and growth than using beads washed in deionized water only. Organoids grown to 2 weeks in culture become difficult to assess by brightfield microscopy due to the dense fibrotic network that has been produced. Staining these constructs with the live cell fluorescent dye Calcein and imaging by scanning

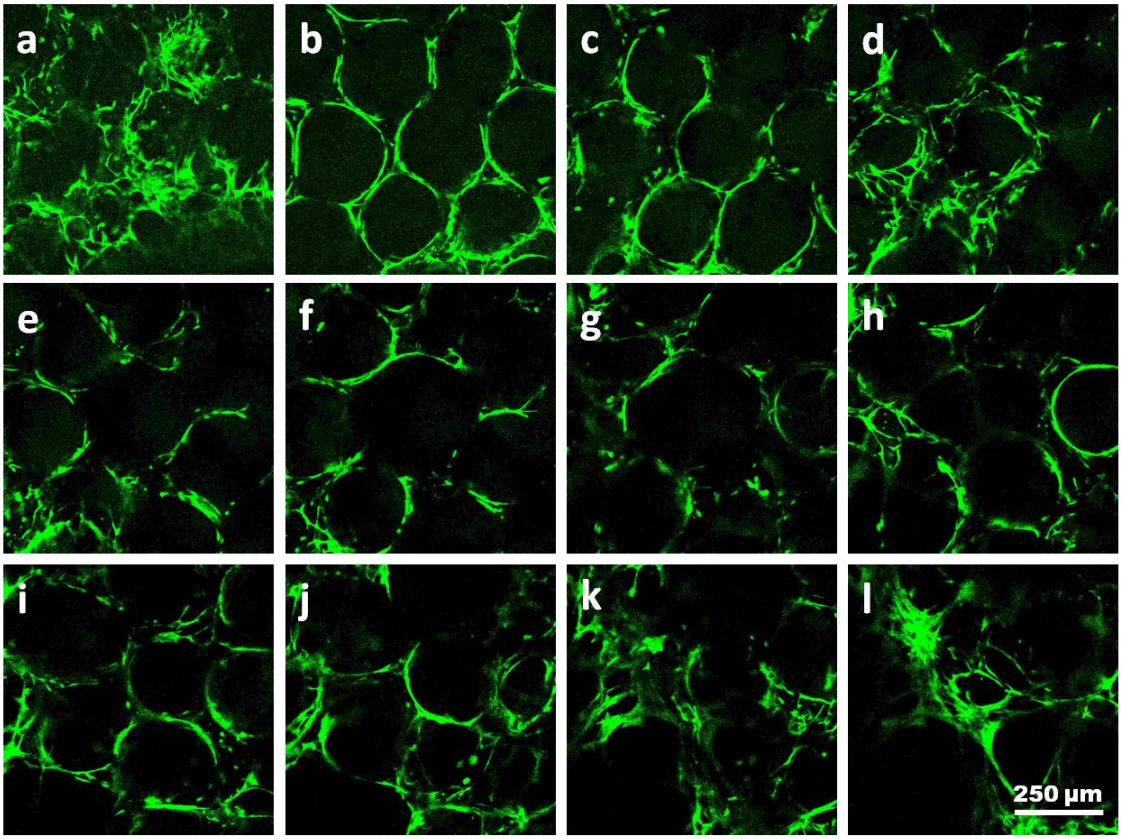

Figure 4.9: Series of confocal optical sections obtained (**a-l**) at 100 µm intervals, from an alginate-templated lung organoid stained with the live cell fluorescent marker Calcein after 14 days in culture.

confocal fluorescence microscopy reveals the cell structure in 3-D (Figure 4.9). Fibroblasts have spread throughout the interstitial space between the beads. The open fibrotic network extends through all of the three layers of beads that make up the over 1 mm thickness of the organoid. These results indicate that the cells remain well-suspended in the gel phase even after extended periods in culture, and that they are able to actively degrade the MMP-cleavable crosslinks to proliferate and from a network.

Chapter 4.4. Summary

Creating the appropriate structural features required for biological function represents a critical element in the development of successful tissue engineering strategies. In natural tissues the presence of pores often provides the necessary physical environment for both the cellular and extracellular processes that must be maintained. Following nature's lead, we have used templating to tailor a porous structure in two separate tissue engineering projects. Using milled NaCl as the template, we have produced a hierarchical porous structure in a PLGA scaffold as part of a biphasic bioartificial cartilage construct. Having both small and large pores simultaneously provides a large capacity for MSC colonization and an open structure for the transport of signals supplied by the MSCs to chondrocytes segregated within a separate gel phase. We have demonstrated that these PLGA scaffolds function well as a synthetic niche for MSCs, which occupy the small pores and proliferate. This represents an important first step towards the creation of transplantable bioartificial cartilage. The highly adaptable salt templating method

we have employed sets the stage for optimizing this system for cartilage matrix production, which can be done, in part, using the methods detailed in Chapter 1. To develop a lung tissue organoid we needed a templating agent that could dictate the structure of tissue directly, without a scaffold acting as an intermediate. This template must then be removed without harming the living organoid. We have completed proof-of-principle experiments demonstrating that alginate can be formed into beads by high-voltage electrostatic generation that can template the growth of iPSC-derived fibroblasts into an inverse-opal like structure. The alginate can later be dissolved with sodium citrate which does not disrupt cell attachment. This work is also preliminary, but shows that alginate templating offers a viable route to producing artificial lung tissue *in vitro*, something that has never been done.

Chapter 5. Conclusions

The central topic of this dissertation has been the development of tools that can aid in the effort to bring regenerative medicine out from the research laboratory and into the clinic. The original research described in Chapters 2, 3, and 4 has been directed at three different problems in regenerative medicine. In each case, the work presented here represents an important early step in the development of a new tool to address these problems.

Chapter 2 reported our work to produce a multivariate tool for Raman-based diagnosis of pathological articular cartilage matrix. We have shown that recognition of diseased cartilage matrix is possible by using a pair of model materials, one healthy and one pathological, to create a metric by which to score the Raman spectra from cartilage samples. Additionally, we hypothesized that the combination of multiple metrics derived from different sets of materials could further improve classification of healthy and diseased cartilage spectra. The three metrics we produced by this method were found to afford varying degrees of accuracy in classification of spectra from normal and osteoarthritic cartilage. The metric derived from human tissues misclassified 4.1% of 7656 healthy and osteoarthritic map spectra. The metric derived from rat tissues misclassified 2.7% and the metric derived from collagens misclassified 14.7%. The optimized combination of these metrics resulted in a greater than 4-fold reduction in the misclassification rate (0.65%) over the most accurate single metric. These results indicate that the use of

diverse metrics can improve the accuracy in future developments of Raman diagnostics. The principal application of this tool is the clinical diagnosis of osteoarthritis and other cartilage diseases, but like many useful tools this one might find use outside of the task for which it was designed. The ability to detect unanticipated variation in the matrix of tissue engineered cartilage constructs might prove especially useful. Given the typically long time to go from laboratory demonstration to implementation of a new clinical diagnostic, applications of this method in regenerative medicine may in reality be the most immediate.

In Chapter 3 a new method of studying hPSCs in confined colonies was described. Here we sought to provide a tool to improve understanding of the spatial heterogeneity of the pluripotent state in hPSC colonies. This variation has been noted before, but the approach described here offers a more carefully controlled measurement to give a more complete picture. We created 3-D reconstructions of pattern-standardized hPCS colonies the by using an automated analysis of confocal z-stack images. This provided unique spatial information about individual cells in the colonies. This includes the volumetric distribution of cells and the morphology of nuclei and entire colonies. In addition, we have mapped the spatial variation in the IF-measured single-cell expression levels of several proteins localized to the nucleus. In our experiments, expression of the pluripotency transcription factor OCT-4 and three early differentiation markers were observed to be a function of radial location, which varied with colony thickness. Implemented in larger study, this method will be able to give a better understanding of how pluripotency and

differentiation potential vary within hPSC colonies. In addition, further investigations using this method could also provide important guidance for deployment of colony patterning in scaled-up hPSC culture. Given our observation of a strong thickness dependency of pluripotency markers, careful control of cell seeding and proliferation may be critical in such efforts.

Two distinct projects utilizing template-structuring in tissue engineered constructs were described in Chapter 4. In a neocartilage construct, a PLGA scaffold with hierarchical structure was templated with NaCl. These porous foams functioned as mechanical reinforcement and a niche for the MSCs that supported cartilage producing chondrocytes. We have created a lung organoid, which demonstrates the ability to template the structure of interconnecting alveoli using alginate beads. Alginate can be dissolved in culture without harming cells so that the final templated structure is composed only of cellular tissue. While both of these results are only the early stages of large undertakings, they also both have established important core elements for future developments. The versatile nature of the straightforward methods used to prepare the PLGA foams lends itself to refining modifications to the structure or functionalization of the foams. The use of alginate to template lung structure is an innovative approach that might prove to be an important advantage for achieving this very challenging goal.

Collectively, the research presented in this dissertation has made important progress in the early development of several new tools that could impact the field of regenerative medicine. Realizing the clinical goals of regenerative medicine will

certainly require new technology and could be accelerated by the future use of these tools.

Chapter 6. Future Work

The three research areas described in this dissertation each represent early demonstrations of new biomedical tools. Thus, there is a great deal yet to be done to deliver on the promise of each tool. This Chapter will detail some immediate steps that can be taken to advance these efforts.

The full development of a medical Raman diagnostic that can detect early signs of cartilage disease in pre-clinical patients will require improved training data. Our research has shown that the multivariate comparison of pathological and healthy samples can create sensitivity diagnosis. Obtaining Raman spectra from patients with pre-clinical OA should then be a long term goal. Additionally, our results indicate a synergistic advantage in using multiple metrics. Given the wide accessibility of micro-fracture surgery patients and the similarity to the rat injury model we studied, obtaining spectra from this source may also be a valuable avenue to pursue. In the short term, the over-all method should be adapted to an arthroscopic study in small animals. Testing various disease models in this way could provide further validation of our approach. Additionally, the ability of this method to examine cartilage matrix should be employed as a non-destructive experimental feedback tool in the continuation of the neocartilage project described in Chapter 4.

There are several ways in which our confocal analysis of patterned hPSC colonies could be improved by continuation of the research presented here. The time consuming nature of imaging could be mitigated by once again taking

advantage of the regular nature of patterned colonies. The periodic spacing and uniform size of the μCP confined colonies makes automated imaging of an entire culture dish a possibility. While the system must be carefully calibrated and flatness of custom culture dished improved, this is a realistic immediate goal. Addressing the limitation imposed by the reliance of different fluorescent dyes is more difficult. A different method of imaging expression of more molecular targets simultaneously might be found in Raman. SERs particles can be targeted immumochemically by tethering antibodies[170]. Importantly this method offers outstanding multiplexing capability because SERs tags can be impregnated with different Raman tags with highly distinctive spectra that can be separated from one another in a single acquisition. A temporal element might also be added to the spatial analysis produced so far. The method thus far has required that cultures be fixed before imaging, limiting the time variable to widely spaced intervals when separate wells could be fixed. Analysis of live cell imaging could provide a nearly continuous spatial-temporal picture of variation within colonies. Transgenic cell lines expressing fluorescent proteins would allow live cell imaging, but would further limit the number of targets that could be observed. Instead, several particle based probes can be used to perform live cell imaging, including fluorescent nanodiamonds and gold SERs particles[170,171].

Our method of forming neocartilage has been demonstrated to produce viable constructs. The next step is to refine the design to optimize for cartilage matrix production. Possible refinements include varying the pore sizes or making

them more regular with water-soluble microsphere templates[172]. Additionally, The PLGA foam could be functionalized[85] or impregnated for the controlled release of bioactive compounds[106,108,173]. Beyond the materials aspects of this project, the ideal culture conditions must be studied and developed. The constructs might be designed into a bioreactor system[174,175] that could supply mechanical forces, as well as different media to the two phases.

The development of a functional lung tissue will require a great deal of further work. The most immediate effort should focus on creating a more complete combination of cell types in the organoid. In addition to fibroblasts, lung endothelial progenitors will be needed to develop vascularization, and lung epithelial progenitors will eventually become the type 1 and type 2 cells that allow gas exchange to take place[137]. How to direct these cells to form the appropriate structures is not clear. Removing the dextran gel in developed fibroblast organoids like the ones we have made might provide space for the infiltration of endothelial cells. We might also encapsulate the endothelial cells in micro-tubes of another gel material to direct vascularization[124]. Epithelial cells might be seeded after alginate removal to direct them to their appropriate location at the eventual gas interface. In summary, the work presented here represents important early steps in the process of making several useful tools for regenerative medicine.

References:

1. Thomson J a. Embryonic Stem Cell Lines Derived from Human Blastocysts. *Science (80-.).* 1998;282(5391):1145–1147. Available at: http://www.sciencemag.org/cgi/doi/10.1126/science.282.5391.1145. Accessed October 5, 2012.

2. Takahashi K, Tanabe K, Ohnuki M, et al. Induction of pluripotent stem cells from adult human fibroblasts by defined factors. *Cell*. 2007;131(5):861–72. Available at: http://www.ncbi.nlm.nih.gov/pubmed/18035408. Accessed October 5, 2012.

3. Lowry WE, Richter L, Yachechko R, et al. Generation of human induced pluripotent stem cells from dermal fibroblasts. *Proc. Natl. Acad. Sci. U. S. A.* 2008;105(8):2883–8. Available at: http://www.pubmedcentral.nih.gov/articlerender.fcgi?artid=2268554&tool=pmcentrez&rendertype=abstract.

4. Hochedlinger K, Jaenisch R. Nuclear reprogramming and pluripotency. *Nature*. 2006;441(7097):1061–7. Available at: http://www.ncbi.nlm.nih.gov/pubmed/16810240. Accessed October 18, 2012.

5. Goldring CEP, Duffy P a, Benvenisty N, et al. Assessing the safety of stem cell therapeutics. *Cell Stem Cell*. 2011;8(6):618–28. Available at: http://www.ncbi.nlm.nih.gov/pubmed/21624806. Accessed October 18, 2012.

6. Tang C, Lee AS, Volkmer J-P, et al. An antibody against SSEA-5 glycan on human pluripotent stem cells enables removal of teratoma-forming cells. *Nat. Biotechnol.* 2011;29(9):829–34. Available at: http://www.ncbi.nlm.nih.gov/pubmed/21841799. Accessed October 18, 2012.

7. Puri MC, Nagy A. Concise review: Embryonic stem cells versus induced pluripotent stem cells: the game is on. *Stem Cells*. 2012;30(1):10–4.

8. Bilic J, Izpisua Belmonte JC. Concise review: Induced pluripotent stem cells versus embryonic stem cells: close enough or yet too far apart? *Stem Cells*. 2012;30(1):33–41.

9. Melkoumian Z, Weber JL, Weber DM, et al. Synthetic peptide-acrylate surfaces for long-term self-renewal and cardiomyocyte differentiation of human embryonic stem cells. *Nat. Biotechnol.* 2010;(May). Available at: http://www.ncbi.nlm.nih.gov/pubmed/20512120.

10. Axelrod BW, Wion D. Stem Cells and Cancer Stem Cells, Volume 8. Hayat MA, ed. 2012;8:3–12.

11. Saha K, Mei Y, Reisterer CM, et al. Surface-engineered substrates for improved human pluripotent stem cell culture under fully defined conditions. *Proc. Natl. Acad. Sci. U. S. A.* 2011;108(46):18714–9.

12. Raman C. A new radiation. *Indian J. Phys.* 1928;398(March). Available at: http://repository.ias.ac.in/70648/1/36-PUb.pdf. Accessed November 20, 2013.

13. Noguchi N, Abduriyim A, Shimizu I, Kamegata N, Odake S, Kagi H. Imaging of internal stress around a mineral inclusion in a sapphire crystal: application of micro-Raman and photoluminescence spectroscopy. *J. Raman Spectrosc.* 2013;44(1):147–154. Available at: http://doi.wiley.com/10.1002/jrs.4161. Accessed November 20, 2013.

14. Maher RC, Cohen LF, Lohsoontorn P, Brett DJL, Brandon NP. Raman spectroscopy as a probe of temperature and oxidation state for gadolinium-doped ceria used in solid oxide fuel cells. *J. Phys. Chem. A*. 2008;112(7):1497–501. Available at: http://www.ncbi.nlm.nih.gov/pubmed/18225868.

15. Bonifacio A, Sergo V. Vibrational Spectroscopy Effects of sample orientation in Raman microspectroscopy of collagen fibers and their impact on the interpretation of the amide III band. *Vib. Spectrosc.* 2010;53(2):314–317. Available at: http://dx.doi.org/10.1016/j.vibspec.2010.04.004.

16. Tanaka M, Young RJ. Review Polarised Raman spectroscopy for the study of molecular orientation distributions in polymers. *J. Mater. Sci.* 2006;41(3):963–991. Available at: http://link.springer.com/10.1007/s10853-006-6595-7. Accessed November 14, 2013.

17. Kramberger C, Thurakitseree T, Shiozawa H, et al. Length scales in orientational order of vertically aligned single walled carbon nanotubes. *Phys. Status Solidi*. 2013;4:n/a–n/a. Available at: http://doi.wiley.com/10.1002/pssb.201300095. Accessed November 20, 2013.

18. Aroca R. *Surface-Enhanced Vibrational Spectroscopy*. Chichester, UK: John Wiley & Sons, Ltd; 2006. Available at: http://doi.wiley.com/10.1002/9780470035641. Accessed November 20, 2013.

19. Wächtler M, Guthmuller J, González L, Dietzek B. Analysis and characterization of coordination compounds by resonance Raman spectroscopy. *Coord. Chem. Rev.* 2012;256(15-16):1479–1508. Available at:

http://linkinghub.elsevier.com/retrieve/pii/S0010854512000240. Accessed November 20, 2013.

20. Heinegård D, Saxne T. The role of the cartilage matrix in osteoarthritis. *Nat. Rev. Rheumatol.* 2011;7(1):50–6. Available at: http://www.ncbi.nlm.nih.gov/pubmed/21119607. Accessed October 12, 2012.

21. Freedman M, Hootman J, Helmick C. Projected state-specific increases in self-reported doctor-diagnosed arthritis and arthritis-attributable activity limitations—United States, 2005-2030. *MMWR Morb Mortal Wkly Rep*. 2007;56(17). Available at: http://scholar.google.com/scholar?hl=en&btnG=Search&q=intitle:Projected+state-specific+increases+in+self-reported+doctor-diagnosed+arthritis+and+arthritis-attributable+activity+limitations—United+States,+2005–2030.#0. Accessed September 6, 2013.

22. Lee AS, Ellman MB, Yan D, et al. A current review of molecular mechanisms regarding osteoarthritis and pain. *Gene*. 2013;527(2):440–7. Available at: http://www.ncbi.nlm.nih.gov/pubmed/23830938. Accessed August 19, 2013.

23. Valdes AM, Spector TD. Genetic epidemiology of hip and knee osteoarthritis. *Nat. Rev. Rheumatol.* 2011;7(1):23–32. Available at: http://www.ncbi.nlm.nih.gov/pubmed/21079645. Accessed November 6, 2013.

24. Moskowitz RW. *Osteoarthritis: diagnosis and medical/surgical management*. Lippincott Williams & Wilkins; 2007.

25. Potter K, Butler JJ, Horton WE, Spencer RG. Response of engineered cartilage tissue to biochemical agents as studied by proton magnetic resonance microscopy. *Arthritis Rheum.* 2000;43(7):1580–90. Available at: http://www.ncbi.nlm.nih.gov/pubmed/10902763.

26. Toh WS, Yang Z, Liu H, Heng BC, Lee EH, Cao T. Effects of culture conditions and bone morphogenetic protein 2 on extent of chondrogenesis from human embryonic stem cells. *Stem Cells*. 2007;25(4):950–60. Available at: http://www.ncbi.nlm.nih.gov/pubmed/17218402. Accessed October 19, 2012.

27. Hwang NS, Kim MS, Sampattavanich S, Baek JH, Zhang Z, Elisseeff J. Effects of three-dimensional culture and growth factors on the chondrogenic differentiation of murine embryonic stem cells. *Stem Cells*. 2006;24(2):284–91.

28. Thompson Y, Piez KA, Seyedin SM. in Agarose Gel Culture differentiation [l-3]. In studies on cartilage induction and differentiation , intra- shown to evoke the formation of hyaline cartilage and bone [4 , 51 . Extraction of ate and form cartilage and bone has been the subject of inte. *Exp. Cell Res.* 1985;157:483–494.

29. Tchetina E V, Kobayashi M, Yasuda T, Meijers T, Pidoux I, Poole a R. Chondrocyte hypertrophy can be induced by a cryptic sequence of type II collagen and is accompanied by the induction of MMP-13 and collagenase activity: implications for development and arthritis. *Matrix Biol.* 2007;26(4):247–58. Available at: http://www.ncbi.nlm.nih.gov/pubmed/17306969. Accessed October 19, 2012.

30. Attur M, Krasnokutsky-Samuels S. Prognostic biomarkers in osteoarthritis. *Curr. Opin. ….* 2013;25(1):136–144. Available at: http://scholar.google.com/scholar?hl=en&btnG=Search&q=intitle:Prognostic+biomarkers+in+osteoarthritis#0. Accessed October 7, 2013.

31. Esmonde-white KA, Esmonde-white FWL, Morris D, Roessler BJ. Fiber-optic Raman spectroscopy of joint tissues. 2011:1675–1685.

32. Ellis DI, Cowcher DP, Ashton L, O'Hagan S, Goodacre R. Illuminating disease and enlightening biomedicine: Raman spectroscopy as a diagnostic tool. *Analyst*. 2013;138(14):3871–84. Available at: http://www.ncbi.nlm.nih.gov/pubmed/23722248. Accessed September 24, 2013.

33. Haka AS, Gardecki JA, Nazemi J, Fitzmaurice M, Feld MS. Diagnosing breast cancer using Raman spectroscopy : prospective analysis. 2013;14(October 2009):1–8.

34. Krafft C, Sergo V. Biomedical applications of Raman and infrared spectroscopy to diagnose tissues. 2006;20:195–218.

35. Konorov SO, Schulze HG, Piret JM, Blades MW, Turner RFB. Label-free determination of the cell cycle phase in human embryonic stem cells by Raman microspectroscopy. *Anal. Chem.* 2013;85(19):8996–9002. Available at: http://www.ncbi.nlm.nih.gov/pubmed/23968373.

36. Chan JW, Lieu DK. Label-free biochemical characterization of stem cells using vibrational spectroscopy. *J. Biophotonics*. 2009;2(11):656–68. Available at: http://www.ncbi.nlm.nih.gov/pubmed/19653219. Accessed February 26, 2011.

37. Lin D, Feng S, Pan J, et al. Colorectal cancer detection by gold nanoparticle based surface-enhanced Raman spectroscopy of blood serum and statistical analysis. *Opt. Express*. 2011;19(14):13565–77. Available at: http://www.ncbi.nlm.nih.gov/pubmed/21747512.

38. Matousek P, Stone N. Prospects for the diagnosis of breast cancer by noninvasive probing of calcifications using transmission Raman spectroscopy. 2013;12(April 2007):1–8.

39. Mc E, Santos LF, Caspers PJ, Schut TCB, Hollander JC Den, Puppels GJ. Discriminating basal cell carcinoma from perilesional skin using high wave-number Raman spectroscopy. 2013;12(June 2007):1–7.

40. Shafer-Peltier KE, Haka AS, Fitzmaurice M, et al. Raman microspectroscopic model of human breast tissue: implications for breast cancer diagnosisin vivo. *J. Raman Spectrosc.* 2002;33(7):552–563. Available at: http://doi.wiley.com/10.1002/jrs.877. Accessed August 30, 2013.

41. Haka AS, Fitzmaurice M, Crowe J, Dasari RR, Feld MS. Detecting Breast Cancer Using Raman Spectroscopy C ell cytoplasm C ell nucleus C alcium hydroxyapatite. 2002:349–351.

42. Schut TCB, Caspers PJ, Nijssen A, Koljenovic S. Towards oncological application of Raman spectroscopy. 2009;36(1):29–36.

43. Granger JH, Granger MC, Firpo M a, Mulvihill SJ, Porter MD. Toward development of a surface-enhanced Raman scattering (SERS)-based cancer diagnostic immunoassay panel. *Analyst*. 2013;138(2):410–6. Available at: http://www.ncbi.nlm.nih.gov/pubmed/23150876. Accessed November 20, 2013.

44. Bonifacio A, Beleites C, Vittur F, et al. Chemical imaging of articular cartilage sections with Raman mapping, employing uni- and multi-variate methods for data analysis. *Analyst*. 2010;135(12):3193–204. Available at: http://www.ncbi.nlm.nih.gov/pubmed/20967391. Accessed October 7, 2011.

45. Sheng N, Lim J, Hamed Z, Yeow H, Chan C, Huang Z. Early detection of biomolecular changes in disrupted porcine cartilage using polarized Raman spectroscopy. 2011;16(January):1–10.

46. Pudlas M, Brauchle E, Klein TJ, Hutmacher DW, Schenke-Layland K. Non-invasive identification of proteoglycans and chondrocyte differentiation state by Raman microspectroscopy. *J. Biophotonics*. 2013;6(2):205–11. Available at: http://www.ncbi.nlm.nih.gov/pubmed/22678997. Accessed October 4, 2013.

47. Esmonde-white KA, Mandair GS, Raaii F, et al. Raman spectroscopy of synovial fluid as a tool for diagnosing osteoarthritis. *J. ….* 2009;14(3):1–17. Available at: http://biomedicaloptics.spiedigitallibrary.org/article.aspx?articleid=1103026. Accessed September 7, 2013.

48. Thomson J a. Embryonic Stem Cell Lines Derived from Human Blastocysts. *Science (80-.).* 1998;282(5391):1145–1147. Available at: http://www.sciencemag.org/cgi/doi/10.1126/science.282.5391.1145. Accessed October 5, 2012.

49. Martin MJ, Muotri A, Gage F, Varki A. Human embryonic stem cells express an immunogenic nonhuman sialic acid. *Nat. Med.* 2005;11(2):228–32. Available at: http://www.ncbi.nlm.nih.gov/pubmed/15685172.

50. Cobo F, Stacey GN, Hunt C, et al. Microbiological control in stem cell banks: approaches to standardisation. *Appl. Microbiol. Biotechnol.* 2005;68(4):456–66. Available at: http://www.ncbi.nlm.nih.gov/pubmed/16012832. Accessed October 23, 2012.

51. Spits C, Mateizel I, Geens M, et al. Recurrent chromosomal abnormalities in human embryonic stem cells. *Nat. Biotechnol.* 2008;26(12):1361–3. Available at: http://www.ncbi.nlm.nih.gov/pubmed/19029912. Accessed October 5, 2012.

52. Adewumi O, Aflatoonian B, Ahrlund-Richter L, et al. Characterization of human embryonic stem cell lines by the International Stem Cell Initiative. *Nat. Biotechnol.* 2007;25(7):803–16. Available at: http://www.ncbi.nlm.nih.gov/pubmed/17572666. Accessed October 5, 2012.

53. Hartung O, Huo H, Daley GQ, Schlaeger TM. Clump passaging and expansion of human embryonic and induced pluripotent stem cells on mouse embryonic fibroblast feeder cells. *Curr. Protoc. Stem Cell Biol.* 2010;Chapter 1:Unit 1C.10. Available at: http://www.ncbi.nlm.nih.gov/pubmed/20814935. Accessed October 23, 2012.

54. Hough SR, Laslett AL, Grimmond SB, Kolle G, Pera MF. A continuum of cell states spans pluripotency and lineage commitment in human embryonic stem cells. *PLoS One*. 2009;4(11):e7708. Available at: http://www.pubmedcentral.nih.gov/articlerender.fcgi?artid=2768791&tool=pmcentrez&rendertype=abstract. Accessed October 20, 2012.

55. Rodin S, Domogatskaya A, Ström S, et al. Long-term self-renewal of human pluripotent stem cells on human recombinant laminin-511. *Nat. Biotechnol.* 2010;28(6):611–5. Available at: http://www.ncbi.nlm.nih.gov/pubmed/20512123. Accessed August 5, 2010.

56. Derda R, Li L, Orner BP, Lewis RL, Thomson JA, Kiessling LL. Defined substrates for human embryonic stem cell growth identified from surface arrays. *ACS Chem. Biol.* 2007;2(5):347–355. Available at: http://pubs.acs.org/doi/abs/10.1021/cb700032u. Accessed November 29, 2010.

57. Lu J, Hou R, Booth CJ, Yang S-H, Snyder M. Defined culture conditions of human embryonic stem cells. *Proc. Natl. Acad. Sci. U. S. A.* 2006;103(15):5688–93. Available at:

http://www.pubmedcentral.nih.gov/articlerender.fcgi?artid=1458634&tool=pmcentrez&rendertype=abstract. Accessed October 18, 2010.

58. Moody J. Feeder-independent culture systems for human pluripotent stem cells. *Methods Mol. Biol.* 2013;946:507–21. Available at: http://www.ncbi.nlm.nih.gov/pubmed/23179852. Accessed November 19, 2013.

59. Laslett AL, Grimmond S, Gardiner B, et al. Transcriptional analysis of early lineage commitment in human embryonic stem cells. *BMC Dev. Biol.* 2007;7:12. Available at: http://www.pubmedcentral.nih.gov/articlerender.fcgi?artid=1829156&tool=pmcentrez&rendertype=abstract. Accessed October 21, 2012.

60. Enver T, Soneji S, Joshi C, et al. Cellular differentiation hierarchies in normal and culture-adapted human embryonic stem cells. *Hum. Mol. Genet.* 2005;14(21):3129–40. Available at: http://www.ncbi.nlm.nih.gov/pubmed/16159889. Accessed November 12, 2013.

61. Chadwick K, Menendez P, Bendall SC, Bhatia M, Stewart MH, Bosse M. Clonal isolation of hESCs reveals heterogeneity within the pluripotent stem cell compartment. 2006;3(10).

62. Mohr JC, de Pablo JJ, Palecek SP. 3-D microwell culture of human embryonic stem cells. *Biomaterials*. 2006;27(36):6032–42. Available at: http://www.ncbi.nlm.nih.gov/pubmed/16884768.

63. Khademhosseini A, Ferreira L, Blumling J, et al. Co-culture of human embryonic stem cells with murine embryonic fibroblasts on microwell-patterned substrates. *Biomaterials*. 2006;27(36):5968–77. Available at: http://www.ncbi.nlm.nih.gov/pubmed/16901537.

64. Park J, Cho CH, Parashurama N, et al. Microfabrication-based modulation of embryonic stem cell differentiation. *Lab Chip*. 2007;7(8):1018–28. Available at: http://www.ncbi.nlm.nih.gov/pubmed/17653344. Accessed July 31, 2010.

65. Bauwens CL, Peerani R, Niebruegge S, et al. Control of human embryonic stem cell colony and aggregate size heterogeneity influences differentiation trajectories. *Stem Cells*. 2008;26(9):2300–10. Available at: http://www.ncbi.nlm.nih.gov/pubmed/18583540.

66. Haoran L, Peerani R, Ungrin M, Joshi C, Kumacheva E, Zandstra PW. Micropatterning of human embryonic stem cells dissects the mesoderm and endoderm lineages. 2009:155–162.

67. Jonas SJ, Alva J a., Richardson W, et al. A spatially and chemically defined platform for the uniform growth of human pluripotent stem cells. *Mater. Sci. Eng. C*. 2012.

68. Jonas SJ, Alva JA, Richardson W, Sherman S, Galic Z, April D. A spatially and chemically defined platform for the uniform growth of human pluripotent stem cells.

69. Xia Y, Rogers J a., Paul KE, Whitesides GM. Unconventional Methods for Fabricating and Patterning Nanostructures. *Chem. Rev.* 1999;99(7):1823–1848. Available at: http://www.ncbi.nlm.nih.gov/pubmed/11849012.

70. Kane RS, Takayama S, Ostuni E, Ingber DE, Whitesides GM. Patterning proteins and cells using soft lithography. *Biomaterials*. 1999;20(23-24):2363–76. Available at: http://www.ncbi.nlm.nih.gov/pubmed/10614942.

71. Dike LE, Chen CS, Mrksich M, Tien J, Whitesides GM, Ingber DE. Geometric control of switching between growth, apoptosis, and differentiation during angiogenesis using micropatterned substrates. *In Vitro Cell. Dev. Biol. Anim.* 1999;35(8):441–8. Available at: http://www.ncbi.nlm.nih.gov/pubmed/10501083.

72. Singhvi R, Kumar A, Lopez G, et al. Engineering cell shape and function. *Science (80-.).* 1994;264(5159):696–698. Available at: http://www.sciencemag.org/cgi/doi/10.1126/science.8171320. Accessed October 12, 2012.

73. Ostuni E, Yan L, Whitesides GM. The interaction of proteins and cells with self-assembled monolayers of alkanethiolates on gold and silver. 1999;15:3–30.

74. Zhang S, Yan L, Altman M, et al. Biological surface engineering: a simple system for cell pattern formation. *Biomaterials*. 1999;20(13):1213–20. Available at: http://www.ncbi.nlm.nih.gov/pubmed/10395390.

75. Singhvi R, Kumar A, Lopez G, et al. Engineering cell shape and function. *Science (80-.).* 1994;264(5159):696–698.

76. Dike LE, Chen CS, Mrksich M, Tien J, Whitesides GM, Ingber DE. Geometric control of switching between growth, apoptosis, and differentiation during angiogenesis using micropatterned substrates. *In Vitro Cell. Dev. Biol. Anim.* 1999;35(8):441–8.

77. Lauer L, Klein C, Offenhäusser a. Spot compliant neuronal networks by structure optimized micro-contact printing. *Biomaterials*. 2001;22(13):1925–32. Available at: http://www.ncbi.nlm.nih.gov/pubmed/11396899.

78. Tien J, Nelson CM, Chen CS. Fabrication of aligned microstructures with a single elastomeric stamp. *Proc. Natl. Acad. Sci. U. S. A.* 2002;99(4):1758–62. Available at: http://www.pubmedcentral.nih.gov/articlerender.fcgi?artid=122266&tool=pmcentrez&rendertype=abstract.

79. Zhang S, Yan L, Altman M, et al. Biological surface engineering: a simple system for cell pattern formation. *Biomaterials*. 1999;20(13):1213–20.

80. Svedhem S, O M, Svensson SCT, Liedberg B. Influence of Specific Intermolecular Interactions on the Self-Assembly and Phase Behavior of Oligo (Ethylene Glycol) - Terminated Alkanethiolates on Gold. *J. Phys. Chem. B*. 2001:5459–5469.

81. Tien J, Nelson CM, Chen CS. Fabrication of aligned microstructures with a single elastomeric stamp. *Proc. Natl. Acad. Sci. U. S. A.* 2002;99(4):1758–62.

82. Langer R, Vacanti J. Tissue engineering. *Science (80-.).* 1993;260(5110):920–926. Available at: http://www.sciencemag.org/cgi/doi/10.1126/science.8493529. Accessed November 10, 2013.

83. Salinas AJ, Esbrit P, Vallet-Regí M. A tissue engineering approach based on the use of bioceramics for bone repair. *Biomater. Sci.* 2013;1(1):40. Available at: http://xlink.rsc.org/?DOI=c2bm00071g. Accessed November 19, 2013.

84. Gunatillake P a, Adhikari R. Biodegradable synthetic polymers for tissue engineering. *Eur. Cell. Mater.* 2003;5:1–16; discussion 16. Available at: http://www.ncbi.nlm.nih.gov/pubmed/14562275.

85. Tian H, Tang Z, Zhuang X, Chen X, Jing X. Biodegradable synthetic polymers: Preparation, functionalization and biomedical application. *Prog. Polym. Sci.* 2012;37(2):237–280. Available at: http://linkinghub.elsevier.com/retrieve/pii/S007967001100092X. Accessed November 9, 2013.

86. Athanasiou KA, Niederauer GG, Agrawal CM. biocompatibility and clinical applications of polylactic acid / polyglycolic acid copolymers. *Biomaterials*. 1996;17(2).

87. Mao H, Lim SH, Zhang S, Christopherson G, Kam K, Fischer S. The Nanofiber Matrix as an Artificial Stem Cell Niche.

88. *Articular Cartilage Tissue Engineering*.

89. Taylor P. Polymer Nanoparticles for Gene Delivery : Synthesis and Processing. *Nanotechnology*. 2004;(713586178).

90. Kumbar SG, James R, Nukavarapu SP, Laurencin CT. Electrospun nanofiber scaffolds: engineering soft tissues. *Biomed. Mater.* 2008;3(3):034002. Available at: http://www.ncbi.nlm.nih.gov/pubmed/18689924. Accessed October 8, 2010.

91. Ge Z, Yang F, Goh JCH, Ramakrishna S, Lee EH. Review Biomaterials and scaffolds for ligament tissue engineering. *J. Biomed. Mater. Res. Part A*. 2006.

92. Naveena N, Venugopal J, Rajeswari R, et al. Biomimetic composites and stem cells interaction for bone and cartilage tissue regeneration. 2012.

93. Chung C, Burdick J a. Engineering cartilage tissue. *Adv. Drug Deliv. Rev.* 2008;60(2):243–62. Available at: http://www.pubmedcentral.nih.gov/articlerender.fcgi?artid=2230638&tool=pmcentrez&rendertype=abstract. Accessed October 12, 2012.

94. Bratt-leal A, Carpenedo R, Mcdevitt T. Integration of Biomaterials into 3D Stem Cell Microenvironments.

95. Perá M. Functionalized Nanostructures with Application in Regenerative Medicine. 2012:3847–3886.

96. Khademhosseini A, Langer R, Borenstein J, Vacanti JP. Microscale technologies for tissue engineering and biology. *Proc. Natl. Acad. Sci. U. S. A.* 2006;103(8):2480–7. Available at: http://www.pubmedcentral.nih.gov/articlerender.fcgi?artid=1413775&tool=pmcentrez&rendertype=abstract.

97. Phadke A, Chang C, Varghese S. Functional Biomaterials for Controlling Stem Cell Differentiation.

98. Mocan T, Bartos D, Mocan L. Influence of nanomaterials on stem cell differentiation : designing an appropriate nanobiointerface. 2012:3011–3025.

99. Wischke C, Schwendeman SP. Principles of encapsulating hydrophobic drugs in PLA/PLGA microparticles. *Int. J. Pharm.* 2008;364(2):298–327. Available at: http://www.ncbi.nlm.nih.gov/pubmed/18621492. Accessed October 9, 2012.

100. Theses M, Citation R. IGF-I RELEASING PLGA SCAFFOLDS FOR. 2010.

101. Ren T, Ren J, Jia X, Pan K. The bone formation in vitro and mandibular defect repair using PLGA porous scaffolds. *J. Biomed. Mater. Res. A*. 2005;74(4):562–9. Available at: http://www.ncbi.nlm.nih.gov/pubmed/16025492. Accessed November 29, 2010.

102. Park J, Fong PM, Lu J, et al. PEGylated PLGA nanoparticles for the improved delivery of doxorubicin. *Nanomedicine*. 2009;5(4):410–8. Available at: http://www.pubmedcentral.nih.gov/articlerender.fcgi?artid=2789916&tool=pmcentrez&rendertype=abstract. Accessed November 25, 2010.

103. Makadia HK, Siegel SJ. Poly Lactic-co-Glycolic Acid (PLGA) as Biodegradable Controlled Drug Delivery Carrier. 2011:1377–1397.

104. Holy CE, Dang SM, Davies JE, Shoichet MS. In vitro degradation of a novel poly(lactide-co-glycolide) 75/25 foam. *Biomaterials*. 1999;20(13):1177–85. Available at: http://www.ncbi.nlm.nih.gov/pubmed/10395386.

105. LeBlon CE, Pai R, Fodor CR, Golding AS, Coulter JP, Jedlicka SS. In vitro comparative biodegradation analysis of salt-leached porous polymer scaffolds. *J. Appl. Polym. Sci.* 2013;128(5):2701–2712. Available at: http://doi.wiley.com/10.1002/app.38321. Accessed November 20, 2013.

106. Fredenberg S, Wahlgren M, Reslow M, Axelsson A. The mechanisms of drug release in poly (lactic-co-glycolic acid) -based drug delivery systems — A review. *Int. J. Pharm.* 2011;415(1-2):34–52. Available at: http://dx.doi.org/10.1016/j.ijpharm.2011.05.049.

107. Yin Y, Chen D, Qiao M, Lu Z, Hu H. Preparation and evaluation of lectin-conjugated PLGA nanoparticles for oral delivery of thymopentin. *J. Control. Release*. 2006;116(3):337–45. Available at: http://www.ncbi.nlm.nih.gov/pubmed/17097180.

108. Seyednejad H, Ghassemi AH, van Nostrum CF, Vermonden T, Hennink WE. Functional aliphatic polyesters for biomedical and pharmaceutical applications. *J. Control. Release*. 2011;152(1):168–176. Available at: http://linkinghub.elsevier.com/retrieve/pii/S0168365911000095. Accessed November 21, 2013.

109. Giri TK, Thakur A, Alexander A, Badwaik H, Tripathi DK. Modified chitosan hydrogels as drug delivery and tissue engineering systems: present status and applications. *Acta Pharm. Sin. B*. 2012;2(5):439–449. Available at: http://linkinghub.elsevier.com/retrieve/pii/S2211383512001153. Accessed November 10, 2013.

110. Jukes JM, van der Aa LJ, Hiemstra C, et al. A newly developed chemically crosslinked dextran-poly(ethylene glycol) hydrogel for cartilage tissue engineering. *Tissue Eng. Part A*. 2010;16(2):565–73. Available at: http://www.ncbi.nlm.nih.gov/pubmed/19737051.

111. Lin C, Zhao P, Li F, Guo F, Li Z, Wen X. Thermosensitive in situ-forming dextran–pluronic hydrogels through Michael addition. *Mater. Sci. Eng. C*. 2010;30(8):1236–1244. Available at: http://linkinghub.elsevier.com/retrieve/pii/S0928493110001670. Accessed November 19, 2013.

112. Jin R, Moreira Teixeira LS, Dijkstra PJ, et al. Enzymatically crosslinked dextran-tyramine hydrogels as injectable scaffolds for cartilage tissue engineering. *Tissue Eng. Part A*. 2010;16(8):2429–40. Available at: http://www.ncbi.nlm.nih.gov/pubmed/20214454. Accessed November 19, 2013.

113. Ahmed T a E, Dare E V, Hincke M. Fibrin: a versatile scaffold for tissue engineering applications. *Tissue Eng. Part B. Rev.* 2008;14(2):199–215. Available at: http://www.ncbi.nlm.nih.gov/pubmed/18544016. Accessed November 8, 2013.

114. Rowley J a, Madlambayan G, Mooney DJ. Alginate hydrogels as synthetic extracellular matrix materials. *Biomaterials*. 1999;20(1):45–53. Available at: http://www.ncbi.nlm.nih.gov/pubmed/9916770.

115. Andersen T, Strand BL, Formo K. *Alginates as biomaterials in tissue engineering*.; 2012:227–258.

116. Lee KY, Mooney DJ. Alginate: properties and biomedical applications. *Prog. Polym. Sci.* 2012;37(1):106–126. Available at: http://www.pubmedcentral.nih.gov/articlerender.fcgi?artid=3223967&tool=pmcentrez&rendertype=abstract. Accessed February 28, 2013.

117. Censi R, Schuurman W, Malda J, et al. A Printable Photopolymerizable Thermosensitive p(HPMAm-lactate)-PEG Hydrogel for Tissue Engineering. *Adv. Funct. Mater.* 2011;21(10):1833–1842. Available at: http://doi.wiley.com/10.1002/adfm.201002428. Accessed November 19, 2013.

118. Lau TT, Wang D-A. Bioresponsive hydrogel scaffolding systems for 3D constructions in tissue engineering and regenerative medicine. *Nanomedicine (Lond).* 2013;8(4):655–68. Available at: http://www.ncbi.nlm.nih.gov/pubmed/23560414. Accessed November 19, 2013.

119. Huang X, Zhang X, Wang X, Wang C, Tang B. Microenvironment of alginate-based microcapsules for cell culture and tissue engineering. *J. Biosci. Bioeng.* 2012;114(1):1–8. Available at: http://www.ncbi.nlm.nih.gov/pubmed/22561878. Accessed November 19, 2013.

120. Zhou S, Bismarck A, Steinke JHG. Ion-responsive alginate based macroporous injectable hydrogel scaffolds prepared by emulsion templating. *J. Mater. Chem. B*.

2013;1(37):4736. Available at: http://xlink.rsc.org/?DOI=c3tb20888e. Accessed November 19, 2013.

121. Barbetta A, Barigelli E, Dentini M. Porous alginate hydrogels: synthetic methods for tailoring the porous texture. *Biomacromolecules*. 2009;10(8):2328–37. Available at: http://www.ncbi.nlm.nih.gov/pubmed/19591464.

122. Francis NL, Hunger PM, Donius AE, et al. An ice-templated, linearly aligned chitosan-alginate scaffold for neural tissue engineering. *J. Biomed. Mater. Res. A*. 2013;101(12):3493–503. Available at: http://www.ncbi.nlm.nih.gov/pubmed/23596011. Accessed November 19, 2013.

123. Fiedler MJ. Creating Porous Hydrogel Scaffolds using Templating Alginate Microspheres. 2012:55. Available at: http://hdl.handle.net/1773/20211.

124. Takei T, Sakai S, Yokonuma T, Ijima H, Kawakami K. Fabrication of artificial endothelialized tubes with predetermined three-dimensional configuration from flexible cell-enclosing alginate fibers. *Biotechnol. Prog.* 2007;23(1):182–6. Available at: http://www.ncbi.nlm.nih.gov/pubmed/17269686.

125. Colosi C, Costantini M, Barbetta A, Bedini R, Dentini M. Morphological Comparison of PVA Sca ff olds Obtained by Gas Foaming and Micro fl uidic Foaming Techniques. 2013.

126. Shastri VP, Martin I, Langer R. Macroporous polymer foams by hydrocarbon templating. 1999.

127. Nicodemus GD, Bryant SJ. Cell encapsulation in biodegradable hydrogels for tissue engineering applications. *Tissue Eng. Part B. Rev.* 2008;14(2):149–65. Available at: http://www.pubmedcentral.nih.gov/articlerender.fcgi?artid=2962861&tool=pmcentrez&rendertype=abstract. Accessed November 20, 2013.

128. Lin R-Z, Chen Y-C, Moreno-Luna R, Khademhosseini A, Melero-Martin JM. Transdermal regulation of vascular network bioengineering using a photopolymerizable methacrylated gelatin hydrogel. *Biomaterials*. 2013;34(28):6785–96. Available at: http://www.ncbi.nlm.nih.gov/pubmed/23773819. Accessed November 20, 2013.

129. Miller JS, Stevens KR, Yang MT, et al. Rapid casting of patterned vascular networks for perfusable engineered three-dimensional tissues. *Nat. Mater.* 2012;11(9):768–74. Available at: http://www.pubmedcentral.nih.gov/articlerender.fcgi?artid=3586565&tool=pmcentrez&rendertype=abstract. Accessed November 12, 2013.

130. Reddi AH, Ph D, Ph D, Andrades A, Ph D. Nanomaterials and Hydrogel Scaffolds for Articular Cartilage Regeneration. 2011;17(5).

131. Zhao W, Jin X, Cong Y, Liu Y, Fu J. Degradable natural polymer hydrogels for articular cartilage tissue engineering. *J. Chem. Technol. Biotechnol.* 2013;88(3):327–339. Available at: http://doi.wiley.com/10.1002/jctb.3970. Accessed November 20, 2013.

132. Müller F a, Müller L, Hofmann I, Greil P, Wenzel MM, Staudenmaier R. Cellulose-based scaffold materials for cartilage tissue engineering. *Biomaterials*. 2006;27(21):3955–63. Available at: http://www.ncbi.nlm.nih.gov/pubmed/16530823. Accessed October 19, 2012.

133. Tuzlakoglu K, Mano F, Reis RL, Sa H. hydrogel as a three-dimensional extracellular matrix for cartilage-engineered applications. 2011:596–603.

134. Mesa JM, Zaporojan V, Weinand C, et al. Tissue engineering cartilage with aged articular chondrocytes in vivo. *Plast. Reconstr. Surg.* 2006;118(1):41–9; discussion 50–3.

135. Mesa JM, Zaporojan V, Weinand C, et al. Tissue engineering cartilage with aged articular chondrocytes in vivo. *Plast. Reconstr. Surg.* 2006;118(1):41–9; discussion 50–3. Available at: http://www.ncbi.nlm.nih.gov/pubmed/16816672. Accessed October 19, 2012.

136. Mondrinos MJ, Koutzaki S, Jiwanmall E, et al. Engineering three-dimensional pulmonary tissue constructs. *Tissue Eng.* 2006;12(4):717–28. Available at: http://www.ncbi.nlm.nih.gov/pubmed/16674286.

137. Song JJ, Ott HC. Bioartificial lung engineering. *Am. J. Transplant*. 2012;12(2):283–8. Available at: http://www.ncbi.nlm.nih.gov/pubmed/22026560. Accessed November 20, 2013.

138. Nichols JE, Niles J a, Cortiella J. Production and utilization of acellular lung scaffolds in tissue engineering. *J. Cell. Biochem.* 2012;113(7):2185–92. Available at: http://www.ncbi.nlm.nih.gov/pubmed/22573544. Accessed November 12, 2013.

139. Song JJ, Kim SS, Liu Z, et al. Enhanced in vivo function of bioartificial lungs in rats. *Ann. Thorac. Surg.* 2011;92(3):998–1005; discussion 1005–6. Available at: http://www.ncbi.nlm.nih.gov/pubmed/21871290. Accessed November 18, 2013.

140. Dehring KA, Crane NJ, Smukler AR, Mchugh JB, Roessler BJ, Morris MD. Identifying Chemical Changes in Subchondral Bone Taken from Murine Knee Joints Using Raman Spectroscopy. 2006;60(10):1134–1141.

141. Potter K, Kidder LH, Levin IW, Lewis EN, Spencer RGS. Imaging of Collagen and Proteoglycan in Cartilage Sections Using Fourier Transform Infrared Spectral Imaging. 2001;44(4):846–855.

142. Kunstar A, Leijten J, van Leuveren S, et al. Recognizing different tissues in human fetal femur cartilage by label-free Raman microspectroscopy. *J. Biomed. Opt.* 2012;17(11):116012. Available at: http://www.ncbi.nlm.nih.gov/pubmed/23117807. Accessed September 7, 2013.

143. Eltawil NM, De Bari C, Achan P, Pitzalis C, Dell'accio F. A novel in vivo murine model of cartilage regeneration. Age and strain-dependent outcome after joint surface injury. *Osteoarthritis Cartilage*. 2009;17(6):695–704. Available at: http://www.pubmedcentral.nih.gov/articlerender.fcgi?artid=2706394&tool=pmcentrez&rendertype=abstract. Accessed October 4, 2013.

144. Krishna H, Majumder SK, Gupta PK. Range-independent background subtraction algorithm for recovery of Raman spectra of biological tissue. *J. Raman Spectrosc.* 2012;43(12):1884–1894. Available at: http://doi.wiley.com/10.1002/jrs.4127. Accessed September 7, 2013.

145. Chan J, Lieu D. Label-free biochemical characterization of stem cells using vibrational spectroscopy. *J. Biophotonics*. 2009;668(11):656–668. Available at: http://onlinelibrary.wiley.com/doi/10.1002/jbio.200910041/abstract. Accessed September 7, 2013.

146. Wang M, Perera A. Principal Discriminants Analysis for small-sample-size problems : application to chemical sensing. :591–594.

147. Frushour B, Koenig J. Raman scattering of collagen, gelatin, and elastin. *Biopolymers*. 1975;14:379–391. Available at: http://onlinelibrary.wiley.com/doi/10.1002/bip.1975.360140211/abstract. Accessed September 7, 2013.

148. Notingher I, Bisson I, Bishop AE, Randle WL, Polak JMP, Hench LL. In situ spectral monitoring of mRNA translation in embryonic stem cells during differentiation in vitro. *Anal. Chem.* 2004;76(11):3185–93. Available at: http://www.ncbi.nlm.nih.gov/pubmed/15167800.

149. Chen H, Chevrier A, Hoemann CD, Sun J, Picard G, Buschmann MD. Bone Marrow Stimulation of the Medial Femoral Condyle Produces Inferior Cartilage and Bone Repair Compared to the Trochlea in a Rabbit Surgical Model. 2013:1–8.

150. Kalson NS, Gikas PD, Briggs TWR. Current strategies for knee cartilage repair. *Int. J. Clin. Pract.* 2010;64(10):1444–52. Available at: http://www.ncbi.nlm.nih.gov/pubmed/20716151. Accessed November 8, 2013.

151. Barth A, Zscherp C. What vibrations tell us about proteins. *Q. Rev. Biophys.* 2002;4:369–430. Available at: http://journals.cambridge.org/production/action/cjoGetFulltext?fulltextid=141794. Accessed September 7, 2013.

152. Mow VC, Proctor CS, Kelly MA, others. Biomechanics of articular cartilage. *Basic Biomech. Musculoskelet. Syst.* 1989:31–54.

153. Koljenović S, Bakker Schut TC, van Meerbeeck JP, et al. Raman microspectroscopic mapping studies of human bronchial tissue. *J. Biomed. Opt.* 2004;9(6):1187–97. Available at: http://www.ncbi.nlm.nih.gov/pubmed/15568939. Accessed September 9, 2013.

154. Piltti KM, Haus DL, Do E, Perez H, Anderson a J, Cummings BJ. Computer-aided 2D and 3D quantification of human stem cell fate from in vitro samples using Volocity high performance image analysis software. *Stem Cell Res.* 2011;7(3):256–63. Available at: http://www.ncbi.nlm.nih.gov/pubmed/21775237. Accessed September 23, 2013.

155. Shen Q, Wang Y, Kokovay E, et al. Adult SVZ stem cells lie in a vascular niche: a quantitative analysis of niche cell-cell interactions. *Cell Stem Cell*. 2008;3(3):289–300. Available at: http://www.pubmedcentral.nih.gov/articlerender.fcgi?artid=2747473&tool=pmcentrez&rendertype=abstract. Accessed August 6, 2013.

156. Saha K, Mei Y, Reisterer CM, et al. Surface-engineered substrates for improved human pluripotent stem cell culture under fully defined conditions. *Proc. Natl. Acad. Sci. U. S. A.* 2011;108(46):18714–9. Available at: http://www.pubmedcentral.nih.gov/articlerender.fcgi?artid=3219112&tool=pmcentrez&rendertype=abstract. Accessed October 18, 2012.

157. Mrksich M, Dike LE, Tien J, Ingber DE, Whitesides GM. Using microcontact printing to pattern the attachment of mammalian cells to self-assembled monolayers of alkanethiolates on transparent films of gold and silver. *Exp. Cell Res.* 1997;235(2):305–13. Available at: http://www.ncbi.nlm.nih.gov/pubmed/9299154.

158. Nava MM, Raimondi MT, Pietrabissa R. Controlling self-renewal and differentiation of stem cells via mechanical cues. *J. Biomed. Biotechnol.* 2012;2012:797410. Available at:

http://www.pubmedcentral.nih.gov/articlerender.fcgi?artid=3471035&tool=pmcentrez&rendertype=abstract. Accessed November 8, 2013.

159. Dahl KN, Ribeiro AJS, Lammerding J, Discher D, Editor G. Nuclear Shape , Mechanics , and Mechanotransduction. 2013:1307–1318.

160. Bauwens CL, Peerani R, Niebruegge S, et al. Control of human embryonic stem cell colony and aggregate size heterogeneity influences differentiation trajectories. *Stem Cells*. 2008;26(9):2300–10. Available at: http://www.ncbi.nlm.nih.gov/pubmed/18583540. Accessed October 12, 2012.

161. Ploeger LS, Dullens HFJ, Huisman a, van Diest PJ. Fluorescent stains for quantification of DNA by confocal laser scanning microscopy in 3-D. *Biotech. Histochem.* 2008;83(2):63–9. Available at: http://www.ncbi.nlm.nih.gov/pubmed/18568680. Accessed November 20, 2013.

162. Zinchuk V, Zinchuk O, Okada T. Quantitative colocalization analysis of multicolor confocal immunofluorescence microscopy images: pushing pixels to explore biological phenomena. *Acta Histochem. Cytochem.* 2007;40(4):101–11. Available at: http://www.pubmedcentral.nih.gov/articlerender.fcgi?artid=1993886&tool=pmcentrez&rendertype=abstract. Accessed August 7, 2013.

163. Hjelstuen MH, Rasch-Halvorsen K, Brekken C, Bruland O, de L Davies C. Penetration and binding of monoclonal antibody in human osteosarcoma multicell spheroids. Comparison of confocal laser scanning microscopy and autoradiography. *Acta Oncol.* 1996;35(3):273–9. Available at: http://www.ncbi.nlm.nih.gov/pubmed/8679256. Accessed November 20, 2013.

164. Shi J, Xing MMQ, Zhong W. Development of Hydrogels and Biomimetic Regulators as Tissue Engineering Scaffolds. 2012:70–90.

165. Osathanon T, Linnes ML, Rajachar RM, Ratner BD, Somerman MJ, Giachelli CM. Microporous nanofibrous fibrin-based scaffolds for bone tissue engineering. *Biomaterials*. 2008;29(30):4091–9. Available at: http://www.ncbi.nlm.nih.gov/pubmed/18640716.

166. Sodha S. A Microfabricated 3-D Stem Cell Delivery Scaffold for Retinal Regenerative Therapy by L BRAR. 2009.

167. Stein A, Wilson BE, Rudisill SG. Design and functionality of colloidal-crystal-templated materials--chemical applications of inverse opals. *Chem. Soc. Rev.*

2013;42(7):2763–803. Available at:
http://www.ncbi.nlm.nih.gov/pubmed/23079696. Accessed November 15, 2013.

168. Becker R. Electron microscopy of the lung Edited by Dean E. Schraufnagel, M.D. Marcel Dekker, Inc., New York and Basel (1990) ISBN 082478319-0; 612 pages, illustrated, $199.00. *Scanning*. 1992;14(6):365–365. Available at:
http://doi.wiley.com/10.1002/sca.4950140610. Accessed November 20, 2013.

169. Knight CG, Willenbrock F, Murphy G. A novel coumarin-labelled peptide for sensitive continuous assays of the matrix metalloproteinases. *FEBS Lett.* 1992;296(3):263–6. Available at: http://www.ncbi.nlm.nih.gov/pubmed/1537400.

170. Zhang Y, Hong H, Myklejord D V, Cai W. Molecular imaging with SERS-active nanoparticles. *Small*. 2011;7(23):3261–9. Available at:
http://www.pubmedcentral.nih.gov/articlerender.fcgi?artid=3228876&tool=pmcentrez&rendertype=abstract. Accessed November 17, 2013.

171. Zurbuchen M a, Lake MP, Kohan S a, Leung B, Bouchard L-S. Nanodiamond landmarks for subcellular multimodal optical and electron imaging. *Sci. Rep.* 2013;3:2668. Available at:
http://www.pubmedcentral.nih.gov/articlerender.fcgi?artid=3773618&tool=pmcentrez&rendertype=abstract. Accessed November 21, 2013.

172. Ren H, Zhang L, Wang T, Li L, Su Z, Wang C. Universal and facile synthesis of multicolored upconversion hollow nanospheres using novel poly(acrylic acid sodium salt) microspheres as templates. *Chem. Commun. (Camb).* 2013;49(54):6036–8. Available at:
http://www.ncbi.nlm.nih.gov/pubmed/23719769. Accessed November 11, 2013.

173. Nie H, Khew ST, Lee LY, Poh KL, Tong YW, Wang C-H. Lysine-based peptide-functionalized PLGA foams for controlled DNA delivery. *J. Control. Release*. 2009;138(1):64–70. Available at:
http://www.ncbi.nlm.nih.gov/pubmed/19409431. Accessed November 29, 2010.

174. Concaro S, Gustavson F, Gatenholm P, et al. Bioreactors for Tissue Engineering of Cartilage. 2009:125–143.

175. Haasper C, Zeichen J, Meister R, Krettek C, Jagodzinski M. Tissue engineering of osteochondral constructs in vitro using bioreactors. *Injury*. 2008;39 Suppl 1:S66–76. Available at: http://www.ncbi.nlm.nih.gov/pubmed/18313474. Accessed September 6, 2013.